Ion Exchange, Self-Assembly, and Light Emission

A Dance of Ions and Light

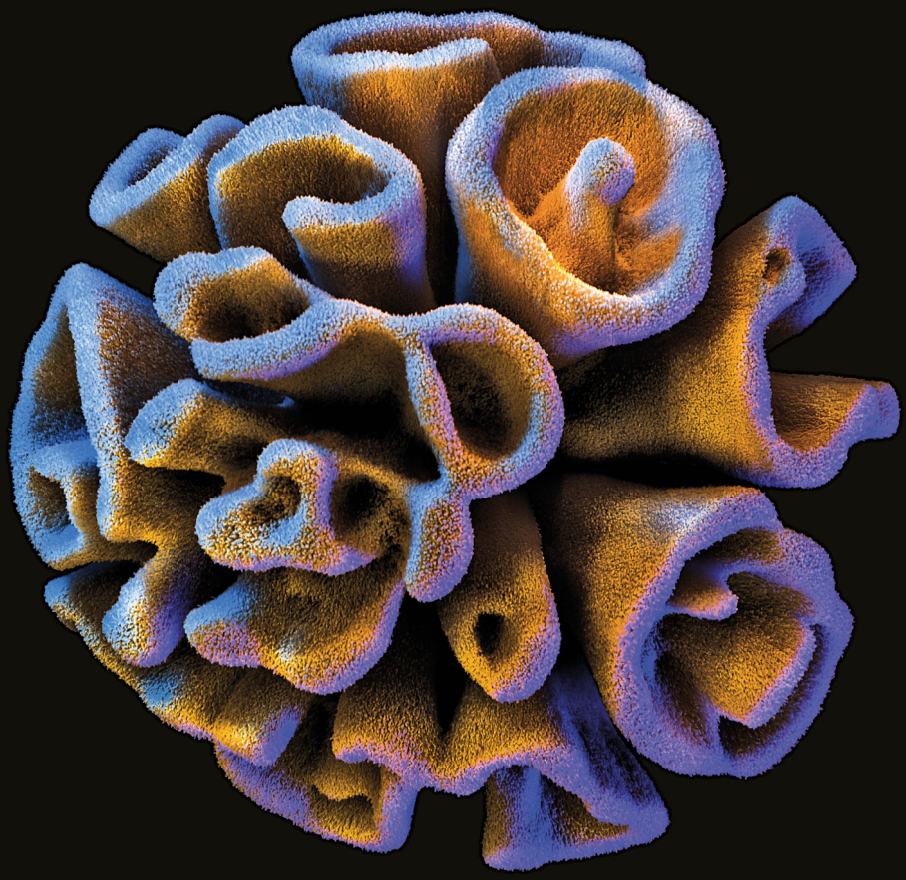

Lukas Helmbrecht

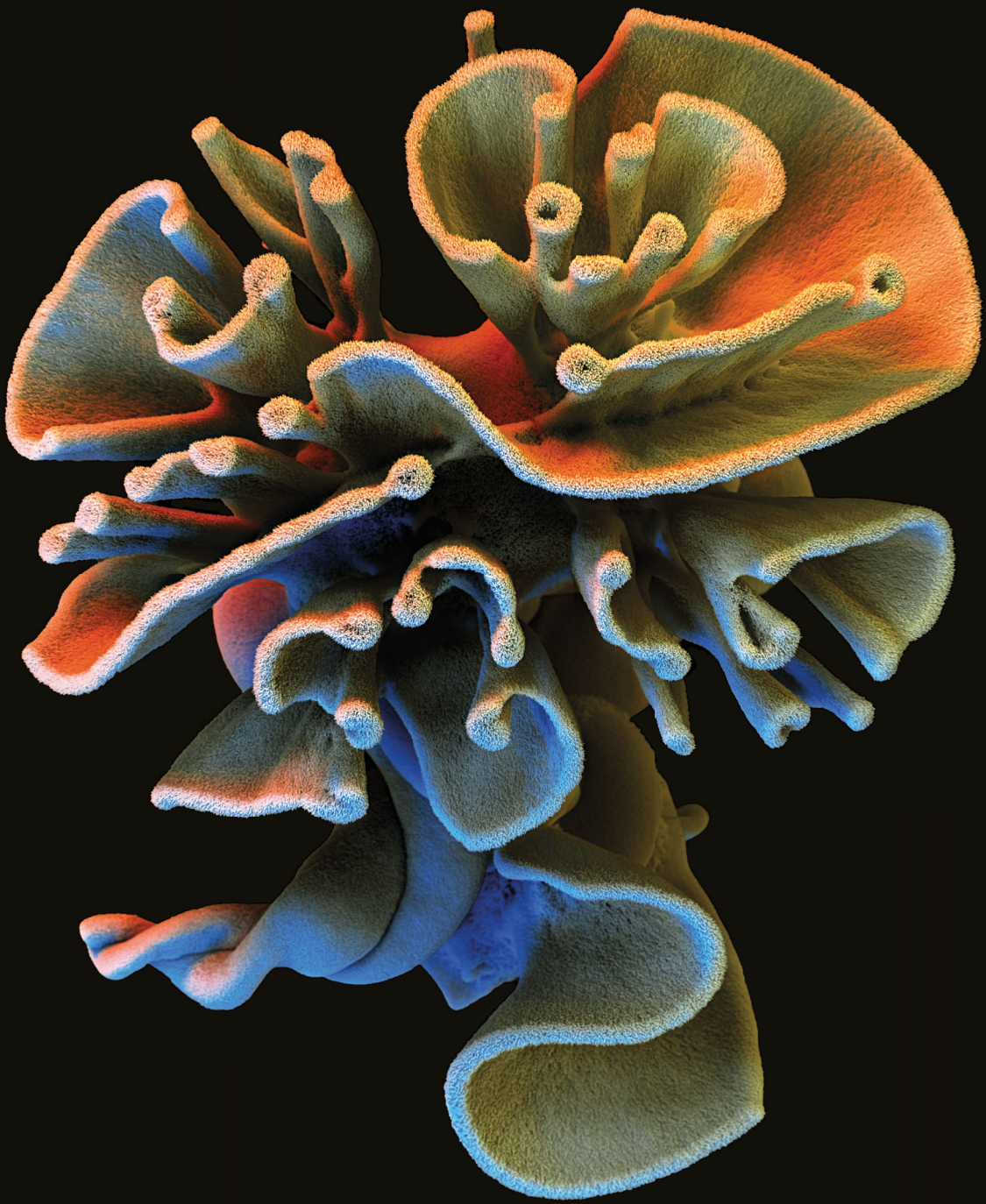

Ion Exchange, Self-Assembly, and Light Emission

A Dance of Ions and Light

Ph.D. Thesis, University of Amsterdam, August 2020
Ion Exchange, Self-Assembly, and Light Emission — A Dance of Ions and Light
Lukas Helmbrecht

Cover image:
Scanning electron micrograph of a self-assembled barium carbonate/silica microarchitecture. The colors are created through combination of multiple detectors. Imaged by Stefan Diller, Scientific Photography, Würzburg, Germany.

ISBN:978-94-92323-41-5

The work described in this thesis was performed at
AMOLF, Science Park 104, 1098 XG, Amsterdam, The Netherlands.

This work is part of the Dutch Research Council (NWO). It is also funded by the Vernieuwingsimpuls Vidi research program "Shaping up materials" with project number 016.Vidi.189.083.

This thesis was produced on FSC® certified materials.
A digital version of this thesis can be downloaded from
http://amolf.nl and https://dare.uva.nl/

Ion Exchange, Self-Assembly, and Light Emission

A Dance of Ions and Light

ACADEMISCH PROEFSCHRIFT

ter verkrijging van de graad van doctor
aan de Universiteit van Amsterdam
op gezag van de Rector Magnificus
prof. dr. ir. K.I.J. Maex
ten overstaan van een door het College voor Promoties ingestelde commissie,
in het openbaar te verdedigen in de Aula der Universiteit
op vrijdag 20 november 2020, te 11:00 uur

door

Lukas Helmbrecht

geboren te Karlsruhe

Promotiecommissie:

Promotor:	prof. dr. H.J. Bakker	*Universiteit van Amsterdam*
Copromotor:	dr. W.L. Noorduin	*AMOLF, Amsterdam*
Overige leden:	prof. dr. E.C. Garnett	*Universiteit van Amsterdam*
	prof. dr. A.M. Brouwer	*Universiteit van Amsterdam*
	prof. dr. N.F. Shahidzadeh	*Universiteit van Amsterdam*
	dr. E.M. Hutter	*Utrecht University*
	prof. dr. M.L. van Hecke	*Universiteit Leiden*
	prof. dr. P. Levkin	*Karlsruher Institut für Technologie*

Faculteit der Natuurwetenschappen, Wiskunde en Informatica.

"A scientist in his laboratory is not only a technician: he is also a child placed before natural phenomena which impress him like a fairy tale."

Marie Skłodowska-Curie,
in *Madame Curie: A Biography*
by Eve Curie Labouisse.[1]

To my parents.

Contents

Minerals in Bloom
Clay, 2019
Lukas Helmbrecht
Part of the series "Molding Nano" curated by Giada La Gala

CHAPTER 1

Introduction

Order in materials is the fundament of the world we live in. Without order, neither a cell nor a building would exist.[2] Biological materials are ordered with unprecedented complexity across length scales to achieve extraordinary performance.[3] Human-made materials alike perform best when made from hierarchically ordered building blocks.[3] Such ordered materials often consist of two or more components that together form a composite material which can exhibit material properties beyond the ones of their individual components. The order in composite materials can reach down to the nanoscale, thereby creating extraordinary material performance that surpasses the performance of the individual bulk materials. A simple, yet impressive example is the hardness of nacre in seashells.[4] Long before humans had the means to probe the nanoscale, they already had developed processes that exploit order at that scale, for example, by encapsulating fragile pigments in nanoscopic host matrices to create paintings withstanding UV irradiation and heat.[5] When materials science flourished in the 20^{th} century, researchers started to deliberately compose materials of intricate complexity across various scales, ranging from fiber-reinforced polymers to integrated electronic circuits. While humans achieve increasingly complex architectures, the processes are oftentimes difficult and cumbersome, leaving nature's extraordinary structuring capabilities unmatched. Therefore, developing new, nature-inspired, design routes of fabrication will allow to gain control over multiple material properties with increased performance while facilitating the fabrication process.

1.1 Self-Assembly

Humanity has always shaped its surroundings, and its ability to do so is mostly defined by the available tools.[6] While fabrication techniques have evolved in precision to create fine mechanics in a watch and nanometer-sized features in integrated circuits, those approaches require sophisticated processes. Often, the material is machined from the bulk down to the desired shape and composition, giving it the name 'top-down' manufacturing. The laboriousness of ordering material at such small scales sparks the desire to find different routes starting from the 'bottom-up' where material forms itself (once the right conditions are met). For nanoparticles, this implies to assemble them from molecular precursors, which is intuitively advantageous over milling down bulk material.

Nanoparticles give access to another bottom-up route for building materials. Intricate architectures can be assembled from distinct building blocks by exploiting their material specific interactions.[3,7–11] Tailoring these interactions allows to direct how building blocks arrange into an ensemble, thus giving it the name directed-assembly or self-assembly: "Self-assembly is the autonomous organization of components into patterns"- G. M. Whitesides.[2] This is one of the few available processes to order materials at the micro- and nanoscale. Self-assembly exhibits many desirable properties: the processes often take place at moderate reaction conditions, are very easy to scale and don't require sophisticated cleanroom facilities.

1.1.1 Ordering in Natural Materials

In living organisms, matter is organized at all scales.[2,10] This phenomenon is so profound that, even on the smallest scale, the complexity of a molecule can serve as an indicator whether an organism had formed it.[12] On a slightly larger scale, organisms embed micro- and nanometer sized crystals into amorphous matrices to synthesize architectures beyond crystallographic symmetries.[13,14]

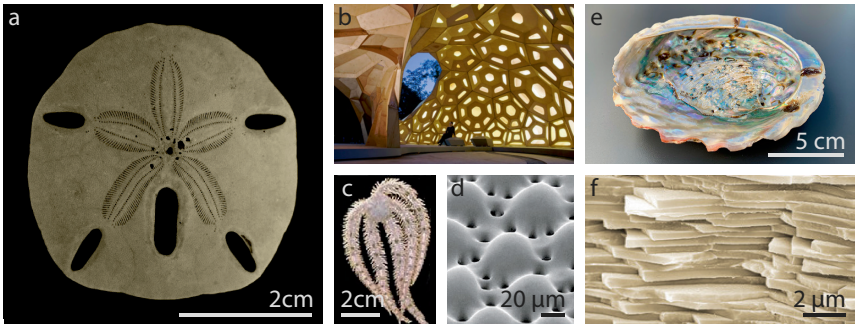

FIGURE 1.1: Order in natural materials. a) Skeleton of a sand dollar. b) Pavilion constructed following the light-weight design principles of the sand dollar skeleton.[15] c) Brittle star, a sea star whose skeleton is covered with d) calcium carbonate micro lenses, allowing it to "see"[16] e) Abalone shell with iridescent nacre. f) SEM micrograph of fractured nacre revealing the layered architecture.[17] *Copyright note:*[1]

This so-called biomineralization with its hierarchical organization of composition allows creating architectures with orthogonal properties (e.g., light and tough) for considerably different purposes, oftentimes even from the same material.[13,17–19] The diversity in functionality that can be achieved through arranging the same

[1]Copyright note: b) Reproduced with permission.[15] Copyright 2012, John Wiley and Sons. c, d) Adapted with permission.[16] Copyright 2001, Springer Nature. e) Image: A.V. Mader. f) Adapted with permission.[17] Copyright 2014, Springer Nature.

material in different ways becomes especially evident when studying calcium carbonate biominerals: the double-curved shell of sand dollars has served as blueprint for lightweight and strong buildings,[20] the nacre of an abalone shell protects the organism and fascinates humans with its iridescence,[4,21] while the accurate crystallographic alignment of calcite allows the brittle star to "see" with its skeleton (Figure 1.1).[16] That all these functionalities are based on the same mineral illustrates a general theme in biomineralization—a limited selection of crystalline materials is combined with amorphous matter to yield architectures with different functionalities. It is thus through the order within a material that functionality can be designed to tailor individual properties separately and outperform bulk properties by far. Hence, taking inspiration from biominerals to develop simple routes to synthetic, hierarchically ordered structures offers great opportunities for new ways to fabricate functional materials.

1.1.2 Synthetic Self-Assembly

Humans possess an innate admiration for the patterns found in nature.[18,22,23] Fascinated by the seemingly effortless manner with which those processes take place, scientists took inspiration and developed self-assembly systems to create architectures from the bottom up.[2,3,7,8,10,24–32] Despite tremendous progress, synthetic self-assembly approaches are yet to meet the grace and complexity found in nature. However, while nature is limited to a small set of compounds,[13] synthetic approaches can choose from a wide variety of materials, thus allowing to create architectures for applications such as optics, (opto-)electronic and catalysis.[10]

The potential of tapping into this vast variety of synthetic materials is exemplified by colloidal self-assembly.[8,9,11,26,33–38] This approach thrives through its simplicity—it is the assembly of structures from particles in solution and thereby gives accesses to the tremendous variety of nanoparticles synthesized to date.[8,39]

By exploiting physical and chemical interactions of those nanoparticles in solution, architectures harnessing the versatility of their building blocks have been assembled, serving fields such as optics, magnetics, catalysis, and electronics.[8] Furthermore, new properties can even emerge from the ordering itself rather than the material properties alone. A visually appealing example are synthetic opals (photonic crystals) that use order on the scale of the wavelength of light (Figure 1.2).[40,41] The sequence in which the building blocks assemble is programmed by the interaction of the particles with each other. Mainly, they can attract or repulse each other in many specific manners. Careful tuning of these interactions allows controlling the final design, e.g., through tailored surface morphology and chemistry (Figure 1.2c, d).[8,9,33] Even more complex architectures can be obtained by introducing multiple particle species to the self-assembly process, or through coprecipitation with amorphous material.[42,43]

Exploiting particle interactions to create architectures makes self-assembly approaches scalable and straightforward. However, due to the ordered packing between the individual particles, the results are dominated by symmetric superstructures. Overcoming these restrictions and introducing in-situ control over the assembled morphology will be essential for a more widespread application of bottom-up assembly.

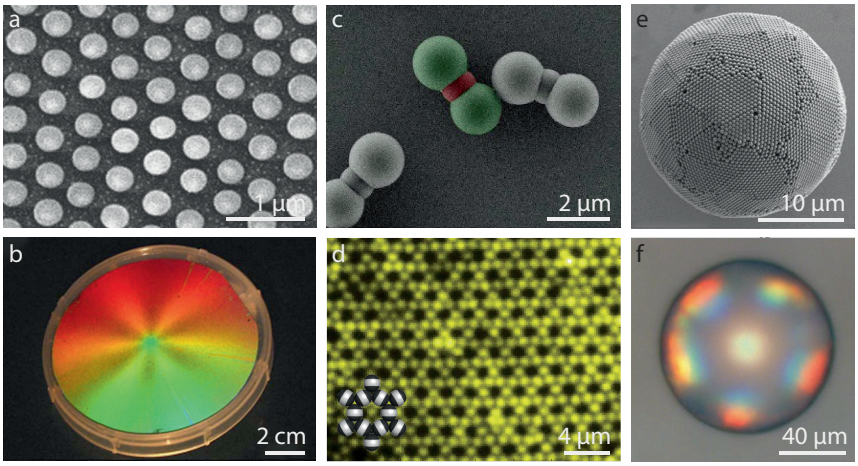

FIGURE 1.2: Synthetic self-assembly. a) Ordered monolayer of silica colloids giving rise to b) structural color under white light.[41] c) Anisotropic polymer colloids.[9] d) Triblock Janus particles with hydrophobic poles assembling into a Kagome lattice.[44] e, f) Hierarchically ordered photonic ball based on polystyrene colloids, SEM and optical micrograph.[45] *Copyright note:*[2]

1.2 Self-Assembled Carbonate Microarchitectures

Spontaneous pattern formation processes can yield complex arrangements that are not restricted to repetitive lattices.[18] Sometimes, when the interplay between two components is defined by diffusion and reactions, complicated patterns emerge that can be controlled through the modulation of the reaction conditions.[18] Intricate 3D architectures can form during the reaction/diffusion controlled self-assembly of carbonate microarchitectures (Figure 1.3).[24,29,46–53]

[2]Copyright note: a, b) Adapted with permission.[41] Copyright 2006, AIP Publishing. c) Adapted with permission.[9] Copyright 2013, Springer Nature. d) Adapted with permission.[44] Copyright 2011, Springer Nature. e, f) Adapted with permission.[45] Copyright 2014, Vogel et. al..

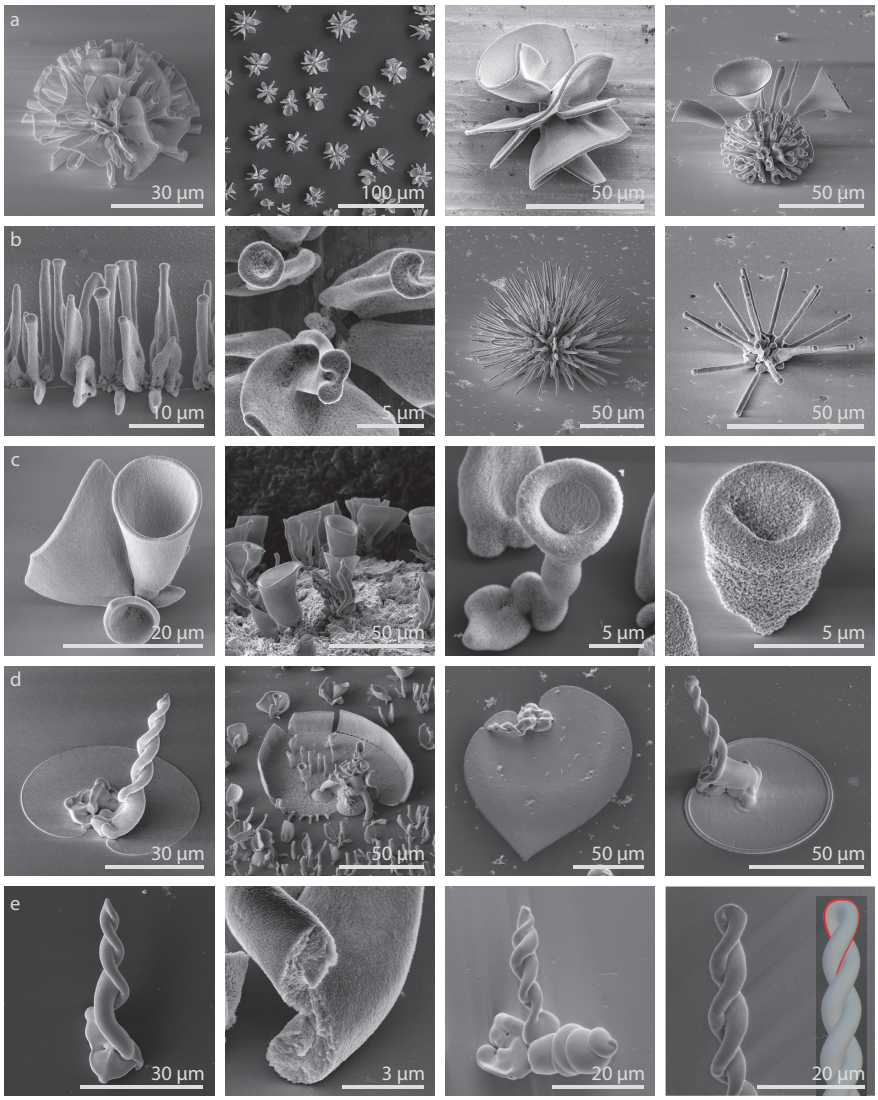

FIGURE 1.3: Typical self-assembled carbonate architectures. a) Coral-like shapes (left to right: typical corals, top-view of a field of corals, coral overgrown with vases). b) Stems (left to right: row of stems, top-view onto stems, typical coral overgrown with stems, small coral overgrown with stems). c) Vase-like shapes (left to right: typical vase, vases and stems on rough aluminum, stem transitioning into a vase with thick rim, very small vase). d) Leaf-like shapes (left to right: leaf with upright helix, leaf overgrown with stems, leaf with horizontal helix, leaf with double rim). e) Helices (left to right: double helix, cross-section of double helix revealing the internal layout, double and single helix, double helix in comparison to a simulated one[49]). *Simulation in e) adapted with permission.*[49] *Copyright 2017, AAAS.*

These hierarchical composites of almost life-like appearance can be grown from solution and are composed of earth alkali metal carbonates ($BaCO_3$, $SrCO_3$, and $CaCO_3$) and silica. First discovered by García-Ruiz, they are often referred to as "Biomorphs" for their striking resemblance to biogenic minerals, albeit the absence of organic molecules during the synthesis.[47,54] Soon, shapes where synthesized that do not have a natural look-alike.[29] In this work, we therefore refer to them as (micro)architectures. The synthesis of these architectures offers a broad variety of shapes (corals, vases, stems, helices, and others) with morphology control through external parameters (Figure 1.3).

1.2.1 Synthesis of Carbonate Microarchitectures

The complexity that can emerge from such simple starting materials as barium ions and metasilicate has intrigued many researchers to study their formation in great detail.[24,29,46,47,49,51] These studies have led to a better understanding of the system itself,[55] as well as given the means to control and even model their growth.[49] The microarchitectures can be described as an ordered ensemble of elongated nanocrystals (≈20 nm) that together form the microscopic shape (10-100 µm) and follow the curvature of the microarchitecture.[24,29,46,47,49,51] The nanocrystals are embedded inside a silica matrix. The microarchitectures are formed in aqueous solution (or gels) from earth alkali metal ions and silica under CO_2 influx. Conventional colloidal self-assembly approaches are a sequential process, first nanoparticles are synthesized, then they are assembled. In contrast, carbonate microarchitectures are synthesized in a single process. Here, the nanocrystals form from solution at the growth front to assemble into the microarchitecture - resulting in a single-step, fast, and straightforward fabrication.

The system is based on coprecipitation of earth alkali metal carbonates ($BaCO_3$, $SrCO_3$, and $CaCO_3$) and polymerization of silica, which are linked through an acid-catalyzed feedback loop. In the case of barium carbonate, CO_2 from the atmosphere diffuses into the solution and triggers $BaCO_3$ precipitation. Strontium and calcium follow an almost identical mechanism. This can be described by the following simplified reaction:[24,29]

$$Ba^{2+} + CO_2 + H_2O \rightarrow BaCO_3 + 2H^+. \tag{1.1}$$

If the bulk solution is more alkaline than the regime of silica polymerization, the formation of H^+ locally decreases the pH at the growth front until the pH for silica polymerization is reached. The simplified reaction can be written as:

$$SiO_3^{2-} + 2H^+ \rightarrow SiO_2 + H_2O. \tag{1.2}$$

The local decrease of pH at the growth front causes the silica to polymerize on the crystallizing $BaCO_3$, thereby blocking its growth and restricting the crystals to nanometer sizes. The constant influx of CO_2 drives the formation of new $BaCO_3$

crystals, which again will be encapsulated by silica. This so-called coprecipitation results in an ensemble of nanoscopic crystals that are individually sealed by a thin layer of silica, and as a whole covered by a thicker layer of silica. The polymerization of silica is pH-dependent and has a narrow optimum.[29] Growth can take place on either side of this optimum (Figure 1.4). In both cases, the process starts with $BaCO_3$ nucleation. On the far alkaline side of the silica optimum, the local pH decreases until the regime of silica polymerization is met. Then, growth is favorable towards the bulk of the solution where the pH is more alkaline, growth in that direction is therefore not inhibited. The resulting carbonate microarchitectures resemble stem-, vase-, or coral-like shapes (Figure 1.4, region 3). Starting much closer to the silica optimum, $BaCO_3$ nucleation decreases the pH below the optimum for silica polymerization. Here, growth towards the bulk of the solution results in reaching the silica polymerization optimum and blocking of growth. Therefore, structures grow towards each other or flat on the substrate, resulting in coral or leaf-like architectures. (Figure 1.4, region 2). Starting the reaction at a pH below the silica polymerization regime results in the growth of conventional whiterite crystals, as no silica can polymerize (Figure 1.4, region 1). This oscillating interaction continues until the consumption of precursors and the influx of CO_2 have disturbed the balance of the coprecipitation.

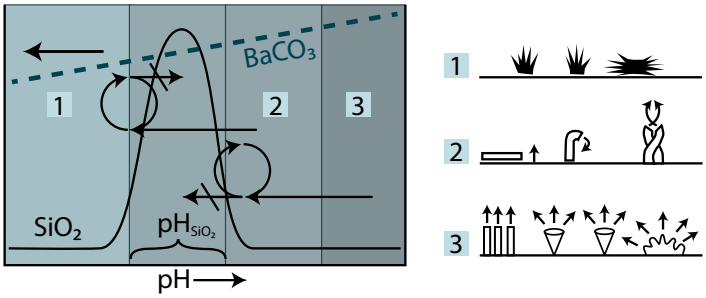

FIGURE 1.4: Schematic of barium carbonate/silica coprecipitation. Adapted with permission of W. L. Noorduin.[29] Left: schematic of the pH dependence. Right: resulting shapes. Silica polymerization is optimal within a narrow pH regime (pH_{SiO2}). Starting with a bulk pH in regime 3, $BaCO_3$ nucleates and thereafter its growth decreases the local pH at the growth front until the pH-regime of silica polymerization is met. Then, silica formation inhibits the growth. The bulk pH remains higher, which allows the growth to continue towards the solution creating architectures as seen on the right side, region 3, as well as in Figure 1.3a–c. In regime 2, the drop in pH, caused by the $BaCO_3$ formation, moves the growth front onto the left side of the silica optimum. Here, the growth direction is opposite, growth towards the bulk solution results in reaching the silica polymerization regime, thus blocking the growth. Architectures, therefore, grow towards each other, as seen in region 2 on the right side and in Figure 1.3d–e. Growth of $BaCO_3$ in regime 1 does not trigger silica precipitation; therefore, only conventional whitherite crystals form.

As this system is based on the interplay of different reactions, it is possible to direct the growth by changing the balance between them. The main handles to steer the growth can be derived from the dependencies apparent in the reaction scheme.[49] Modulation of the CO_2 influx can be used to increase the $BaCO_3$ precipitation, which can yield vase-like shapes. Adjustment of the pH does not only enable to enter two distinctly different growth regimes but also to allows tuning the growth within these regimes. The temperature-dependent solubilities and reaction rates offer yet another way to manipulate growth. Collectively these insights have led to the development of models that can reproduce the growth of know structures and can predict new ones (Figure 1.3e).[49] Beyond these intrinsic parameters, crystal growth is very susceptible to the incorporation of additives that may allow extreme alterations of the morphology.

1.2.2 Prospects of Carbonate Microarchitectures

A unique characteristic of the metal carbonate/silica coprecipitation system is the hierarchy in its architecture. The interplay between carbonate and silica results in short-range ordered nanocrystals (typical size 10-30nm) which are enveloped by thin layers of silica. On the micrometer scale, long-range order between the crystal ensemble and the morphology emerges as they follow the local curvature. Furthermore, the crystals align their elongated shape (they are elongated along their crystallographic c-axis), while the silica passivation of the crystal growth ensures a quasi-monodisperse crystal size distribution.

In colloidal assembly approaches, the particles are typically synthesized and functionalized in a separate step before the assembly. The prior functionalization encodes the final structure already into the individual particles and thereby limits the possibilities to steer the assembly process dynamically during assembly. In contrast, the growth of carbonate microarchitectures is based on coupled chemical reactions that are sensitive to external stimuli that shift the balance in their interplay. Hence, the shape of the architecture can be manipulated during the growth process. This dynamic steering allows constructing architectures one step closer to the finesse found in nature.

While colloidal assembly accesses many materials but is very limited in the accessible shapes, these carbonate architectures offer many shapes but are restricted to a few carbonate salts ($BaCO_3$, $SrCO_3$, and $CaCO_3$) in combination with silica. This limited choice of materials may partially be compensated by post synthesis functionalization of the outer silica layer,[50,53,56] yet widespread technological applications will require the accessibility of different material compositions.

1.3 Self-Assembled Crystals and Light

Crystals have always fascinated humans with their shine.[21] Therefore, crystals have been a topic of interest for many scientists that explored their ability to manipulate light, at least since Vikings used birefringent to navigate (Figure 1.5e).[57,58] The discovery which sparked plenty of research in the interactions between light and crystals was Arago's observation in 1811 that linear polarized light undergoes a rotation when transmitted through quartz.[59] This insight was followed by many experiments that contributed to the understanding of how light interacts with chiral media.[60–63] Scientists discovered that crystals also could be chiral, and depending on their handedness, will rotate light to the left or right.[63] In α-quarz, for example, the order of the atoms in the crystal lattice is chiral. This chirality can be mimicked through a twisted stack of linearly birefringent sheets of mica.[64,65] In these so-called Reusch piles, named after the scientist who discovered them, the chiral behavior is absent in the individual sheets and emerges from their order. While the order of a crystal structure is difficult to change, the alignment of mica sheets can easily be modified. A modern-day implementation where light follows the twist of a crystal can be found in liquid crystal displays. These liquid crystals can undergo a phase transition from linear (nematic) to chiral (cholesteric) and thereby rotate light, which is used to switch pixels on and off. This demonstrates the ability of ordered crystalline ensembles to manipulate light. Gaining control over assembly of those ensembles is a powerful tool that will allow to design the response of light to a material.

Nature has developed many ways to manipulate light by creating sophisticated order of materials (Figure 1.1c-f and 1.5a-c).[66–69] An example that highly resembles modern-day optical fibers is the silica skeleton of a marine glass sponge (Figure 1.5c).[70] Other organisms have also shown excellent control over crystal growth; a prime example are the calcite eyes of brittle stars (a type of sea star) (Figure 1.1c, d).[16] Here the shape is optimized to focus light on the underlying neural cells, and even the crystallographic orientation is optimized to minimize optical distortion. There are many more examples of natural optical structures,[69] all of which are formed under ambient conditions and mild temperatures. These moderate reaction conditions in nature stand in sharp contrast to the oftentimes harsh conditions and elevated temperatures of industrial manufacturing.

Aware of the potential that lies in the ordering of matter and fascinated by the finesse of natural systems, scientists used self-assembly to create materials with optical functionality (Figure 1.2).[19,32] The many examples span a broad spectrum: some are mimicking their biological counterparts (Figure 1.5d),[25] others create advanced optical components such as glass fibers with integrated sensors,[71] or exploit periodicity to create structural colors (Figure 1.2).[40,72–75] Overall, the assembly from small units creates materials that cannot exist in bulk and that have material properties that emerge from the composition and order in the assembly. We en-

vision that the development of strategies that offer control over the alignment of individual building blocks, as well as control over the microscopic morphology will result in materials with novel functionalities.

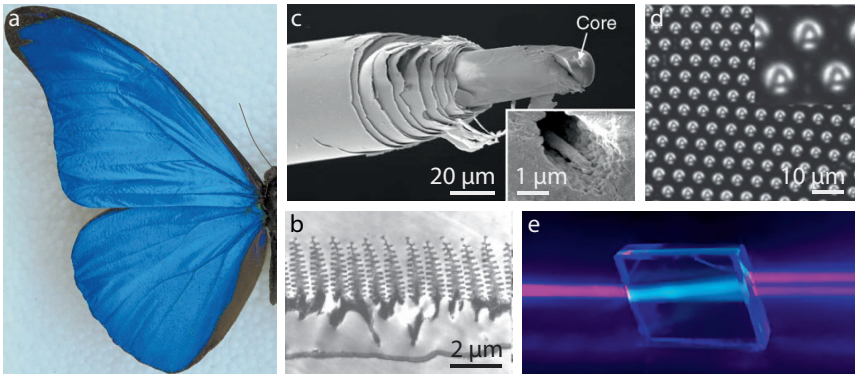

FIGURE 1.5: Optical structures. a) Photograph of Morpho butterfly wing and b) SEM micrograph of the color-giving ordered structure.[69] c) Spicule of a silica-based sea sponge, the layered architecture resembles commercial optical fibers used for telecommunications.[70] d) Self-assembled calcium carbonate microlens array projecting the letter "A". The architecture is mimicking the eyes of the brittle star (Figure 1.1c, d).[25] e) Calcite crystal, which due to its birefringence, splits an unpolarized laser beam into two polarized beams. Vikings likely used this to navigate on cloudy days.[76] *Copyright note:*[3]

1.4 Controlling Chemical Composition Using Ion Exchange

Self-assembly has brought sophisticated spatial control over materials by arranging them from single building blocks into functional structures. Mostly, the building blocks are nanoparticles.[8–11,14,33,34,38,39,77–82] These nanoparticles exhibit a wide variety in their size, morphology, composition, crystallinity, and surface functionality, which define their specific electronic, optical, magnetic, or catalytic activity.[39,77] Ideally, those properties would be controlled independently. However, the properties are entangled by their synthesis route.[83–85] Consequently, not all properties of nanoparticles can be controlled independently, making some combinations inaccessible.

The chemical composition can, for ionic nanoparticles, be manipulated post-synthesis through ion exchange reactions.[34,48,83–89] This approach starts with the

[3]Copyright note: a, b) Reproduced with permission.[69] Copyright 2003, Springer Nature. c) Adapted with permission.[70] Copyright 2004, National Academy of Sciences. d) Adapted with permission.[25] Copyright 2012, Springer Nature. e) Adapted with permission.[76] Copyright 2014, Taylor and Francis.

synthesis of a particle which differs in composition from the desired one but matches the targeted properties such as shape and crystal structure. Post synthesis, the material is then converted to the desired composition through an ion exchange reaction. In this process, one ionic species is replaced by another one of similar size and commonly also identic charge.

Ion exchange reactions have a long history: they are known to occur in rocks and fossils and have found technological application in thin films to create waveguides or modify semiconductors.[90–92] Applying these types of reactions to nanoparticles has sparked a new field that developed new ways to control the chemical composition of particles. Remarkably, ion exchange retains some properties of the original crystal such as crystal-lattice and morphology, while changing the material composition of particles entirely or selectively.[83–85] Thereby, ion exchange offers an opportunity to disentangle shape and chemical composition, and provides new ways to expand the already extensive library of nanoparticles by compositions that formerly were inaccessible.

The last two decades have brought significant advances in the understanding of the underlying principles of ion exchange reactions.[83,85] A fundamental requirement is the possibility for one ionic species to leave the crystal and the availability of another ion to take its place (Figure 1.6a–c). The supply and removal of ions are often mediated by solutions and sometimes also by gas phases. Intuitively the process can be understood as a striving for equilibrium (following Le Chatelier's principle).[93] An ionic crystal AX constituted of A^+ and X^- can potentially undergo an ion exchange to BX when exposed to an abundance of B^+ ions. Therefore, AX has to undergo dissociation, A^+ solvation, B^+ desolvation, and BX association. The energies associated with these processes determine whether or not the ion exchange is thermodynamically feasible. The association and dissociation energies largely depend on the lattice energy of the ionic crystal, while (de-)solvation is driven by the affinity of the ions for the solvent and the solubility constants.[83,85]

Besides the thermodynamic considerations, it is essential to understand the practical implications that arise from the kinetics.[83,85] In order to replace one ion by another, ions have to move through the solution towards and away from the crystals. The rate of the reaction is mostly determined by the surface to volume ratio of the crystals and the diffusivity of the individual ions. More importantly, ions also need to move inside the crystal. Their transport is commonly supported by vacancy or interstitial diffusion (Figure 1.6a–c).[83,85] These diffusion processes inside the crystal depend on many factors, one of them being the size of the ions that are exchanged, as larger ions generally diffuse slower. Furthermore, the ability of a crystal to accommodate strain, which is much higher in nanocrystals that in bulk, assists the movement of ions. Overall, cation exchange in nanocrystals has been widely studied.[83,85] Exchanging anions remains difficult, primarily because of their larger size and thereby slower diffusion rates.[86,94] Ion exchange in bigger,

microscopic, architectures is more challenging than in nanoparticles due the much longer diffusion paths that often prevent a complete exchange.

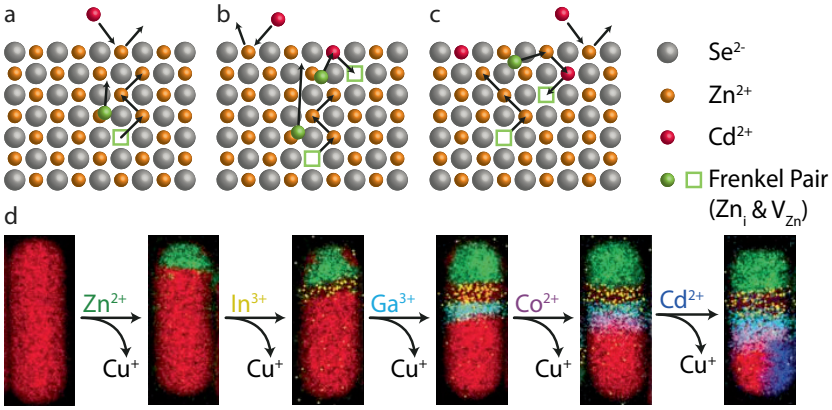

FIGURE 1.6: Ion exchange reactions. a–c) Simplified schematic depicting the ion exchange from ZnSe to CdSe via interstitials and vacancies, following the mechanism proposed by Groeneveld et. al..[89] b) Sequential ion exchange of a copper sulfide nanorod into a multiphase particle.[84] *Copyright note:*[4]

Based on these insights, many ion exchange reactions have been developed, thus expanding the already vast library of nanocrystals synthesized to date. Apart from complete conversion, partial conversion also allows to create alloys and spatially organize separate phases (i.e., core-shell) of an otherwise inaccessible complexity (Figure 1.6d).[83–85] First steps beyond the conversion of individual particles have been explored by converting nanoparticle films in combination with lithographic techniques to create patterns (Figure 1.7d).[34,85,95,96] In order to unleash the potential of ion exchange, there are two main challenges to overcome. First, the size limitations, which mostly arise from diffusion, make ion exchange impractical for microscopic and larger structures. Here the role of the anion is especially important as its larger size hampers diffusion. Second, ion exchange reactions are typically applied on the entire sample. Gaining spatial control over ion exchange reactions may also pave the way for alternatives to current lithographic approaches. Eventually, these advances could enable a seamless integration of ion exchange and self-assembly techniques, ultimately obtaining independent control over the shape and composition of materials.

[4]Copyright note: b) Adapted with permission.[84] Copyright 2020, AAAS.

1.5 Perovskites

The rise of semiconductors has set the foundation for the digital age.[97–99] Over time, the semiconductor industry continuously innovates to create smaller integrated circuits with increasing complexity and solar cells of higher efficiency.[100,101] The continuously increasing performance comes at the cost of requiring advanced, costly clean room facilities, thus limiting the accessibility of this research. A material class that has made semiconductor research, especially solar cell research, accessible to a broad group of scientists by requiring only minimal technological prerequisites are lead halide perovskite semiconductors.[102–104] Within a decade of being first implemented in a solar cell, efficiencies almost match those of silicon-based cells which have been researched for 60 years.[100]

While the term perovskite is often used synonymous for semiconducting lead halide perovskites, it refers to an ionic crystal structure ABX_3 in which A^+ and B^{2+} are cations of fundamentally different sizes, and X^- the anion (Figure 1.7a). This crystal structure was first recorded as mineral in 1839 (calcium titanium oxide). Remarkably, it is only since 2009 that this perovskite crystal structure got widespread attention due to the first implementation of methylammonium lead halides in a solar cell.[105,106] One of the most popular examples is $MAPbBr_3$ with methylammonium, lead, and bromide, respectively. Other common cations are formamidinium and cesium, while the halides are typically chloride, bromide, and iodide as well as mixtures thereof.[103] Unlike covalently bound semiconductors, their ionic nature allows for simple solution processing. Choices in the halide moiety enable straightforward adjustments in composition to tune the bandgap. It might be this ease in fabrication in combination with their excellent optoelectronic properties and tolerance to defects that have resulted in the manifold applications including devices such as LEDs, detectors and scintillators (Figure 1.7).[107–112] While solar cells only require continuous layers, these integrated devices also demand lateral patterning of complementary materials such as insulators and semiconductors of different bandgaps. Already a remarkable level of patterning control has been achieved, such as local tuning of the bandgap through ion exchange.[96,113] Moreover, spatial positioning of material has been achieved by techniques such as lithography, laser writing, inkjet printing, templates, and self-assembly of nanoparticles.[96,114–120] Overall, this highlights the potential for patterning perovskites in two dimensions as well as developing routes to sculpt perovskites in three dimensions.

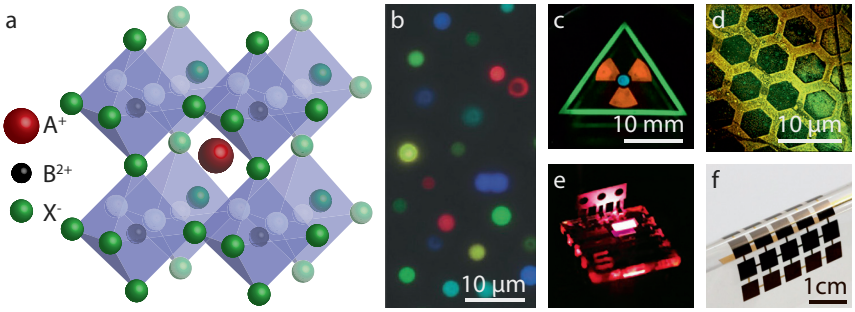

FIGURE 1.7: Lead halide perovskite semiconductors. a) Cubic perovskite crystal structure showing a methylammonium or formamidinium anion surrounded by four PbX_6 octahedra. b) $CsPbX_3$ mixed halide nano crystals under UV light, exhibiting fluorescence at different wavelengths depending on their composition.[121] c) $CsPbX_3$ perovskite emitting light under X-ray radiation, demonstrating the applicability in scintillators (detection of X-rays by conversion of X-rays into visible light, detectable by a conventional CCD).[107] d) Photoluminescence micrograph of $CsPbBr_3$ nanocrystalline film which was locally ion-exchanged to $CsPbI_3$, using X-ray lithography.[96] e) Methylammonium lead bromide-iodide LED.[122] f) Flexible perovskite solar cell.[120] *Copyright note:*[5]

1.6 Motivation and Outline

Self-assembly and ion exchange are two versatile concepts for the creation of complex architectures and control over the composition of materials. In this thesis, we pose three questions regarding the application of these concepts. First, how can we manipulate light with self-assembled $BaCO_3/SiO_2$ microarchitectures? Second, how can we use ion exchange reactions to replace the material inside these microarchitectures for a semiconductor? And third, what does it take to 'print' ion exchange reactions onto a material to control the composition of a material locally? This thesis addresses these questions experimentally through optical studies of self-assembled helices, ion exchange on microarchitectures, and patterned ion exchange reactions in thin films.

In **chapter 2**, we study the potential of self-assembled carbonate double helices to manipulate light. We incorporate fluorescent molecules into the structure and show that light emitted from these molecules is wave-guided and leaves the helix at the tip in a narrow beam. The helix thus acts as a directional emitter. Furthermore, light transmitted through the helix experiences circular retardance specific

[5]Copyright note: b) Adapted with permission.[121] Copyright 2017, John Wiley and Sons. c) Adapted with permission.[107] Copyright 2018, Springer Nature. d) Adapted with permission.[96] Copyright 2016, ACS. e) Adapted with permission.[122] Copyright 2014, Springer Nature. f) Adapted with permission.[120] Copyright 2020, Springer Nature.

to the handedness of the helix. We attribute this behavior to the chiral ordering of the birefringent barium carbonate nanocrystals within the helix. Collectively, these observations demonstrate the ability of self-assembly to hierarchically order matter into materials with emerging functionality.

In **chapter 3**, we present an approach to expand the $BaCO_3/SiO_2$ coprecipitation system to different materials by post-synthesis shape-preserving conversion reactions. We develop an ion exchange route that first replaces the barium for lead and then the carbonate for methylammonium halide, creating methylammonium lead halide, a semiconductor with outstanding optoelectronic performance. While ion exchange reactions are often developed for individual nanoparticles, the hierarchical nanocomposite layout of these architectures allowed us to exchange the material fully with retention of the intricate morphological features. We show that this approach can be transferred to other nanocomposites by applying it to the conversion of biominerals.

In **chapter 4**, we introduce the concept of ion exchange lithography (IEL). Based on the ion exchange reactions developed in chapter 3, we use methylammonium and formamidinium halides in solution as reactive "ink" and lead carbonate nanoparticle films as ion exchangeable "canvas". By spraying, stamping and painting the ink on the canvas we demonstrate controlled patterning of electrically insulating films and semiconductors with tunable optoelectronic properties. Moreover, we show that the IEL approach can be integrated into the fabrication of (opto)electronic devices such as light-emitting diodes (LED).

Overall, this thesis shows the potential of hierarchical self-assembly strategies to create ordered ensembles with emerging functionality. We explore their ability to manipulate light, as well as their advantages in ion exchange processes given by their architecture. With this, we decouple shape and composition in self-assembly of metal carbonates, expanding the material repertoire to state-of-the-art semiconductors. Finally, we develop a lithography method based on ion exchange reactions to create patterns that may open up new routes for the fabrication of integrated devices.

The Double Helix
Barium Carbonate and Silica, 2020
Sample: Lukas Helmbrecht
Imaging: Stefan Diller, Scientific Photography, Würzburg

CHAPTER 2

Circular Retardance and Directed Emission from Self-Assembled Microhelices

Published as:

Helmbrecht, L., Tan, M., Röhrich, R., Bistervels, M.H., Kessels, B.O., Koenderink, A.F., Kahr, B. and Noorduin, W.L., *Directed Emission from Self-Assembled Microhelices.* Advanced Functional Materials, 2020, 30, 1908218.

Bottom-up assembly can organize simple building blocks into complex architectures for light manipulation. The optical properties of self-assembled polycrystalline barium carbonate/silica double helices are studied using fluorescent Fourier and Mueller matrix microscopy. Helices doped with fluorescein direct light emission along the long axis of the microarchitecture. Furthermore, light transmission measured normal and parallel to the long axis exhibits twist sense-specific circular retardance (CR) and wave-guiding, respectively, albeit the measurements suffer from depolarization. The helices thus integrate highly directional emission with enantiomorph-specific polarization. This optical response emerges from the arrangement of nanoscopic mineral crystallites in the microscopic helix and demonstrates how bottom-up assembly can achieve ordering across multiple length scales to form complex functional materials.

2.1 Introduction

Material syntheses based on self-assembly have given rise to structures with unique mechanical, magnetic, electric, and optical properties.[2,7,25,27,30,31] Such bottom-up assembly strategies also enable hierarchical ordering of building blocks across multiple length scales, thereby offering the opportunity to integrate multiple functionalities within a single material. Helical-shaped nanocomposites formed from barium carbonate ($BaCO_3$) nanocrystals and amorphous silica (SiO_2) can put these ideas to the test. These bioinspired nanocomposites have been observed to self-assemble into highly intricate, yet controllable, three-dimensional (3D) shapes such as vases, stems, and helices, that can be further sculpted and chemically modified.[24,29,46–53,56] The structural layout of the helical composites has been studied in great detail: the rod-shaped nanocrystals are elongated along their c-axes and align parallel to one another while precessing tangentially around the helical axis, thus forming a chiral ensemble as shown in Figure 2.1.[29,47]

It is well-known that chiral assemblies of achiral building blocks can exhibit handedness-specific optical responses.[64,65] Hence, the intricately ordered, anisotropic medium of the helices suggests that these architectures may have optical properties absent in their building blocks alone.

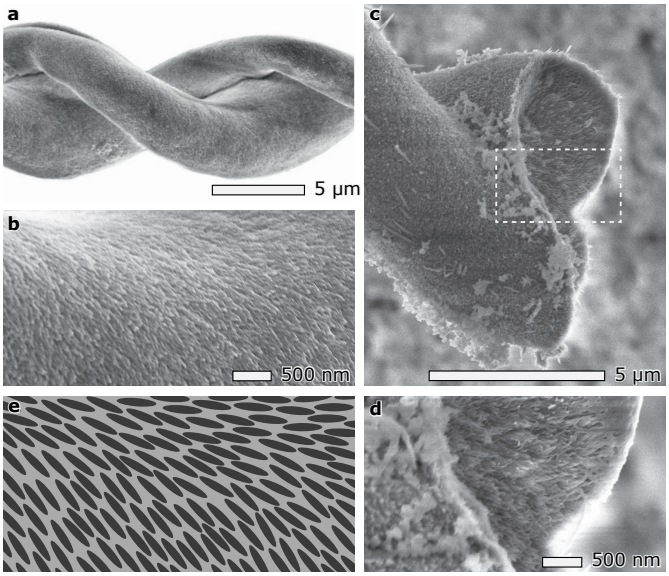

FIGURE 2.1: Visualization of the hierarchical organization of $BaCO_3/SiO_2$ helices. a) Electron micrograph of the microscale helical shape, b) The nanoscale twisting of the crystals on the outside of the helix. c) A cross-sectioned helix at higher magnification, d) showing the internal ordering of the nanocrystals. e) Schematic of the aligned nanocrystals.

The twisting matrix overlays linearly birefringent nanocrystals of $BaCO_3$ (n_α = 1.529, n_β = 1.676, n_γ = 1.677) in multiple directions with respect to incident wave vectors.[61,123] Moreover, the high refractive indices of the $BaCO_3/SiO_2$ ($n \approx 1.5$) medium may also affect total internal reflection and waveguiding at some optical frequencies.[49,124] Here, we study the optical properties of helices using fluorescent Fourier microscopy and Mueller matrix microscopy.[125,126]

2.2 Results and Discussion

2.2.1 Analyzing Directed Emission

$BaCO_3/SiO_2$ helices were synthesized according to a previously developed co-precipitation reaction (see Methods and Chapter 1.2 for details).[29] After growth of 1.5 hours, typical helices were approximately 40 µm long and 5 µm wide with a pitch of about 10 µm. Fluorescein was incorporated during growth to enable active light emission.[49] If a helix behaves as a wave-guide, scattered light within should be directed to the tip. We investigated the directional emission of individual helices with respect to their orientation, characterized by a polar tilt and azimuthal rotation (Θ_H and Φ_H respectively) relative to a glass cover slip substrate (Figure 2.2). These angles can be measured directly by scanning electron microscopy (SEM) (see Methods, section 2.4.2).

The direction of emitted light was determined using a home-built Fourier or k-space microscope (Figure 2.2a, Methods section 2.4.3).[127] The base of the helix was excited with a laser (λ = 490 nm). The emission (λ_E = 510 nm) was collected with a high numerical aperture objective (NA = 0.9), whose back focal plane (Fourier plane) was projected onto a CCD camera, where each pixel position in the image corresponds to an angle of incident light in real space (Figure 2.2a, c). Isotropic emission would give a diffuse Fourier image, whereas directed emission would produce a focused spot.

The polar emission angle (Θ_E) is calculated as distance of the emission peak (r_E) from the center of the Fourier plane (Figure 2.2c):

$$\Theta_E = arcsin(r_E/f) \tag{2.1}$$

where f is the focal length of the microscope objective (see Methods section 2.4.3 for derivation of equation 2.1). This enables a direct comparison of the tilt direction of the helix, as determined by SEM, with the direction of the emitted beam. Additionally, equation 2.1 gives the expected emission position in the Fourier plane from the polar tilt.

We analyzed the light emission for multiple helices (Figure 2.2a, Methods section 2.4.3). All microarchitectures show directional emission, as indicated by a well-defined spot in the Fourier plane. We define the position of the light spot

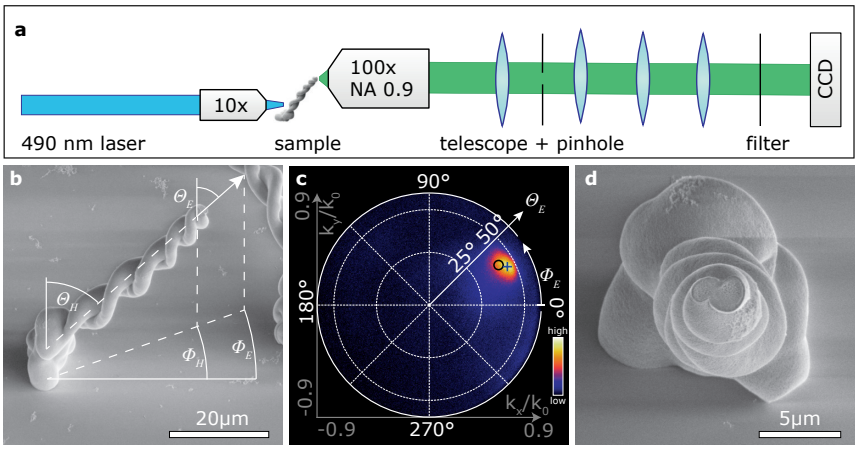

FIGURE 2.2: Directional light emission of self-assembled microhelices. a) Schematic of the Fourier microscopy setup. b) SEM image of a helix with polar tilt (Θ_H) and azimuthal rotation (Φ_H) relative to the substrate, compared with the polar angle of the emission (Θ_E) and the azimuthal rotation (Φ_E). c) Corresponding Fourier image of the emission, showing good agreement between orientation of the helix (marked with ○) and the direction of the emission (marked with +) (deviation of + 4° in Θ and – 4° in Φ). The outer circle corresponds to the maximum collection angle of 64.2° as given by the NA 0.9 of the objective. d) Top view of the helix showing the diameter and morphology of the tip.

as the location of maximum intensity (Figure 2.2c) and compare the direction of the emission with the orientation of the helices previously determined by SEM. As expected, rotating the sample led to a rotation of the spot in the Fourier plane. By combining the Fourier and SEM characterization, we found a close agreement between the emission direction (Θ_E = 40° and Φ_E = 30°) and the orientation of the helix (Θ_H = 44° and Φ_H = 26°) (Figure 2.2c).

Spot sizes were characterized in terms of the beaming half-angle (i.e., half the dispersion of the emission spot in the Fourier plane). This was 7.5° in the polar direction (Θ) and 11.5 °and in the azimuthal direction (Φ) (Figure 2.2c). A theoretical lower boundary of the beaming half-angle determined from a wave propagation simulation was 4° for light passing through a 2 µm diameter circular aperture, which is comparable to the smallest feature of the tip of the helix (Methods section 2.4.3).[128] The experimentally found beaming half-angle is close to the theoretical limit. The microscale morphology of the helix thus determines direction and dispersion of light emission.

2.2.2 Analyzing Circular Birefringence

We analyzed the optical polarization characteristics of enantiomorphous helices. The change in polarization of light transmitted through the helices can be measured using Mueller matrix polarimetry (Figure 2.3a). The instrument design is based on dual continuously rotating waveplates.[129–132] The polarization state of light incident on the sample is modulated by coupling a stationary linear polarizer to a rotating quarter-wave plate. The polarization state of light transmitted by the sample is subsequently analyzed by passing the beam through a rotating quarter-waveplate followed by a stationary polarizer. The time-dependent light intensity signal produced by the combination of polarization state generator (PSG) and polarization state analyzer (PSA) can be inverted to recover the Mueller matrix (**M**), a 4 × 4 real-valued transformation matrix that describes the optical properties of a sample.

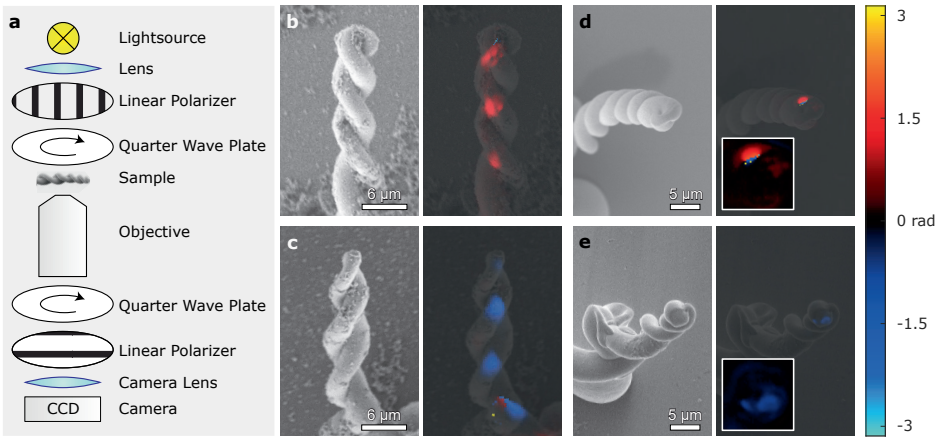

FIGURE 2.3: Circular retardance (CR) from $BaCO_3/SiO_2$ helices. a) Schematic of the Mueller Matrix microscope setup. b–c) Series of electron micrographs with CR overlaid on SEM image. A right-handed arrangement of 'ropes' (b) generates +CR while a plait of opposite handedness (c) generates –CR. d–e) Light transmitted from the tip exhibits +CR for left-handed structures (d), and –CR for right-handed structures (e). Insets in d) and e) show a 2x magnification of the tip

Light of any polarization state can be described by the Stokes vector (S), a four-element vector defined as $S = [I\ Q\ U\ V]^T$ where I is the total intensity, Q is the difference in intensity of light polarized along the x and y directions, U is the intensity difference of light polarized along ±45°, and V is the difference in intensity between left and right circularly polarized light. An input Stokes vector (S_{in}) can be transformed to an output Stokes vector (S_{out}) by **M**, so that $S_{out} = \mathbf{M}S_{in}$.

Circular retardance (CR), the angle by which the polarization vector of light is rotated when transmitted through a sample (range: $\pm\pi$), can be evaluated from the differential Mueller matrix, which is approximated from the matrix logarithm (**L**) of **M**:[129,133,134]

$$\mathbf{L} = \begin{bmatrix} -A & LE & LE' & CE \\ LE & -A & -CR & LR' \\ LE' & LR & -A & LR \\ CE & LR' & -LR & -A \end{bmatrix} \tag{2.2}$$

The process of obtaining **L** unscrambles mixed linear and circular anisotropies, providing a phenomenological understanding of the polarization transformations affected by the helices. (Figure 2.3b–e). Although this analysis is of limited utility when encountering depolarization, it is, in this case, a signature of the respective enantiomorphs.[135]

Ms were measured for helices whose long axes were parallel or orthogonal with respect to the light propagation direction. Measurements were collected at normal incidence transmission for a series of helices at a wavelength of 550 nm, which lies outside of the absorption band of fluorescein (Methods section 2.4.3). Viewed perpendicular to the helical axis, the rope-like strands of the double helix are overlaid every half period by an angle of $\approx 70°$. Light propagating orthogonally through a left-handed helix experiences a right-handed progression of anisotropic lamellae (Figure 2.3b) (as viewed from the detector). This generates a +CR, in other words, the incident plane of polarization is rotated clockwise (applying the normal convention for optical rotation whereby a dextrorotatory structure produces a clockwise rotation when looking at the light source). The converse is also true. In a right-handed helix, light encounters a left-handed arrangement of elements producing a levorotation (–CR) (Figure 2.3c). The maximum rotation in orthogonal transmission (up to 1.4 rad) was observed where the sample thickness is greatest (ca. 6 µm).

The CR observed in Figure 2.3b–c can be understood from the ordering of nanocrystals within the helix, in particular, the misorientation of anisotropic nanoparticles along the wave vector as it traverses the material. Skewed stacks of anisotropic lamellae are known as Reusch piles, after the scientist who used plates of mica to mimic the action of α-quartz on the azimuth of linearly polarized light passed along the optic axis.[64,65] Dispersion theory predicts that the sense of optical rotation depends on whether the wavelength of the illumination is greater or less than the helical pitch (P) of the structure. Here, P is greater than 550 nm. Therefore, we expect that for a right-handed ensemble the CR will be dextrorotary (positive), which is consistent with the experiment. The systematic dextrorotatory (red) signal in the false-color micrograph of Figure 2.3c might be a consequence of the inclination of this helix out of the sample plane compared with Figure 2.3b.

Measurements along the helical axis suffer from strong depolarization, which can be described using the degree of polarization (DOP):

$$DOP = \frac{\sqrt{Q^2 + U2 + V^2}}{I^2} \tag{2.3}$$

The low DOP values observed are a consequence, in part, of mismatched indices of refraction between the material and its surroundings (air); helices became dislodged when embedded in an index matching medium. Due to the low DOP, results have to be interpreted with care. Nevertheless, it is significant that the polarization responses were opposite for heterochiral helices. This provides a clue as to how the light is responding when traveling along the long axis. We presume that the helices behave as waveguides when light is transmitted through the tip; in other words, the sense of the light rotation follows the twist of the structure as in a cholesteric or twisted nematic liquid crystal.[62] Thus, a left-handed helix (Figure 2.3d), which rotates the plane of polarization clockwise, operates as a dextrorotary waveguide while a right-handed helix operates as a levorotatory waveguide (Figure 2.3e). Similar optical effects have been measured in twisted optical fibers, supporting the conclusion that nanocomposite helices of $BaCO_3/SiO_2$ function as waveguides.[136,137] When subjected to an elastooptic deformation, monomode fibers generate a CR of opposite handedness to the twist. A right-handed deformation produces a levorotation.

2.3 Conclusion

Self-assembled, microscopic $BaCO_3/SiO_2$ double helices display directional emission and enantiomorph-specific circular retardance (CR). Currently, the handedness and directionality of helices are set by spontaneous symmetry breaking that occurs in the early stages of the assembly process.[138] An exciting step forward would be to program the chirality and orientation of microarchitectures on the substrate surface by deliberately steering the assembly using top-down fabrication strategies and chiral auxiliaries.[139] In conclusion, helices emit highly directional light along their long axes, while affecting a differential refraction of left and right circularly polarized light. Normal to the helix axis, a CR is recorded that is best interpreted as a consequence of overlaid, misoriented, anisotropic lamellae. CR and directional emission originate from hierarchical ordering in helices, which intrinsically emerges from the self-assembly. Overall, these results demonstrate the potential of bottom-up processes to organize simple building blocks across multiple length scales for complex functional materials.

2.4 Methods

2.4.1 Growth of $BaCO_3/SiO_2$ Microhelices

Typically, 0.074 mg $BaCl_2$ and 0.016 g Na_2SiO_3 (Sigma Aldrich) were dissolved in 15 ml water. The pH was adjusted to 11.2 using HCl, and 21 mg of fluorescein was added. Glass substrates of 20 x 24 x 1 mm were mounted in a 100 ml beaker, and partially immersed with the growth solution before covering with a Petri dish. After 1.5 h, the glass substrates were removed and carefully rinsed with deionized water to isolate the microhelices. This procedure yields ca. 40 µm ensembles. These helices were found to be long enough for studying the optical effects of multiple twists, yet robust for transport.

2.4.2 Geometric Analysis of Microhelices

The orientation of each microhelix was determined relative to the substrate using an FEI Verios 460 scanning electron microscope. The polar angle θ_H was determined by orienting the sample stage such that the microhelix was parallel to the electron beam (Figure M2.2c).

2.4.3 Fourier Microscopy for Analyzing Directional Emission of Microhelices

Fourier Microscopy Setup

The Fourier microscope consists of the following components: (Figure M2.1a)

- Laser emitting at 490 nm, coupled to an optical fiber (SuperK EXTREME by NKT Photonics)
- Aperture to trim beam
- 470 nm/40 Bandpass (BP) filter to remove white light tail form laser
- 10x air objective to focus the light at the base of the microhelix
- Fluorescent sample on X-Y stage
- 100x air objective while measuring, NA = 0.9 (64.16° acceptance angle) (can be exchanged for a 10x objective during alignment)
- Beam splitter (removable) and white light source for white light imaging
- Telescope (two 50 mm lenses) with 300 µm pinhole in between to select the tip of the microhelix and discard scattered light
- Two lenses to project image on CCD (one removable to switch between Fourier and real space)
- 2x long pass LP filter 500 nm
- CCD (pco.panda 4.2 by PCO AG)

Data processing of Fourier Images for Directionality Analysis

The direction of light emission from the microarchitectures is analyzed using the Fourier Microscopy setup (Figure M2.1a). Directional emission from the helix creates a light spot on the Fourier plane. The relation between that position and the emission angle is described by the Abbe sine condition for aplanatic systems: $r = fsin\Theta$ (Figure M2.1d). We define: r_E as the radial distance of the emission peak from the center, Θ_{max} as the maximal acceptance angle of the objective, and r_{max} as the corresponding distance. Following the Abbe sine condition, the relation between the angle of emission Θ_E and the position of the emission on the Fourier plane is as follows:

$$\Theta_E = arcsin\left(\frac{r_E}{f}\right), \tag{M2.1}$$

with $r_{max} = f \cdot NA$, follows:

$$\Theta_E = arcsin\left(\frac{r_E \cdot NA}{r_{max}}\right), \tag{M2.2}$$

Alternatively:

$$\Theta_E = arcsin\left(\frac{k_E}{k_0}\right) \tag{M2.3}$$

where k_E is the wave vector of the emission and $k_0 = 2\pi/\lambda_E$ the free space wave vector.

The emission direction is calculated using a computer script (Python), which crops the Fourier image to the region of interest, determines the location of the maximum intensity, and derives the corresponding angles using equation M2.3. Additionally, the script marks the position of emission as expected from the helix' geometry.

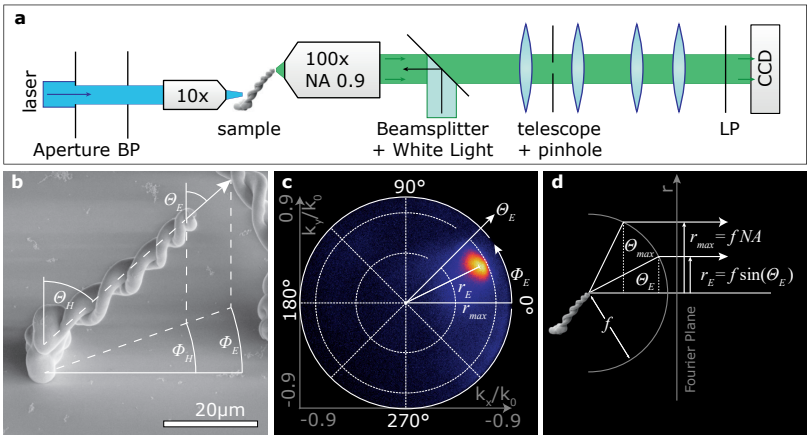

FIGURE M2.1: Fourier microscopy setup and ‚easurements. a) Fourier microscope. b) SEM image with angles of orientation (Θ_H, Φ_H) and emission (Θ_E, Φ_E). c) Measured Fourier image with r_E and r_{max} (see equations M2.1-M2.3). d) Schematic relation between the emission angle Θ_E, and the position on the Fourier plane.

Additional Directionality Measurement

Supplementary to the specimen shown in Figure 2.2 in the main text, we here present another example. In compliance with the previous microhelix, this one also shows a narrow emission angle and a good agreement between orientation and direction of emission (Figure M2.2).

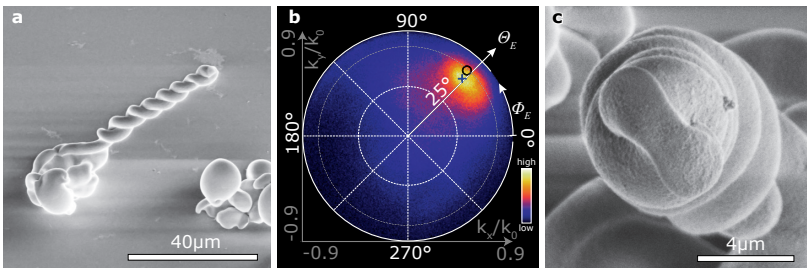

FIGURE M2.2: Directional light emission of a self-assembled microhelix. a) SEM image, and b) corresponding Fourier image of the emission, showing good agreement between orientation of the helix (marked with ○) and the direction of the emission (marked with +). c) Top view of the helix.

Analysis of the dispersion of the emission

The dispersion of the emission is determined from the spot size in the Fourier image. The boundary of this spot is obtained by applying a 1/e threshold. We measure a spot size of 23° in the Φ-direction and 15° in the θ-direction for the helix in Figure 2.2 in the main text, therefore giving a beaming half angle of 11.5° and 7.5° respectively (Figure M2.3a). In the simulation, a light field with a Gaussian profile was passed through a circular aperture with a 2 µm diameter and numerically propagated using the convolution-based Fresnel function in the "LightPipes" Python package to the back-focal plane of a lens with a 100 µm focal length.[128] This small lens focal length was chosen in order to decrease the size difference between aperture and back-focal plane, which greatly reduces the resolution requirements and, therefore, the simulation time. From the resulting intensity profile (Figure M2.3b), we derive a beaming half angle of 4° (Figure M2.3c).

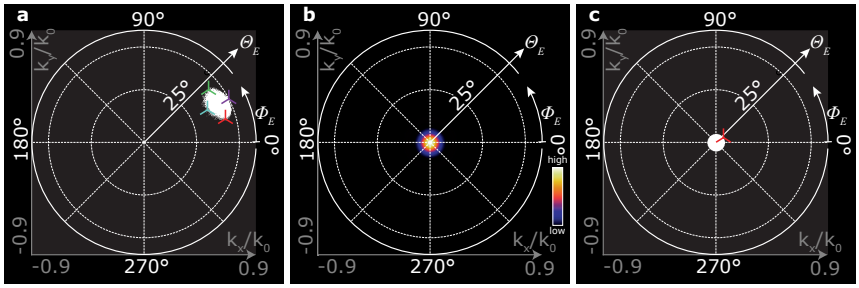

FIGURE M2.3: Analysis of the beaming half angle. a) Experimentally obtained spot size in the Fourier plane (1/e threshold is applied to the data of Figure M2.1c). The markers indicate the edges of the spot. The spread in the Φ-direction is 23° (green: Θ = 42°, Φ = 39°; red: Θ = 43°, Φ = 16°), and the spread in the Θ-direction is 15°(purple: Θ = 50°, Φ = 27°; cyan: Θ = 35°, Φ = 27°). b) Simulated light field resulting from a 2 µm aperture, c) applying a 1/e threshold shows a beaming half angle of 4°.

2.4.4 Mueller Matrix Microscopy

The concept of the dual rotating retarder Mueller matrix polarimeter was first described by Azzam in 1978.[129] Our system is built by modifying the accessory slots of an inverted commercial microscope frame (Zeiss Z1 Observer). In this design, monochromatic light, represented by the Stokes vector $S_{in} = [1000]^T$, is transmitted through a linear polarizer ($\mathbf{P_1}$) coupled to a continuously rotating waveplate ($\mathbf{M_{R1}}$). Together, $\mathbf{P_1}$ and $\mathbf{M_{R1}}$ form the polarization state generator (PSG). After transmission through the sample, $\mathbf{M_s}$, light is gathered by an objective lens and sent to the polarization state analyzer (PSA), composed of a continuously rotating waveplate, $\mathbf{M_{R2}}$, followed by a fixed linear polarizer, $\mathbf{P_2}$. The continuous

rotation of the waveplate elements creates a time-dependent signal at the detector that encodes for all 16 Mueller matrix elements, thereby completely describing the polarization properties of a sample. The time-dependent scalar intensity signal measured at the detector can be represented as:

$$I(t) = S_{out}\mathbf{P_2}\mathbf{M_{R2}}(\mathbf{t})\mathbf{M_s}\mathbf{M_{R1}}(\mathbf{t})\mathbf{P_1}\mathbf{S_{in}} \tag{M2.4}$$

Expansion of the scalar intensity function as a Fourier series reveals that $\mathbf{I}(\mathbf{t})$ has twelve frequency components.[129,132] If the period and frame rate are appropriately chosen, digital demodulation of the time varying signal recovers the complete Mueller matrix of the sample,

$$\mathbf{M_s} = \begin{bmatrix} m_{11} & m_{12} & m_{13} & m_{14} \\ m_{21} & m_{22} & m_{23} & m_{24} \\ m_{31} & m_{32} & m_{33} & m_{34} \\ m_{41} & m_{42} & m_{43} & m_{44} \end{bmatrix} \tag{M2.5}$$

The Mueller matrix was measured using a Mueller matrix microscope (Figure 2.3 main text). The technical details of our instrument are published in full elsewhere.[130–132]The circular retardance measurements shown in Figure 2.3 were obtained from the normalized Mueller matrix measurements shown in Figure M2.4.

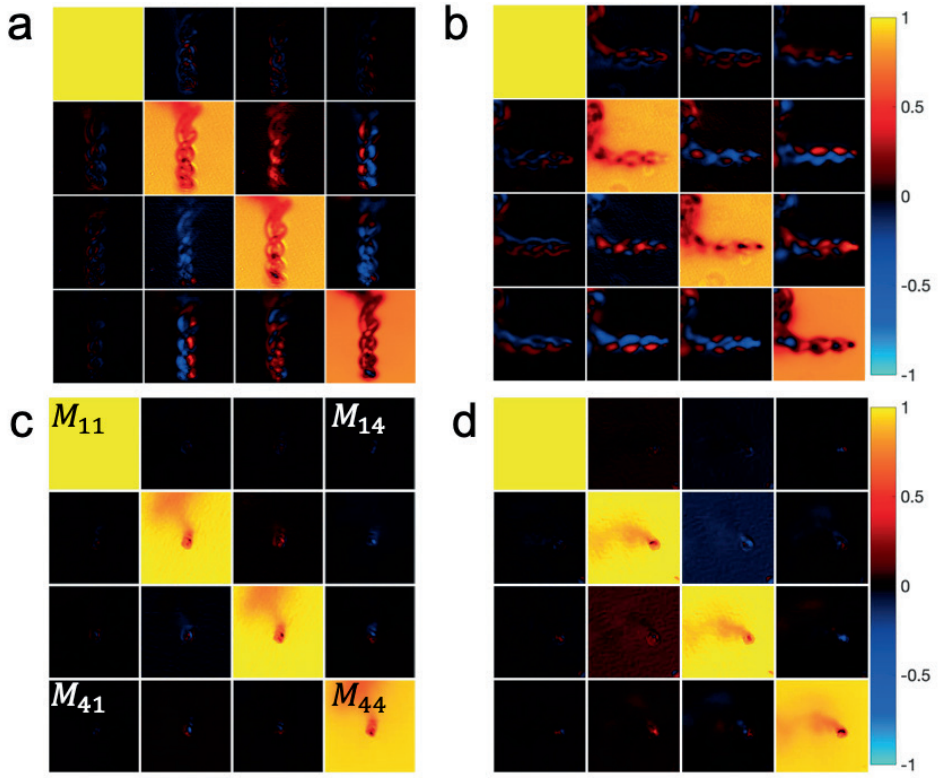

FIGURE M2.4: Normalized Mueller matrix measurements (transmission, $\lambda = 550\,\text{nm}$) of a left-handed helix (a and c) and a right-handed helix (b and d). The helices in a and b are laying flat on the substrate. Thus, the direction of light propagation is perpendicular to the long axis of the helix. In contrast, the helices in c and d are nearly orthogonal with respect to the substrate, and light is transmitted parallel to the long axis of the helices.

Transformation
Fluorescent Paint on Sand Dollar Skeletons, 2018
Henk-Jan Boluijt and Lukas Helmbrecht

CHAPTER 3

3D Perovskite Sculptures via Self-Assembly and Ion Exchange

Published as:

Holtus, T., Helmbrecht, L., Hendrikse, H.C., Baglai, I., Meuret, S., Adhyaksa, G.W., Garnett, E.C. and Noorduin, W.L., *Shape-preserving transformation of carbonate minerals into lead halide perovskite semiconductors based on ion exchange/insertion reactions.* Nature chemistry, 2018, 10(7), pp.740-745.
Tim Holtus, Lukas Helmbrecht, and Hans C. Hendrikse contributed equally.

Biological and bio-inspired mineralization processes yield a variety of three-dimensional structures with relevance for fields such as photonics, electronics, and photovoltaics. However, these processes are only compatible with specific material compositions, often carbonate salts, thereby hampering widespread applications. In this chapter, we present a strategy to convert a wide range of metal carbonate microarchitectures into lead halide perovskite semiconductors with tunable bandgaps, while preserving the 3D shape. First, we introduce lead ions by cation exchange. Second, we use carbonate as a leaving group, facilitating anion exchange with halide, which is followed rapidly by methylammonium insertion to form the perovskite. As proof of principle, pre-programmed carbonate salt shapes such as vases, coral-like forms, and helices are transformed into perovskites while preserving the morphology and crystallinity of the initial microarchitectures. This approach also readily converts calcium carbonate biominerals into semiconductors, furnishing biological and programmable synthetic shapes with the performance of artificial compositions such as perovskite-based semiconductors.

3.1 Introduction

Strategies that offer independent control over 3D shape and composition of nano- and micro-scale architectures are of fundamental interest and hold relevance for fields ranging from optics and sensing to microelectronics and catalysis.[17,30,31,49,140–144] Carbonate salts, including the most abundant biomineral calcium carbonate, give access to an impressive catalogue of exquisitely sculpted crystalline shapes that can be created via biological and bio-inspired mineralization processes with a rational control over form.[13,24,26,29,30,49,140,145] However, these carbonate salts have limited application potential, due to the properties of their chemical composition. One way to overcome this inherent limitation is by converting previously formed shapes into a desired composition while preserving the original shape. Both biological and synthetic shapes have already been converted into functional compositions using oxidation/reduction reactions, which give access to a range of metals and metal oxides.[144,146,147] However, many compositions that can act as conductors, semiconductors, and catalysts cannot be synthesized using these reactions. An entirely different and potentially more versatile approach to tune the material composition by choice is offered by ion exchange reactions. These reactions enable the conversion of the ionic composition of nanocrystals—and superlattices thereof—into a wide range of compositions, whilst preserving the original morphology.[34,36,83,85,86,88,91,147–149] Cation exchange has already been demonstrated for many different ions.[83] Anion exchange, on the contrary, remains challenging as the larger size and lower diffusivity of anions hinder proper conversions. As a result, only a few examples of successful anion exchange reactions have been reported,[86,94] and general routes to exchange anions still need to be developed. Here we demonstrate a versatile pathway towards complete cationic and anionic exchange with full shape preservation, starting from a variety of biological and bio-inspired artificial structures. Two key insights underlie this approach. Firstly, the anionic carbonate group in biological and bio-inspired minerals can act as a remarkably good leaving group, offering a promising way to introduce new anions in a relatively facile and generic manner. Secondly, many biomineralized architectures are composed of nanocomposites, i.e., materials composed of an ensemble of nanocrystals embedded in an amorphous matrix, and this nanocrystalline nature may readily enable the tuning of their composition using ion exxchange reactions. This applies not only to biologically formed structures but also to the wide variety of synthetic bioinspired materials, for which numerous strategies exist to yield rationally designed shape-controlled hybrid materials.[13,17,24,26,29–31,49,141,145] Exploiting these two unique advantages will thus enable the possibility to first program the shape in a carbonate salt nanocomposite and subsequently apply a cascade of cation and anion conversion reactions to obtain a functional-material composition, e.g. a semiconductor or catalyst, of the exact same shape.

To demonstrate the proof-of-principle we chose methylammonium lead-halide perovskites ($CH_3NH_3PbX_3$) as target materials. The exceptional performance of these semiconductors for solar cells, water-splitting, lasers, LEDs and radiation detectors along with their facile synthesis is revolutionizing the prospects of next-generation optoelectronics.[150] So far most studies have been performed on thin films, but control over the 3D microscale morphology of perovskites may be essential for developing the next generation of transistors and directed light-absorption and emission.[151,152] Despite the recent progress in casting methods,[153,154] growth of arbitrary perovskite shapes has remained challenging, and highlights the need for new strategies to gain independent control over shape and composition.

In this work, we introduce a simple two-step reaction scheme for converting carbonate architectures into lead-halide perovskites (Figure 3.1). Starting from biological and programmable synthetic carbonate-salt architectures, we convert these into perovskites with a tunable bandgap and a charge carrier lifetime on par with state-of-the-art perovskite thin films, while at the same time inheriting the 3D shape, delicate features, and crystallinity of the starting architecture.

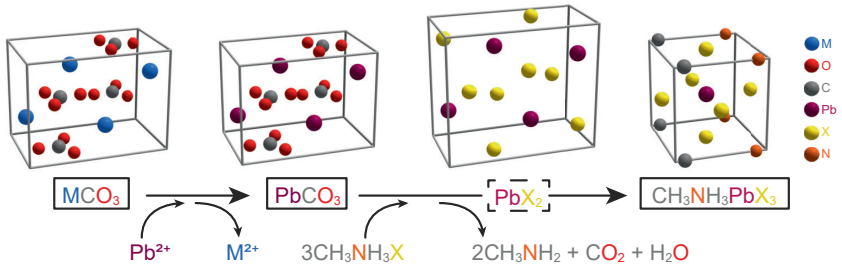

FIGURE 3.1: reaction scheme for the synthesis of $CH_3NH_3PbX_3$ perovskites from carbonate salts (MCO_3). The reaction of $PbCO_3$ with CH_3NH_3X results in the direct formation of $CH_3NH_3PbX_3$ via intermediate PbX_2 (dashed box). Cation organization in the crystal unit cell of the carbonate salts and PbX_2 is similar, thereby facilitating the cation exchange reaction. The sizes of the unit cells are scaled for the conversion of $BaCO_3$ to $CH_3NH_3PbBr_3$. M (blue) = Ca, Ba or Sr; X (yellow) = Cl, Br or I; Pb (purple), O (red), N (orange), C and H (both grey).

3.2 Results and Discussion

Conversion of carbonate salts into perovskites requires a complete chemical and structural transformation involving the exchange of the cations and the notoriously difficult exchange of anions, insertion of methylammonium halide (CH_3NH_3X), and rearrangement of the crystal unit cell, while in all steps minimizing the distortion of the crystal lattices (Figure 3.1). A key insight for the development of our route is that PbX_2, a commonly used precursor for synthesizing lead halide

perovskites,[155,156] crystallizes in the same orthorhombic crystal structure as $PbCO_3$ (cerrusite) and many other carbonate salts MCO_3 (with M = i.e. Ba, Sr, or Ca in the witherite, strontianite, and aragonite crystal structures, respectively). More explicitly, the metal ions in the crystal structures of PbX_2, $PbCO_3$ and MCO_3 are in the same position, and the dimensions of the unit cells are closely matched, with the length of the unit cell axes changing typically less than 10%. Additionally, the carbonate group can act as a good leaving group for facilitating the insertion of the halides into the $PbCO_3$ structure. Our two-step reaction scheme thus allows us to synthesize lead-halide perovskites from arbitrarily chosen metal carbonate architectures by first exchanging the metal ions for lead, followed by the reaction of the carbonate ions with methylammonium halides to yield the corresponding perovskite directly.

Prior to performing the conversion reaction, we program the carbonate shape into the desired target architecture. For the proof-of-principle, we use the bio-inspired co-precipitation of barium and strontium carbonate nanocrystals with silica. This nanocomposite system offers a pragmatic platform for developing a wide selection of micro-sized 3D geometries including vase, helix, and coral shapes, which can be formed by rationally modulating the reaction conditions such as temperature, pH and CO_2 concentration.[24,29,49] We illustrate the concept of the conversion reactions on coral-like shapes of barium carbonate and silica ($BaCO_3/SiO_2$) (Figure 3.2a, see Methods 3.4.1 for details).

In the first step, we exchange the Ba^{2+} for Pb^{2+} while preserving the shape of the original microarchitectures (Figure 3.2). During this exchange reaction, it is essential to prevent the dissolution of $BaCO_3$ and subsequent nucleation of $PbCO_3$, as such dissolution/recrystallization process hinders preservation of the shape.[157] Since the dissolution/recrystallization is relatively slow for high concentrations of Pb^{2+}, we perform the reaction in a nearly saturated aqueous solution of 0.9 M $Pb(NO_3)_2$ for 30–60 seconds in the absence of CO_2. This reaction is rapidly driven to completion due to the high concentration of Pb^{2+} and because the thermodynamic stability of the resulting $PbCO_3$ is higher, as indicated by the solubility product of $PbCO_3$ ($K_{sp} = 7.4\times10^{-14}$), which is orders of magnitude lower than that of $BaCO_3$ ($K_{sp} = 2.58 \times10^{-9}$).[85,158] Additionally, the similarities between the orthorhombic crystals structures of both $BaCO_3$ and $PbCO_3$ minimize distortion of the unit cell during the conversion (Figure 3.1). Energy Dispersive X-ray Spectroscopy (EDS) confirms the virtually complete exchange from Ba^{2+} to $Pb2^{2+}$ throughout the interior of the microarchitectures (>98 at.%, Figure 3.1, Methods 3.4.6). As expected, the orthorhombic crystal structure is maintained during the conversion of $BaCO_3$ into $PbCO_3$, which can be concluded from the nearly identical X-Ray powder diffraction (XRPD) data. Scanning Electron Microscopy (SEM) reveals the preservation of the entire architecture with nanoscale fidelity, while even the initial crystallographic alignment along the c-axis of the nanocrystals is retained according to the Maltese cross birefringent pattern of both the $BaCO_3$

and $PbCO_3$ using polarization microscopy (Methods 3.4.7).[24] This preservation of nanoscale features and crystallographic orientation suggests a transformation in which each individual crystal of one phase transforms into an individual crystal of a different phase while inheriting its orientation from the original crystal, thus constituting an additional level of complexity over dissolution/recrystallization mechanisms.

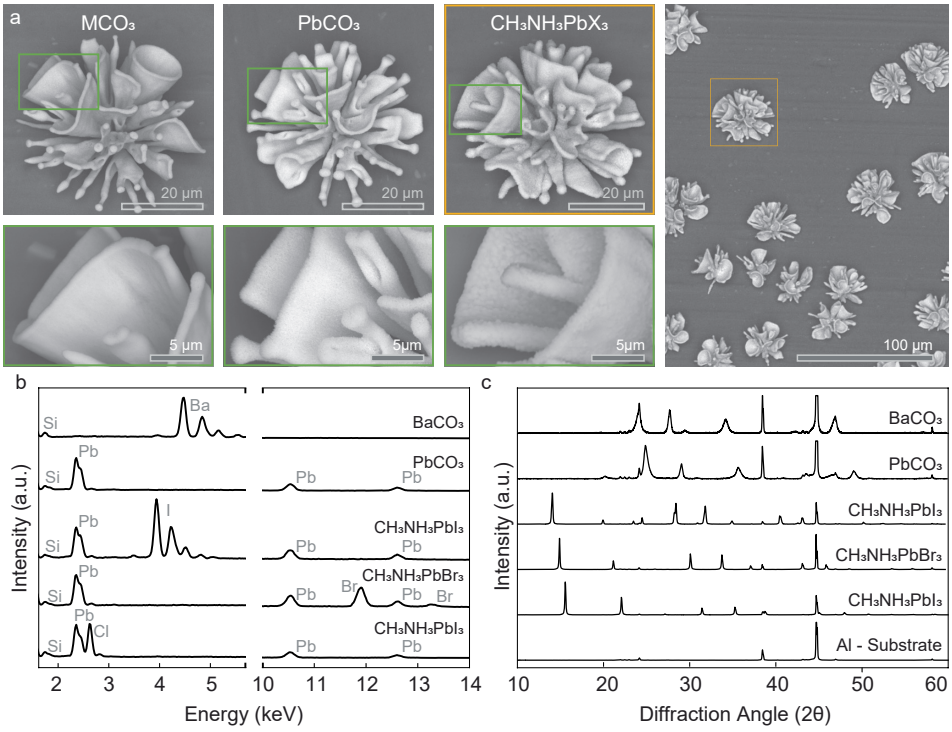

FIGURE 3.2: Conversion of metal carbonate microarchitectures into $CH_3NH_3PbX_3$ perovskites. a) Scanning electron microscope (SEM) images of the sequential reaction products, and overview images of the final perovskite product, shown for the conversion of $BaCO_3$ into $CH_3NH_3PbBr_3$ (see Methods 3.4.3 and Figure M3.1 for details and SEM images of the $CH_3NH_3PbI_3$ and $CH_3NH_3PbCl_3$ microarchitectures, respectively). b) Energy dispersion spectroscopy of microarchitectures showing the conversion of $BaCO_3$ into $PbCO_3$ and the final product $CH_3NH_3PbX_3$. c) X-ray powder diffraction data for microarchitectures showing the conversion of $BaCO_3$ (witherite) into $PbCO_3$ (cerrusite) and the final product $CH_3NH_3PbX_3$.

In the second step, we convert the resulting $PbCO_3$ architectures directly into the desired $CH_3NH_3PbX_3$ perovskite. The required exchange of anions has remained challenging in other systems thus far since the larger size and lower

diffusivity of anions often leads to sluggish conversions and poor retention of the morphology.[83] Besides replacing the carbonate with the desired halide-anion X (X = Cl, Br or I), the reaction to perovskite requires the well-established insertion of CH_3NH_3X and rearranging the crystal structure to yield the perovskite.[155] We here address these challenges in a one-pot conversion by exposing the $PbCO_3$ architectures to an excess of gaseous CH_3NH_3X at 120 °C for ca. 6 hours, which results in the direct formation of the desired perovskite ($CH_3NH_3PbX_3$). Characterization of the resulting architectures shows excellent conversion of $PbCO_3$ into the desired perovskite while retaining both the shape and fine features of the starting microarchitectures (Figure 3.2). The proposed reaction cascade is as follows:

$$PbCO_3(s) + 2CH_3NH_3X(g) \rightleftharpoons$$
$$PbX_2(s) + H_2O(g) + CO_2(g) + 2CH_3NH_2(g) \tag{3.1}$$
$$PbX_2(s) + CH_3NH_3X(g) \rightleftharpoons CH_3NH_3PbX_3(s). \tag{3.2}$$

In the first step, the removal of H_2O, CO_2 and CH_3NH_2 from the reaction mixture drives the reaction to completion, which is consistent with Le Chatelier's principle.[93] Additionally, the removal of water prevents the undesired decomposition of the perovskite, although small concentrations of water may improve the quality of the perovskite by lowering the defect density.[159–161] In the second step, the excess amount of CH_3NH_3X pushes the reaction of the intermediate PbX_2 to the perovskite.

To confirm the proposed reaction mechanism, we first develop a method for methylamine CH_3NH_2 detection. For this, we use a UV-light absorbing aromatic aldehyde that reacts with methylamine to form an imine that can be detected by HPLC-UV (High performance liquid chromatograph coupled to a UV-detector, see Methods 3.5.3 for details). This analysis shows that methylamine is released during the conversion of $PbCO_3$ to the perovskite, in agreement with the first step of the proposed mechanism. Consistent with this mechanism, we can also gain direct access to the PbX_2 intermediate by reacting $PbCO_3$ microarchitectures with KI under acidic conditions to obtain the corresponding PbI_2 microarchitectures (Methods 3.5.6). In the second step CH_3NH_3X is inserted into PbX_2 to form $CH_3NH_3PbX_3$. This reaction is already well documented for pure PbX_2 crystals.[155] Using the microarchitectures of PbI_2 we also confirm that the microarchitectures can undergo this insertion reaction with CH_3NH_3I to form the corresponding $CH_3NH_3PbI_3$ architecture. Finally, we qualitatively investigate the relative reaction rates of the two consecutive reaction steps by partially reacting $PbCO_3$ microarchitectures to $CH_3NH_3PbX_3$ according to the one-pot conversion scheme. Analysis of these microarchitectures using XRD show no detectable amounts of the reaction intermediate PbX_2, suggesting that the anion exchange of $PbCO_3$ to PbX_2

(step 1) is relatively slow compared to the conversion of PbX_2 to $CH_3NH_3PbX_3$ (step 2).

The generality of our reaction scheme allows us to synthesize a range of perovskites starting from a wide choice of carbonate compounds. To demonstrate this, we successfully convert microarchitectures of $BaCO_3$, $SrCO_3$, and $CaCO_3$ into the corresponding chloride, bromide, and iodide perovskites (Figure 3.2b, c, and Methods). It should be noted that the silica (20–25 at.% of the entire composition) is inert during the entire sequence of conversions, and merely required for controlling the shape of the original MCO_3 microarchitectures before we start with the conversions.[24,29,49] However, during the conversions, the silica matrix can assist in stabilizing and maintaining the overall micro shape by acting as a scaffold and by hindering ripening of the nanocrystals.

To verify the quality of our 3D shaped perovskites and the potential for our approach in optoelectronic applications, we benchmark the photoluminescence (PL) spectra and PL lifetime of our 3D halide-perovskite microarchitectures against already reported standard thin-film perovskites. Our 3D perovskites show narrow PL emission, with the peak wavelength tunable from the blue into the near-infrared by selecting the methylammonium halide precursor (Figure 3.3a), comparable to what has been reported in the literature for thin-film perovskites.[156] The photoluminescence lifetime of 28 ns for $CH_3NH_3PbBr_3$ microarchitectures is also on par with standard material preparation methods of thin films (Figure 3.3b).[156] We also see excellent PL uniformity both within and across large fields of halide-perovskite microarchitectures, confirming the complete conversion of the samples (Figure 3.3c). Our perovskites thus perform comparable to state-of-the-art thin-film perovskites, while offering the ability to straightforwardly program the 3D shape.

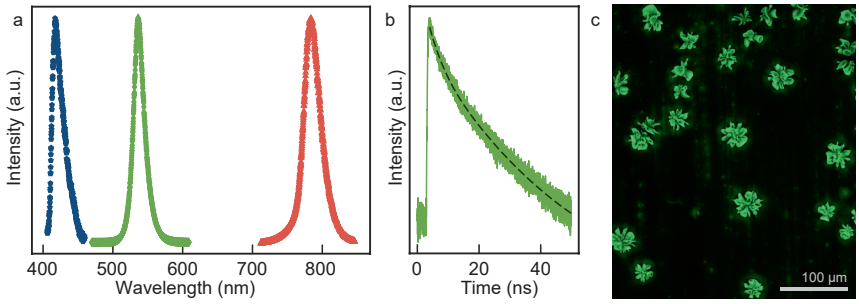

FIGURE 3.3: Photoluminescence of perovskite microarchitectures. a) Photoluminescence of coral-shaped synthetic microarchitectures of lead halide perovskites $CH_3NH_3PbX_3$, X = Cl (blue trace), Br (green trace) and I (red trace), measured with excitation wavelengths of 365 nm, 405 nm and 532 nm, respectively. b) Photoluminescence lifetime of a $CH_3NH_3PbBr_3$ microarchitectures. c) Overlay image of SEM and corresponding fluorescence microscopy image of a field of $CH_3NH_3PbBr_3$ coral shapes.

Since our conversion process is to a large extent independent of the microscopic form of the mineralized architecture, a wide variety of perovskite shapes can be synthesized by first programming the shape of the starting carbonate microarchitectures and subsequently converting them into lead-halide perovskite materials.[29,49] To illustrate the versatility of our concept, we preprogram different morphologies by modulating the reaction conditions such as pH, temperature and CO_2 concentration during the co-precipitation process of carbonate and silica (see Methods 3.4.1 for details). Subsequently, these microarchitectures can be converted to perovskites with a tunable bandgap based on the choice of methylammonium halide precursor. The photoluminescence can be seen with excellent spatial resolution in the cathodoluminescence (CL) images of a selection of perovskite helices, trumpets, spiked corals, and vases (Figure 3.4).

The colors of the CL images in Figure 3.4a–e correspond to the real color of light emitted from the perovskite microarchitectures (peak wavelength), showing the tunability of the bandgap by selecting the methylammonium halide precursor. Our reaction scheme thus enables the synthesis of a vast repertoire of programmable 3D perovskites with independent control over the micro-shape and material composition.

Our simple and flexible conversion approach also applies to naturally occurring biomineral architectures made of $CaCO_3$, many of which have a comparable nanocrystalline layout and material composition to the artificially synthesized carbonate shapes.[13,26,145] We illustrate this concept by converting a $6\times15\times3$ mm section of the highly intricate aragonite architecture of a cuttlefish bone (from Sepia officinalis) into perovskite, while retaining even the fine structure of the sub-micrometer-thin lamella (Figure 3.4f, for larger samples see Methods Figure M3.2). The epitaxial relationship between aragonite and the most common $CaCO_3$ polymorph, calcite, suggests that these biominerals can be converted as well. We confirm this by converting a 3.5 cm sized calcite shell of a sand dollar (Mellita isometra) into $CH_3NH_3PbBr_3$. To speed up the reaction rate due to the slow mass transport in the gas phase reaction, we perform the conversion of $PbCO_3$ into perovskite in a solution containing the methylammonium halide precursor instead of the gas-phase reaction. Even though a low pH can deteriorate perovskites, we here use acidic conditions to turn the carbonate of $PbCO_3$ into a good leaving group and speed up the conversion reaction. To directly visualize the transformation, we use UV illumination to observe the light emission from the forming perovskite. The reaction is remarkably fast, with a 3.5 cm sand dollar converting in less than one minute, as is clearly visible from the bright fluorescent true-color camera images (Figure 3.4g) and Movie in the SI of this publication.[48] This experiment also gives insight in the conversion depth that can be achieved: for a sand dollar with a thickness of ca. 1 mm, we find that the outer 100 µm is converted into perovskite, giving rise to a core-shell structure with a semiconductor on the outside and an insulating $CaCO_3$ interior (Figure 3.3 and Methods Figure M3.2). Thus, our

transformation scheme is also effective on macroscopic scales, yet preserves even the finest features with sub-micrometer fidelity.

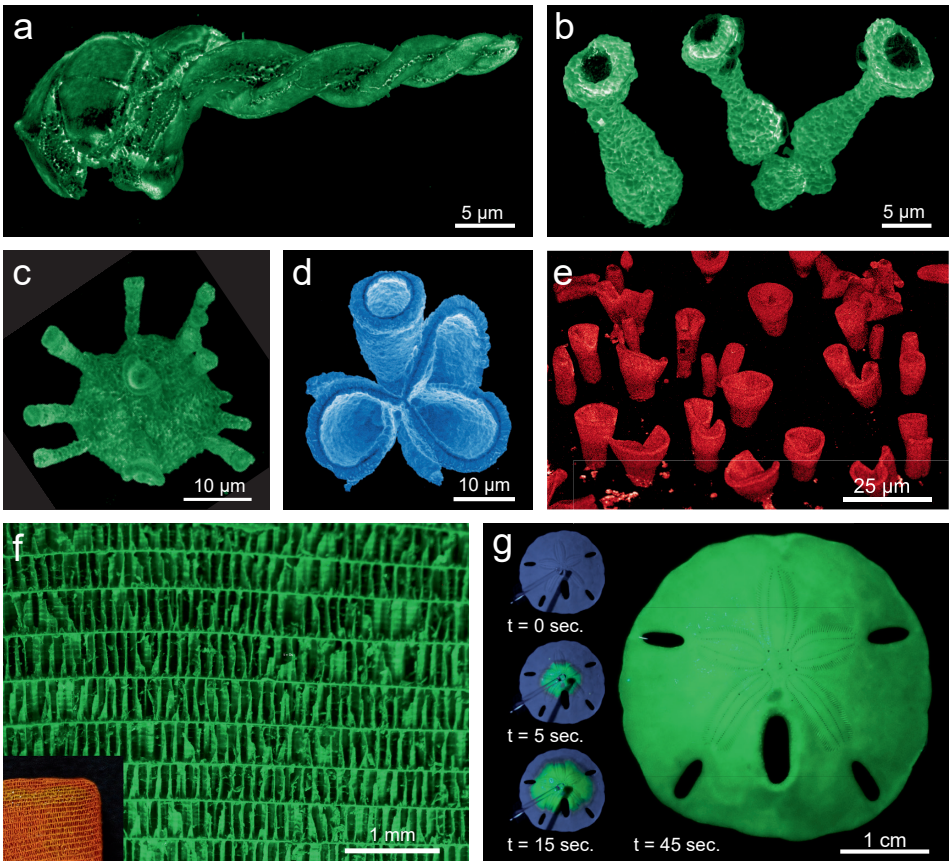

FIGURE 3.4: Complex arbitrarily shaped perovskites from synthetic and biological mineral architectures. a–c): Double helix a) trumpet b) and spiked-coral c) shapes of $CH_3NH_3PbBr_3$. d) $CH_3NH_3PbCl_3$ coral shape. e) Field of $CH_3NH_3PbI_3$ vase shapes. The colours chosen for the colour scale represent the emission range of the measured cathodoluminescence, with lighter colours corresponding to higher emission intensity. f) Fluorescence microscopy image of a cuttlefish bone converted into $CH_3NH_3PbBr_3$. Inset: photograph under daylight illumination (image width 0.5 cm). g) Time-lapse fluorescence photographs under UV illumination at 365 nm of a sand dollar converting in 45 s from $PbCO_3$ into $CH_3NH_3PbBr_3$.

3.3 Summary

We have presented a platform to gain independent control over both the shape and composition of 3D functional materials, using a two-step reaction scheme that converts biological and programmable synthetic carbonate salt architectures into perovskites. With calcium carbonate being the most abundant biomineral in nature, our reaction thus gives access to the vast catalogue of biological architectures, leveraging nature's exquisite morphogenesis strategies with chemical conversion into broadly applicable functional materials.[13,17,24,26,29–31,49,140,141,143–146,162] Furthermore, the control offered by bio-inspired synthetic crystallization strategies over parameters such as nucleation position, shape and crystal size can now be combined with the unprecedented material performance of artificially made halide perovskites with tunable optical and electronic properties. Finally, these principles can readily be extended to the synthesis of other functional materials, potentially including other semiconductors such as lead-free perovskites, conductors, and catalysts.

3.4 Methods

3.4.1 Growth of $BaCO_3$ and $SrCO_3$ Microarchitectures

Typically, an aluminum plate (2×2 cm) was vertically positioned in a 100 ml beaker containing 0.074 g $BaCl_2$ or 0.084 g $SrCl_2$ and 0.016 g Na_2SiO_3 (all obtained from Sigma Aldrich) in 15 ml of water. The reaction vessel was loosely covered with a Petri dish to allow CO_2 from the air to slowly diffuse into the reaction mixture. The pH was measured using a VWR Scientific 8005 pH meter and adjusted by adding HCl or NaOH to a pH of 11.8 for the growth of stem, vase and coral-like microarchitectures (Figure 3.2, Figure 3.3 and Figure 3.4d, e) or to a pH of 11.2 for the growth of helical microarchitectures (Figure 3.4a). Typical growth times ranged between 1.5–2.0 hours after which the reaction was stopped by carefully washing the sample with deionized water. Then the microarchitectures were converted into $PbCO_3/SiO_2$ (see section 3.4.3). The resulting microarchitectures were analyzed by XRD, SEM/EDS, and optical microscopy.

Trumpet shapes in Figure 3.4b were grown in an aqueous solution containing 0.084 g $SrCl_2$ and 0.016 g Na_2SiO_3 in 15 ml of water. The reaction vessel was loosely covered with a Petri dish to allow CO_2 from the air to slowly diffuse into the reaction mixture. After ca. 1.5 hours, the Petri dish was carefully removed for 2 minutes, allowing an increased influx of CO_2 to split the stem-like architectures into vases and then placed back on the beaker. After 20 minutes, the beaker was carefully immersed in an ice bath to cool down the reaction solution to 4 °C for 10 minutes to thicken the rim of the growing trumpets. The reaction was stopped by carefully washing the sample with deionized water. Then the microarchitectures were converted into $PbCO_3/SiO_2$.

The microarchitecture in Figure 3.4c was shaped by growing it in an aqueous solution containing 0.084 g $SrCl_2$ and 0.016 g Na_2SiO_3 in 15 ml of water in a 100 ml beaker. The reaction vessel was loosely covered with a Petri dish to allow CO_2 from the air to slowly diffuse into the reaction mixture. The solution was cooled down to 4 °C using an ice bath to thicken the base of the microarchitectures. After 1 hour, the solution was heated to 40 °C to split the growth front into thin stems. Optionally, after 15 minutes, these stems could then be split into trumpets by applying a two-minute CO_2 pulse. After 15 more minutes, the reaction was stopped by carefully washing the sample with deionized water. Then the microarchitectures were converted into $PbCO_3/SiO_2$.

3.4.2 Conversion of $BaCO_3$ and $SrCO_3$ Architectures to $PbCO_3$

$BaCO_3$ microarchitectures prepared by the above-described method were placed (directly after growth) in an airtight jar containing 15 g of $Pb(NO_3)_2$ in 50 ml of degassed water. This degassed water was prepared by bubbling nitrogen through it for 1 h before the conversion reaction. The reaction jar was kept under an inert atmosphere by applying a continuous flow of nitrogen while the $Pb(NO_3)_2$ was dissolving in it (ca. 15 minutes) to ensure no additional CO_2 was present in the solution. The sample slides with the microarchitectures were fully submerged for 30–60 s to allow full conversion to take place and were afterward washed with deionized water and acetone. The resulting microarchitectures were analyzed with the same methods as used for the $BaCO_3$ microarchitectures.

3.4.3 Gas Phase Conversion of $PbCO_3$ to $CH_3NH_3PbX_3$

$PbCO_3$ microarchitectures were placed in the middle of a single zone horizontal tube furnace (Figure M3.1). Subsequently, an alumina boat containing methylammonium halide (chlorine, bromine, or iodine) was placed at the edge of the tube furnace in the cold zone. The pressure inside the tube was lowered to below 0.1 mbar using a vacuum pump. The tube was then flushed with argon until atmospheric pressure was reached. This process was repeated twice to purge the system of oxygen. Afterwards the temperature of the furnace was set to 120 °C and a 30 sccm flow of argon was applied to increase the pressure to 70 mbar. The boat was moved directly next to the $PbCO_3$ microarchitectures in the middle of the oven. After 6 hours, the reaction was stopped by opening the oven. XRD, EDS and PL measurements confirmed the formation of a lead halide perovskite (see Figure 3.2b, c, and Figure 3.3a).

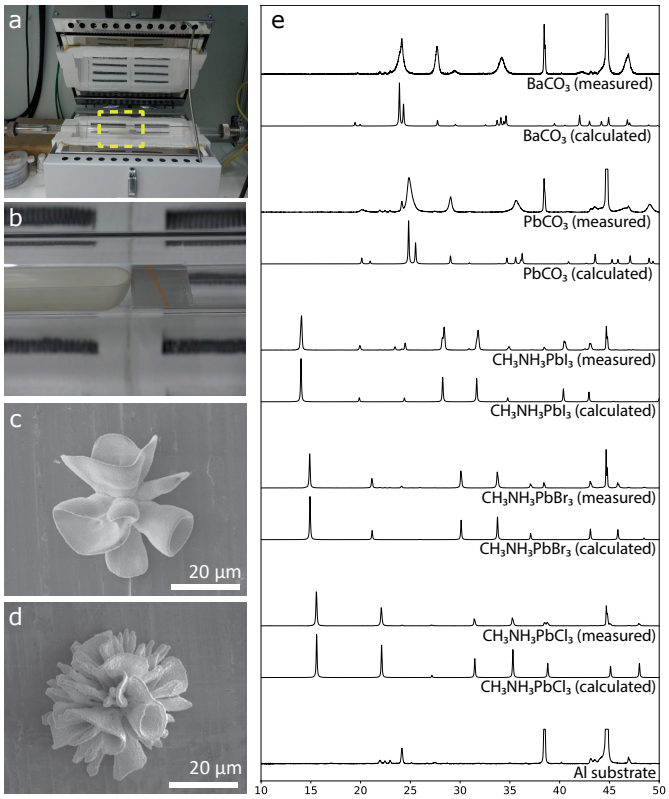

FIGURE M3.1: Experimental setup for the gas phase conversion of $PbCO_3$ to $CH_3NH_3PbBr_3$ and XRD data with reference peaks. a) Photograph of the tube furnace with the quartz tube. b) Close up of the highlighted area in a) showing the alumina boat with methylammonium bromide and an aluminum slide containing an orange line of microarchitectures after reaction to the corresponding $CH_3NH_3PbBr_3$ perovskite. c) Scanning electron microscopy image of a $CH_3NH_3PbCl_3$ microarchitecture. d) Scanning electron microscopy image of a $CH_3NH_3PbI_3$ microarchitecture. e) XRD diffractograms of the microarchitectures after conversion into the perovskite with the corresponding reference peaks.

3.4.4 Preparation and Conversion of $CaCO_3$ Biomineralized Architectures

Sand dollars shells and cuttlefish bones are biominerals composed of $CaCO_3$ crystals that can be converted to $PbCO_3$ following the procedure described for the conversion of the microarchitectures. To facilitate the conversion of the cuttlefish bone, the organic tissue was first bleached. The sand dollar shells were not bleached. For this slices of cuttlefish bone was infiltrated with acetone at lowered

pressure (250 mbar) for one hour. To remove the acetone, the cuttlefish bone were transferred to water and stored under the same reduced pressure for 1 hour. The cuttlefish bone then was bleached in 0.5M KOH for 10 days. Immersing the sample in deionized water stopped the bleaching process and the KOH was allowed to diffuse out of the sample for 24 hours. Hereafter the samples were placed in acetone for 24 hours to replace the water in the structure and dried at ambient atmosphere. Prior to the conversion to $PbCO_3$, both the cuttlefish bone and sand dollar shell were again infiltrated with acetone. For the conversion 15 g $Pb(NO_3)_2$ was dissolved in 50 ml of degassed, deionized water (0.9 M) under N_2 atmosphere. The infiltrated samples were placed in the $Pb(NO_3)_2$ solution at lowered pressure to infiltrate them completely with the aqueous solution. The exchange reaction was allowed to continue for 120 minutes. Immersing the biominerals in deionized water for 24 hours stopped the conversion reaction and removed the $Pb(NO_3)_2$. Finally, the samples were transferred to acetone for 1 hour and dried at lowered pressure for 20 minutes. The conversion to $CH_3NH_3PbX_3$ follows the same route as for the microarchitectures, but due to the large sample size, the reaction time was increased to 24 hours instead of 6 hours (Figure M3.2).

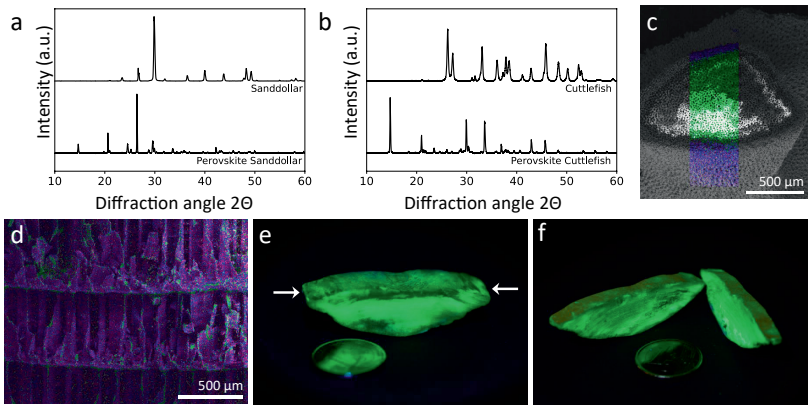

FIGURE M3.2: Conversion of biominerals in lead halide perovskites. a) X-Ray powder diffraction data showing the conversion of biomineralized $CaCO_3$ (aragonite) of a cuttlefish bone into $CH_3NH_3PbBr_3$. b) X-Ray powder diffraction data showing the conversion of biomineralized $CaCO_3$ (calcite) of a sand dollar shell into $CH_3NH_3PbBr_3$. c) EDS map of a cross-section of a sand dollar shell showing partial conversion of $CaCO_3$ into the $CH_3NH_3PbBr_3$, leading to a core-shell structure with semiconducting perovskite enveloping the insulating $CaCO_3$ (false colors refer to green: calcium, blue: lead and purple: bromine). d) EDS map of a cross-section of a cuttlefish bone showing almost complete conversion (same color code as in c). e) Slice of a cuttlefish bone (6.5×1.5×1.7 mm, 1 euro coin for scale) converted to $CH_3NH_3PbBr_3$ showing photoluminescence under UV illumination. f) Cross section of the sample shown in e) cut along the long axis indicated by arrows, showing conversion throughout the interior.

The exchange reaction to $CH_3NH_3PbX_3$ can also be performed in a liquid phase. This circumvents the size limitations given by the diameter of the reaction tube in the furnace. To convert a large piece of cuttlefish bone, 500 mg of methylammonium bromide was dissolved in 50 g of isopropanol. Similar to the previous steps, the cuttlefish bone got infused with isopropanol at lowered pressure and then transferred to the prepared solution of methylammonium bromide. To allow diffusion of methylammonium bromide into the structure, the sample was left in the solution for 24 h (Figure M3.2c).

To convert the surface of a sand dollar a solution of 25 mg methylammonium bromide in 2.5 g of isopropanol was prepared. The solution was then applied onto the sand dollar shell using a Pasteur pipet. When the conversion reaction was performed under UV radiation, the formation of the perovskite could be observed in real-time. The initially white sand dollar turns light orange in daylight and fluoresces bright green under UV irradiation.

3.4.5 X-ray Diffraction (XRD) Characterization

X-ray diffraction measurements were performed using a Bruker D2 Phaser (Bragg-Brentano geometry) using a K-alpha Cu X-ray source with an emission energy of 8.0415 keV. The samples were mounted inside a chamber filled with ambient air at room temperature. All measurements were performed using a 1.0 mm beam knife to reduce unwanted scattering and optimize the low angle part of the diffractogram. A nickel filter was used to reduce the 20–30% contribution from the k-beta Cu X-ray source. A divergence slit of 0.1 or 1 mm was used to control the illuminated area of the sample based on the spread of the material on the aluminum slide. Diffracted X-rays were detected using a Lynxeye detector and were collected for at least 12 hours with a scanning interval ($\Delta 2\Theta$) of 0.01°. Diffractograms were calibrated using the aluminum background peaks and known aluminum peaks from literature (Crystallography Open Database COD 9008460).

The crystal structure was verified by comparing the measured XRD-diffractograms with generated diffractograms from known crystal structures found in literature (Figure M3.1). Mercury was used to generate the diffractograms. The coordinates of the atoms were obtained from the following literature:
$BaCO_3$: COD 1000033 (American Mineralogist, 1971, 56, 758-766).
$PbCO_3$: COD 1010956 (Zeitschrift fuer Kristallographie, Kristallgeometrie, Kristallphysik, Kristallchemie (-144,1977), 1933, 84, 299-309).
$CH_3NH_3PbI_3$: COD 4335636 (Inorganic Chemistry, 2013, 52, 9019-9038).
$CH_3NH_3PbBr_3$: ICSD 252415 (ACS Central Science, 2016, 2, 201-209).
$CH_3NH_3PbCl_3$: https://github.com/WMD-group/hybrid-perovskites/.

3.4.6 Scanning Electron Microscopy (SEM) and Energy-Dispersive X-ray spectroscopy (EDS) Characterization

Samples were loaded into the SEM without applying a conductive metal coating. SEM images were obtained using an FEI Verios 460 equipped with an Everhart-Thornley detector (ETD) and a circular backscatter detector (CBS). The images were recorded at 5 kV, and 15 kV respectively using a 100 pA current in both instances. EDS was measured with the same electron microscope using an Oxford X-Max^n energy dispersive X-ray spectrometer with an accelerating voltage of 30 kV using a 100 pA current.

3.4.7 Optical Microscopy Characterization

Optical microscopy analysis was performed using a Leica DMRX optical microscope equipped with cross polarizers, a Basler aCA1920-40gc camera and Pylon Viewer software. Optical microscopy analysis using crossed polarizers of the $BaCO_3/SiO_2$ coral-like microarchitectures shows a Maltese cross birefringent pattern, which arises from the crystallographic alignment the c-axis of the $BaCO_3$ nanocrystals along the growth direction of the microarchitecture (Figure M3.3a). After the conversion of the $BaCO_3$ into $PbCO_3$, this Maltese cross birefringent pattern is preserved, suggesting that the nanocrystals remain aligned (Figure M3.3b).

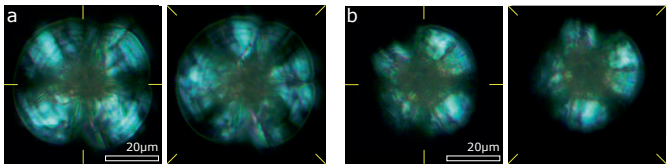

FIGURE M3.3: Crossed polarization microscopy study of $BaCO_3/SiO_2$ microarchitectures before and after conversion to $PbCO_3/SiO_2$. a) Maltese cross birefringent pattern of $BaCO_3/SiO_2$ microarchitectures. Alignment of the polarizers is depicted by the yellow lines. b) Crossed polarization microscopy image of a similar microarchitectures after conversion into $PbCO_3/SiO_2$, demonstrating the preservation of the birefringent pattern.

3.4.8 Photoluminescence and Fluorescence Microscopy Characterization

The photoluminescence measurements were performed on a WITec alpha 3000 SR. As light sources, a 532 nm laser, a 405 nm laser (Thorlabs fiber coupled-laser source S1FC-405) and a 365 nm led (LedEngin Inc LZ1-10UV00-0000) were used to excite the iodide, bromide and chloride perovskite, respectively. The signal was collected

with a WITec UHTS 300 spectrometer and the corresponding detector (DV401A-BV-352). It should be noted that the initial calcium carbonate biominerals, the $BaCO_3/SiO_2$, $SrCO_3/SiO_2$ and $CaCO_3/SiO_2$ microarchitectures and the converted $PbCO_3$ did not display any photoluminescence. The light emission of especially the bromide perovskite can be easily seen under a light microscope with the appropriate filter cube. For Figure 3.3c and Figure 3.4f text a Nikon Eclipse Ci Pol microscope with a Basler aCA1920-40gc camera, Pylon Viewer software and a Nikon FITC filter cube (Ex 465-495, DM 505, BA 515-555) was used. For Figure 3.4g a conventional photo camera (Olympus OM-D E-M1 with Olympus 12–40 pro) was used without additional filters.

3.4.9 Cathodoluminescence Characterization of Lead Halide Perovskite Microarchitectures

The cathodoluminescence (CL) spectroscopy characterization was performed using an FEI Quanta scanning electron microscope at 5 keV. The CL collection system was designed by Delmic. Two types of experiments have been performed. First standard CL spectroscopy, where simultaneously a spectrum and a secondary electron (SE) contrast are taken. It allows a perfect correlation between the spectrum and the SE image. The pixel size was around 400 nm, and each pixel was scanned during the pixel acquisition. The acquisition time was 100 ms per pixel. In figure M3.5, the average spectrum taken on individual coral-shaped microarchitectures is shown. The main peak of chloride (left, blue), bromide (middle, green) and iodide (right, red) lead halide perovskite is respectively around 420 nm, 550 nm and 800 nm, which are compatible with the PL measurements (Figure M3.4 and the main text Figure 3.4). The microarchitectures were stable enough under the beam to allow multiple acquisitions, a slight decrease of the intensity was observed, but no change in the shape of the spectrum was measured.

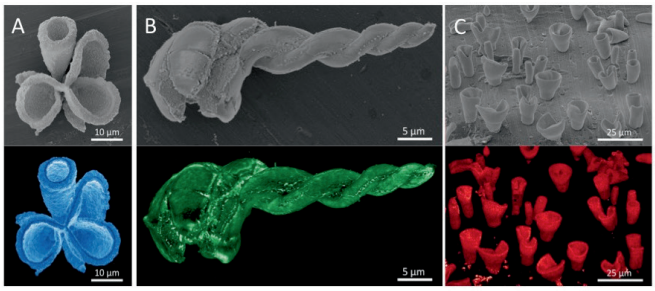

FIGURE M3.4: SEM and corresponding CL images of converted microarchitectures. a) Coral shape of $CH_3NH_3PbCl_3$. b) Helical shape of $CH_3NH_3PbBr_3$. c) Field of $CH_3NH_3PbI_3$ vase shapes. Colors in the CL images correspond to maximum peak intensity wavelength measured in CL, lighter colors correspond to higher emission.

The CL signal can also be collected using a photomultiplier tube (PMT), in this case, without any spectral selectivity. The time per pixel is therefore drastically reduced to 100 µs per pixel and large area can be scanned with a good spatial resolution. In the case of Figure 3.4a–e, the pixel size is between 20 nm and 100 nm. These images are intensity maps, they have been color-coded to represent the range of the emitted light deduced from spectra of Figure M3.5: blue for $CH_3NH_3PbCl_3$, green for $CH_3NH_3PbBr_3$, and red for $CH_3NH_3PbI_3$ microarchitectures.

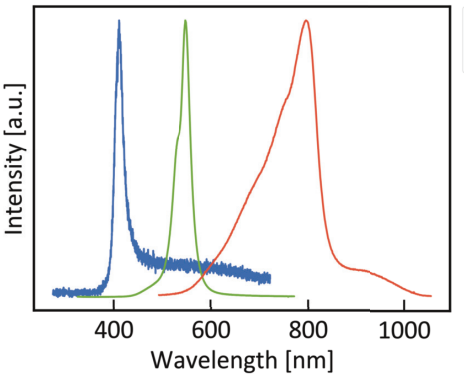

FIGURE M3.5: Cathodeluminescence of lead halide perovskite microarchitectures. Spectrum of $CH_3NH_3PbCl_3$ (left), of $CH_3NH_3PbBr_3$ (middle) and $CH_3NH_3PbI_3$ (right).

3.4.10 Photoluminescence Lifetime Characterization

The photoluminescence lifetime measurements were performed using a time-correlated single-photon counting (TCSPC) method. The setup is equipped with a picosecond pulse driver (PicoQuant PDL 828), a 485 nm excitation laser source with pulse widths below 110 ps and 40 MHz repetition rate (PicoQuant LDH-D-C-485), a picosecond time analyzer (PicoQuant HydraHarp 400), and a single photon counting detector (Micro Photon Devices, MPD-5CTD). A series of neutral density filters was used to attenuate the intensity of the laser source. The measurements were acquired at 0.5 $\mu J/cm^2$/pulse. A long-pass filter (ET500LP, Chroma Tech.) was used to transmit the entire radiative emission from the perovskite microarchitectures to the detector while excluding any contribution from the excitation source. The detected emission signal was then fed into the single-photon counter to ensure no more than one photon per excitation cycle registration. To prevent any event that may increase the chance of registering more than one photon per cycle, we performed the measurements with a rate below 1% of the repetition rate of the laser. The samples were soaked under the same laser (CW mode) for about 2 minutes before the measurements to minimize any effect of light-induced

dynamics within perovskite microarchitectures. In fact, over the measurement, we observed no degradation within the $CH_3NH_3PbBr_3$ 3D microarchitectures. The measurement was performed at room temperature. We used a bi-exponential function to fit the PL decay curve. The fitting equation for Figure 3.3b follows a bi-molecular recombination dynamics: $dn(t)/dt = -k_1(n) - k_2(n)^2$ where k_1 is 0.841 and k_2 is 2.604, which yields an effective photoluminescence lifetime of 28 $\pm$ 0.65 ns. We associated the resulting lifetime with an admixture of exciton and quasi-neutral free charges presence in the perovskite microarchitectures.

3.5 Appendix

3.5.1 Conversion of $SrCO_3/SiO_2$ Architectures to $CaCO_3/SiO_2$

Water was degassed by bubbling nitrogen through it for 1 hour. Inside an airtight jar with a magnetic stirring bar, 5 g of $CaCl_2$ was dissolved in 50 ml of the degassed water. The reaction jar was kept under an inert atmosphere by applying a continuous flow of nitrogen via two tubes that were inserted through the cap of the airtight jar. Sample slides containing $SrCO_3/SiO_2$ microarchitectures, prepared as described above, were placed in the calcium solution. After keeping the solution under nitrogen atmosphere for 30 minutes, the samples were removed from the solution and washed with deionized water and acetone subsequently. The resulting microarchitectures were characterized using SEM and EDS (Figure A3.1).

3.5.2 Conversion of $CaCO_3/SiO_2$ Architectures to $PbCO_3/SiO_2$

Water was degassed by bubbling nitrogen through it for 1 hour. Inside an airtight jar with a magnetic stirring bar, 550 mg of $Pb(NO_3)_2$ was dissolved in 50 ml of the degassed water. The reaction jar was kept under an inert atmosphere by applying a continuous flow of nitrogen via two tubes that were inserted through the cap of the airtight jar. After the $Pb(NO_3)_2$ was completely dissolved, sample slides containing $CaCO_3$ were inserted in the solution. The lid was closed again and the solution containing the slides was kept under nitrogen atmosphere for 10 minutes. Afterward, the sample slides were removed and washed with deionized water and acetone subsequently.

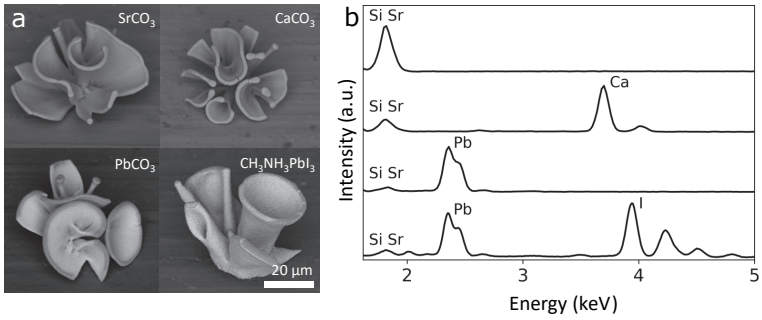

FIGURE A3.1: Conversion of $SrCO_3/SiO_2$ microarchitectures in $CH_3NH_3PbI_3$ perovskites via $CaCO_3/SiO_2$. a) Scanning electron micrographs from the sequential reaction products and the final perovskite for the conversion of $SrCO_3$ to $CaCO_3$ to $PbCO_3$ and $CH_3NH_3PbI_3$. b) Energy dispersion spectroscopy of the microarchitectures in a) showing the conversion of $SrCO_3$ (top) into $PbCO_3$ via $CaCO_3$ and the final product $CH_3NH_3PbI_3$ (bottom).

The resulting microarchitectures were characterized with SEM, and EDS (Figure A3.1). Conversion of these $PbCO_3/SiO_2$ microarchitectures into the desired perovskite occurred under the experimental conditions described in section 3.4.3.

3.5.3 Detection of Methylamine

Our method for the detection of methylamine during the conversion of $PbCO_3$ to $CH_3NH_3PbX_3$ involves a condensation reaction of methylamine with 2-napthalaldehyde to form the corresponding imine (N-Methyl-1-(2-naphthyl)methanimine) (Figure A3.2).

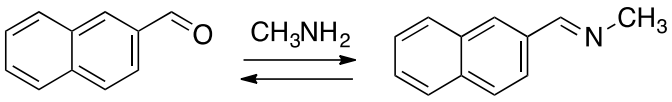

FIGURE A3.2: Condensation of methylamine with 2-naphthaldehyde.

Both 2-napthalaldehyde and the resulting imine structures can be detected straightforwardly due to their high UV-light absorption that arises from the aromatic ring systems. Furthermore, application of high performance liquid chromatography (HPLC) with UV-light detection allows us to distinguish between 2-napthalaldehyde and its N-methylimine.

3.5.4 HPLC Analysis

HPLC analysis was performed using an Agilent Technologies Infinity 1260 HPLC system equipped with a Chiralpak IA (250 x 4.6 mm, 5 µm) column, eluent: n-heptane/isopropanol 80/20 (v/v), flow rate: 0.7 ml/min., detection: 220 nm). Retention times of 2-napthalaldehyde and the corresponding N-methylimine were determined following the procedure below:

1) 2-napthalaldehyde: 2-napthalaldehyde (droplet) was dissolved in isopropanol (1.0 ml). HPLC analysis of the resulting solution indicated that the retention time of the aldehyde is 7.1 min. (see Figure A3.3a) (top) chromatogram).

2) N-methylimine. $MeNH_2$ (50 ml of 33 wt.% solution in MeOH) was added to a solution of 2-napthalaldehyde (2 mg) in isopropanol (1.0 ml). The resulting mixture was shaken for 30 seconds and allowed to react for 15 minutes at ambient temperature without stirring. HPLC analysis of the resulting solution indicated complete conversion of 2-napthalaldehyde into the corresponding imine (retention time 6.4 min., see Figure A3.3b) (bottom) chromatogram).

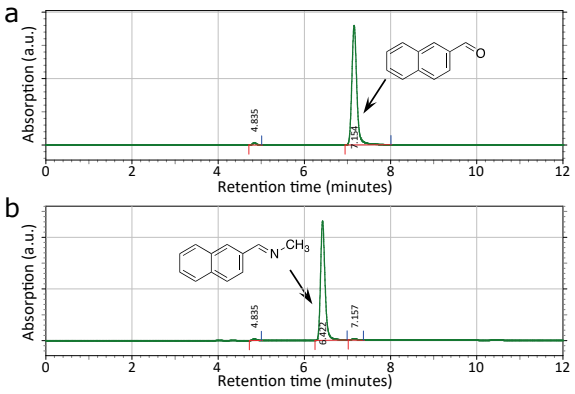

FIGURE A3.3: Chromatograms of a) 2-napthalaldehyde, and b) the resulting imine.

3.5.5 Detection of Methylamine During the Conversion Reaction:

The reaction was performed following the standard protocol in the presence of 2-napthalaldehyde. A stock solution of o CH_3NH_3Br (10 mg) and 2-napthalaldehyde (5 mg) in isopropanol (10 ml) was prepared. As expected, HPLC analysis of the stock solution confirmed that virtually only 2-napthylaldehyde was present in the mixture, thus indicating no formation of methylamine (Figure A3.4b). Then, solid $PbCO_3$ (3 mg) was added to the stock solution (0.3 ml), resulting in the release of methylamine and its subsequent reaction with the present 2-napthalaldehyde to form the corresponding imine as indicated by HPLC (Figure A3.4a).

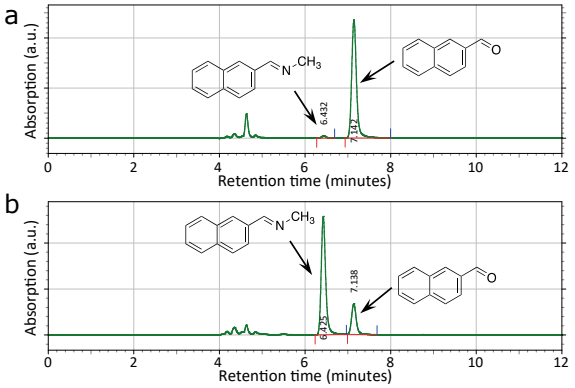

FIGURE A3.4: Chromatograms of the stock solution of a) 2-napthalaldehyde and methylammonium bromide, and b) the reaction mixture upon addition of $PbCO_3$, showing the presence of the imine, which indicates the formation of methylamine during the reaction of $PbCO_3$ to methylammonium lead bromide.

3.5.6 Conversion of $PbCO_3/SiO_2$ Architectures to PbI_2/SiO_2

An acidic aqueous solution was prepared by adding 17 µl of HNO_3 (70% in H_2O) to 50 mL of deionized water. 150 mg KI was added to 10 mL of this acidic aqueous solution. This solution was then used to convert microarchitectures from $PbCO_3$ to PbI_2 by dipping the sample in for 45 seconds under ambient conditions. For each consecutive conversion, a new solution was made per individual sample. Afterward, the sample slides were washed with deionized water and acetone and carefully dried in the air. The resulting microarchitectures were characterized using SEM and EDS (Figure A3.5).

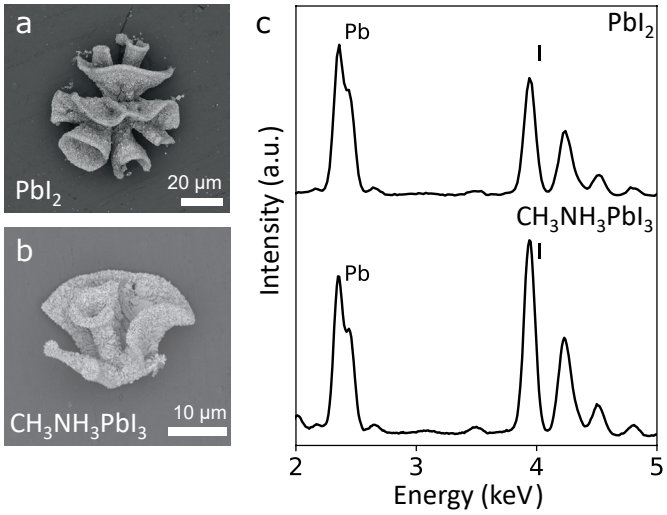

FIGURE A3.5: Conversion of $PbCO_3$ to PbI_2, followed by the conversion to $CH_3NH_3PbI_3$. Scanning electron micrographs of a) PbI_2, and b) $CH_3NH_3PbI_3$. c) Energy dispersion spectroscopy graphs showing the successful conversion to the intermediate PbI_2, and the final product $CH_3NH_3PbI_3$.

Radiant
Ion Exchange Lithography on Lead Carbonate, 2020
Lukas Helmbrecht

CHAPTER 4

Ion Exchange Lithography: Localized Ion Exchange Reactions for Spatial Patterning of Perovskite Semiconductors and Insulators

Submitted as:

Helmbrecht, L., Futscher, M.H., Muscarella, L.A., Ehrler, B. and Noorduin, W.L. *Ion Exchange Lithography: Localized Ion Exchange Reactions for Spatial Patterning of Perovskite Semiconductors and Insulators*, 2020.

Patterning materials with different properties in a single film is a fundamental challenge and essential for the development of next-generation (opto)electronic functional components. This work introduces the concept of ion exchange lithography and demonstrates spatially controlled patterning of electrically insulating films and semiconductors with tunable optoelectronic properties. In ion exchange lithography, a reactive nanoparticle "canvas" is locally converted by printing ion exchange "inks". To demonstrate the proof of principle, a canvas of insulating nanoporous lead carbonate is spatioselectively converted into semiconducting lead halide perovskites by contact printing an ion exchange precursor ink of methylammonium and formamidinium halides. By selecting the composition of the ink, the photoluminescence wavelength of the perovskite semiconductors is tunable over the entire visible spectrum. A broad palette of conversion inks can be applied on the reactive film by printing with customizable stamp designs, spray-painting with stencils, and painting with a brush to inscribe well-defined patterns with tunable optoelectronic properties in the same canvas. Moreover, the optoelectronic properties of the converted canvas are exploited to fabricate a green light-emitting diode (LED), demonstrating the functionality potential of ion exchange lithography.

4.1 Introduction

Spatial arrangement of materials with contrasting properties is fundamentally interesting and essential for integrated (opto)electronic devices.[3,77] Nanoparticles are versatile building blocks for achieving such arrangement by both bottom-up and top-down assembly.[8,9,11,14,33,34,38,39,48,77–87,163] Spatial patterning of nanoparticles has been achieved by methods such as patchy particles, oriented attachment, hierarchical self-assembly, topological templates, and optical and e-beam lithography.[8,9,11,14,33,34,38,39,77–82,163,164] Moreover, the entire ensemble of nanoparticles can be converted into a desirable chemical composition using ion exchange reactions, while preserving the pattern of the ensemble.[34,48,83–87] Also, selected areas of the ensemble can first be encapsulated with a passivating coating, after which only the uncoated nanoparticles undergo conversion during ion exchange.[95] Hence, organization of different composition is possible in many ways, but oftentimes requires multiple steps to achieve control over patterning and chemical composition, making the overall process difficult and expensive.[77,82]

Locally applying the reagents offers an alternative approach for spatial arrangement of materials with desirable properties. For thousands of years, printing of inks on canvases has spurred human development. Recently, methods such as microcontact printing have been used extensively to locally functionalize substrates and infuse reactants in gels.[165–168] Inspired by these works, we here introduce the concept of ion exchange lithography (IEL). We show that spatial patterning of materials can simply be achieved by printing ion exchange "inks" on a reactive nanoparticle "canvas". Importantly, to act as a versatile canvas, the nanoparticle film should enable ion exchange to many different chemical compositions. The ink, on the other hand, should react the contacted area of the canvas to one specific composition only, while other reaction products ideally leave the canvas automatically.

To demonstrate the proof-of-principle of IEL, we explore the spatially controlled conversion of an electrically insulating canvas into semiconducting lead halide perovskites. The extraordinary properties of perovskites, in combination with their simple synthesis, is revolutionizing the field of optoelectronics.[102–104] Spatially organizing perovskites alongside materials with fundamentally different properties is essential for integrated devices such as displays, detectors, and scintillators.[107–112] Spatial positioning of perovskites has been achieved using, for instance, photolithography, laser writing, templates, and inkjet printing.[114–119,121] Post synthesis modification of perovskites has enabled local modification of the light emission color.[96,113] Nevertheless, such approaches are often laborious and slow, and require specialized equipment, thus making them difficult to scale up. This highlights the need for new strategies to directly achieve spatial organization of desirable compositions in a simple and scalable manner.

Here we integrate semiconducting perovskites in an electrically insulating film by printing, painting, and spraying reactive inks on an ion-exchange reactive canvas. The versatility of this IEL approach allows for scalability and arbitrary, user-defined patterns. The photoluminescence wavelength of the perovskite semiconductors is tunable over the entire visible spectrum by selecting the composition of the ink. Moreover, we show that the IEL approach can be integrated into the fabrication of (opto)electronic devices such as light-emitting diodes (LED).

4.2 Results and Discussion

Our approach is illustrated in Figure 4.1. In short, nanoscopic lead carbonate ($PbCO_3$) crystals are deposited in a thin film. This electronically insulating lead carbonate ($PbCO_3$) film acts as reactive canvas, while a solution of methylammonium halides (CH_3NH_3X or MAX; X = Cl, Br, or I) is the reactive ink. Contact printing of the ink on the canvas results in the local conversion of $PbCO_3$ into semiconducting methylammonium lead halide perovskites ($CH_3NH_3PbX_3$ or $MAPbX_3$; X = Cl, Br, or I) following the previously developed reaction:[48]

$$PbCO_3(s) + 3CH_3NH_3X(l) \rightleftharpoons H_2O(l) + CO_2(g) + 2CH_3NH_2(g) + CH_3NH_3PbX_3(s) \tag{4.1}$$

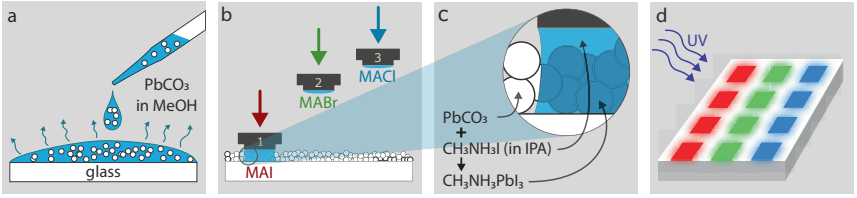

FIGURE 4.1: Schematic illustration showing the fabrication of a spatially patterned perovskite film. a) Drop casting $PbCO_3$ particles dispersed in methanol onto a glass substrate results in a $PbCO_3$ thin film that acts as the reactive canvas. b) Stamping MAX in IPA on the canvas results in, c) spatially-controlled conversion of the $PbCO_3$ into a $MAPbX_3$ perovskite. d) Upon UV irradiation, the converted areas emit light with a color that is controlled by adjusting the halide moiety of the perovskite.

To demonstrate the proof-of-principle, we fabricate nanoporous films by drop casting nanoscopic $PbCO_3$ crystals onto glass substrates (see Methods for details). High-resolution Scanning Electron Microscopy (SEM) shows that the particles have typical sizes between 40 and 300 nm, and are densely packed into uniform films while still exhibiting nanoscale porosity (Figure 4.2a). We find that the film

thickness can be tuned between ca. 0.25 and 5.0 µm by controlling the drop casting conditions (Figure 4.2 and Methods).

We perform the ion exchange contact printing by bringing the $PbCO_3$ film in contact with a solution of MAX in anhydrous isopropyl alcohol (IPA). The conversion ink is applied using customized silicone stamps (see Methods). Silicone is easily moldable and chemically inert. In addition, the hardness of the silicone can be tuned to achieve uniform contact while keeping the canvas intact during removal of the stamp (see Methods).[165,168] The local conversion is demonstrated by applying MABr-IPA on the $PbCO_3$ canvas using a stamp patterned with rectangular studs. Within seconds the white $PbCO_3$ transforms into yellow-orange perovskite at the points of contact with the stamp, thereby meticulously replicating the pattern of the stamp with high fidelity (See Methods for comparison of a stamp and stamped pattern). The optoelectronic properties of the converted pattern can directly be visualized by exciting the electronic structure with an ultra-violet (UV) light source (Figure 4.2b). We observe bright green photoluminescence (PL) from the converted rectangles, whereas the lead carbonate in the pristine part of the film did not convert to the perovskite and therefore did not emit any light. Photoluminescence spectroscopy showed that the emission wavelength of the converted pattern peaked at 530 nm, which is consistent with previous PL measurements of $MAPbBr_3$.[48]

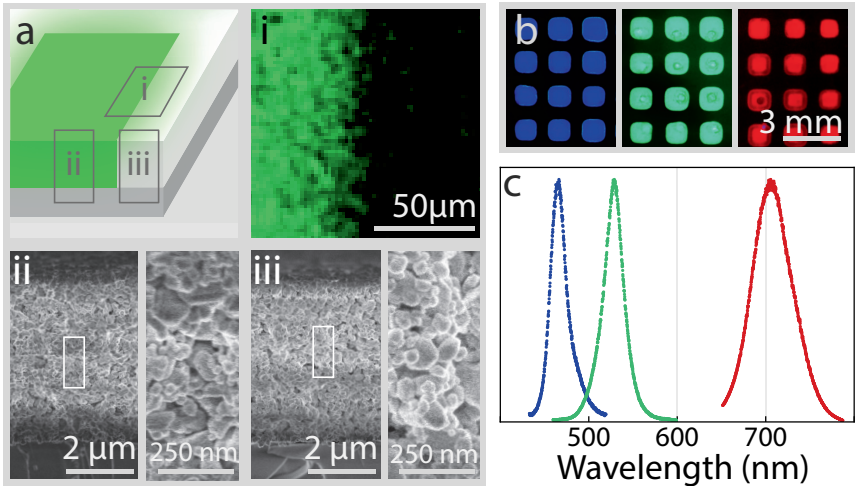

FIGURE 4.2: Characterization of contact printed perovskite pixels. a) Schematic overview of a printed pixel: i) EDS elemental mapping of Br atoms, ii) cross-section of a converted film with close-up (SEM), iii) cross section of a pristine film with close-up (SEM). b) Fluorescence photographs of contact printed perovskite pixels of different emission colors by tuning the halide moiety: left to right: MACl-MABr (6:4), MABr, MABr-MAI (2:8). c) Corresponding normalized photoluminescence spectra of the perovskites shown in b).

We expect that the nanoporous structure facilitates percolating by capillary forces to achieve conversion throughout the interior of the canvas. Indeed, energy-dispersive X-ray spectroscopy (EDS) on a cross-sectioned sample reveals the presence of bromide throughout the depth of the canvas (see Methods, Figure M4.3). Combined with fluorescence photographs of the backside of the opaque canvas, this indicates conversion from the top to the bottom (see Methods, Figure M4.2). Still, in the lateral direction, a well-defined boundary between the converted and unconverted area is achieved, according to EDS (Figure 4.2a). Although the grains undergo conversion to perovskite, the nanoscopic morphology is conserved, as observed via high-resolution electron microscopy (Figure 4.2a). Furthermore, EDS analysis suggests that mostly the outside of these grains is converted, as ca 3.5 at% of the film constitutes of bromide, while the surplus $PbCO_3$ in the grains may support the morphology retention. We expect that the degree of conversion can be further controlled through the balance between $PbCO_3$ and conversion ink, as well as the size of the particles themselves.

Reaction scheme 4.2 suggests that perovskites with different halide moieties–and therefore different emission colors–can be synthesized in the $PbCO_3$ film by selecting the corresponding methylammonium halide precursor in the ink. Indeed, mixing MAI into the MABr/IPA conversion ink yielded mixed-halide perovskite patterns with red PL, while MACl addition resulted in blue PL (Figure 4.2b). The emission wavelength can be tuned by the mixing ratios of different methylammonium halides in the conversion ink: e.g., 6:4 molar ratio MACl:MABr/IPA resulting in bright emission around 465 nm (Figure 4.2c), whereas 8:2 molar ratio MAI:MABr yields deep red emission around 705 nm (Figure 4.2c). Hence, the color of the light-emitting patterns can be tuned over the whole visible spectrum.

IEL can be extended to other classes of perovskites. Formamidinium halide perovskites ($CH(NH_2)_2PbX_3$ or $FAPbX_3$; X = Cl, Br, or I) are of interest because of their greater chemical stability and longer carrier diffusion length while exhibiting comparable optical performance compared to methylammonium perovskites.[169,170] Conversion of $PbCO_3$ to $FAPbX_3$ is achieved using formamidinium halides ($CH(NH_2)_2X$ or FAX; X = Cl, Br, or I) instead of methylammonium halides in the precursor ink. Akin to MAX (reaction scheme 4.2), FAX can partly dissociate to form acid and thereby drive the exchange of carbonate with the halide group. Moreover, the chemical similarities between MAX and FAX as well as the structural similarities between the crystal lattices of $MAPbX_3$ and $FAPbX_3$ suggest an equivalent reaction pathway. The resulting $FAPbX_3$ perovskite patterns show bright luminescence with tunable PL emission throughout the visible spectrum by selecting the halide moiety between chloride, bromide, and iodine (see Appendix).

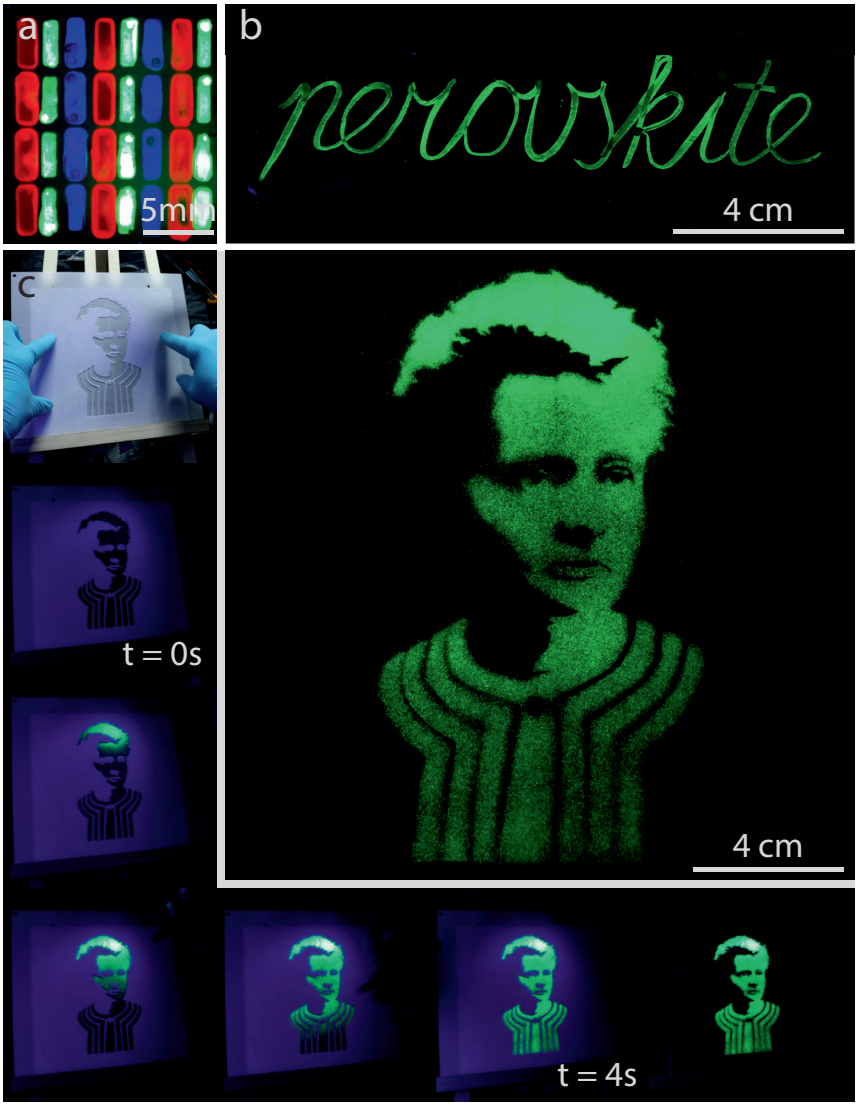

FIGURE 4.3: IEL via different printing techniques. a) Fluorescence photograph of multicolor contact printed pixels: FABr-FAI (2:8) (red), MABr (green), and MACl-MABr (6:4) (blue) separated by unconverted $PbCO_3$. b) Fluorescence photograph of a pattern drawn by applying the conversion ink with a paintbrush. c) Time-lapse of an airbrush painting of Marie Skłodowska-Curie: a 20x20 cm film of $PbCO_3$ is selectively shielded with a stencil (the polymer in the stencil fluoresces blue under UV irradiation), MABr/IPA is applied with an airbrush gun, the ion exchange reaction creates perovskite that luminesces green under UV irradiation, removal of the stencil shows the portrait.

Based on these insights, we integrate perovskites with different emission wavelengths into a single canvas. To this aim, we sequentially print the ion mixtures for different perovskites on the lead carbonate film. Accurate spatial positioning of the different stamps is achieved by a guiding framework (see Methods, Figure M4.2). To demonstrate the principle, we integrate rectangles of red, green, and blue-emitting semiconductors within the non-luminescent insulator to produce an array pattern akin to the ones commonly used in LED displays (Figure 4.3a).

The ion exchange inks could be applied using many other traditional and scalable inking techniques such as inkjet-, offset-, and roll-to-roll printing. From this extensive repertoire, we test traditional artist's paintbrushes and an airbrush gun. With the paintbrush, freeform patterns can be achieved straightforwardly (Figure 4.3b). With the airbrush, large uniform areas can be converted. Moreover, highly complex patterns can be achieved using laser-cut stencils as a shadow mask, which we exploit for creating a green luminescent portrait of Marie Skłodowska-Curie. (Figure 4.3c). An additional advantage of airbrushing is that this method is fast and contact-free while easily converting sizeable areas, hence averting the risk of damaging the film and offering compatibility for large-scale fabrication.

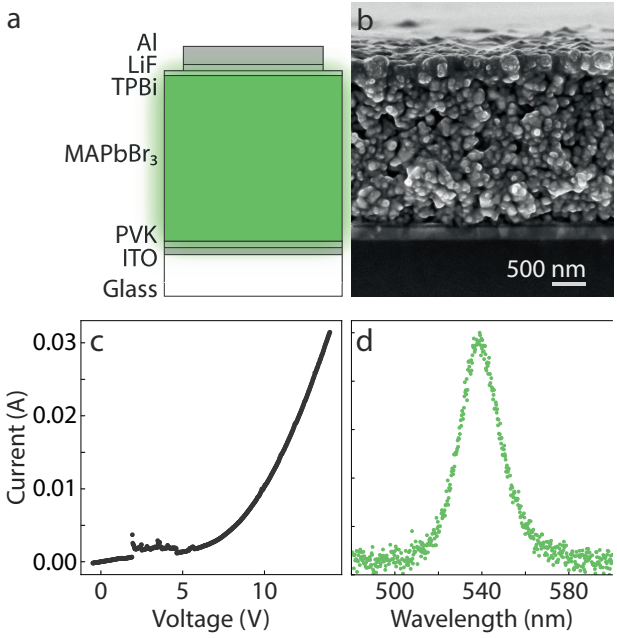

FIGURE 4.4: LED based on an IEL. a) Schematic of the layers used in this LED. b) Cross section of a device imaged by SEM. c) IV measurement. d) Normalized EL showing green light emission of the LED at 10 V.

IEL offers exciting opportunities for the direct integration of materials with different electronic properties in functional devices. We demonstrate the principle for a LED with $FAPbBr_3$ as the active layer. The device is constructed of stacked layers with, in the center, the perovskite created by ion exchange (see Figure 4.4a, b and Methods 4.4.4). We characterize the device by performing electroluminescence (EL) spectroscopy and measuring the current-voltage (IV) curves. As expected for $FAPbBr_3$ LEDs, the IV curves display typical diode characteristics (Figure 4.4c). With applied voltage, the device operates as an LED and emits green EL around 540 nm as previously reported,[171,172] demonstrating the potential of IEL for functional (opto)electronic devices (Figure 4.4d).

4.3 Conclusion

In conclusion, we here demonstrate spatially-controlled ion exchange reactions of lead carbonate films into lead halide perovskites. We show that this ion exchange-lithography method offers a simple, scalable, versatile, and highly customizable method for integrating desirable complementary electronic and optoelectronic properties in arbitrary patterns that can be integrated into functional devices. Effectively, the conversion liquid and film can be regarded as reactive ink and canvas for integrating unusual and attractive properties with high spatial control.

Semiconductors and lead carbonates have a long history in painting and other arts. Basic lead carbonate is one of the oldest synthetic pigments known, while semiconducting salts such cadmium sulfide and lead chromate enabled bright colors and were widely adopted by painters such as Monet and Van Gogh.[173–176] Traditionally, artists apply the semiconductors as pigment on the canvas. In contrast, our work enables conversion of the canvas into a semiconductor by painting a reactive ink.

Already, many ion exchange reactions have been developed in liquids.[48,83–86] We therefore envisage that the palette of conversion inks for our IEL methodology can straightforwardly be extended to a wide range of chemical compositions with desirable and unusual properties. Moreover, state-of-the-art technologies such as roll-to-roll and inkjet printing can be exploited, since the resolution of the converted patterns is to a large extend defined by the precision with which the conversion ink is applied. In addition, we foresee that nanocomposites could serve as attractive conversion canvases due to their outstanding mechanical properties and chemical reactivity.[48,177–179] Consequently, IEL may offer an attractive route for the synthesis of functional integrated devices such as displays and detectors that require complicated spatial patterning of complementary properties in a single film. Therefore, exciting opportunities will arise from expanding the microelectronic paint box, adding conversion inks for the synthesis of other semiconductors, transport layers, and conductors, which ultimately enables fully printed devices with ion exchange lithography.

4.4 Methods

4.4.1 Lead Carbonate Canvas Fabrication

Lead carbonate powder (2.0 g, Alfa Aesar, lead(II)carbonate, ACS, 40119) was dispersed in 10 ml isopropyl alcohol with glass beads in a 20 ml vial, and ground for ten consecutive days in an ultrasonic bath (VWR Ultrasonic Cleaner USC-THD). Subsequently, the nanocrystalline lead carbonate powder was isolated from the slurry by filtration. To prepare the canvas, the nanocrystals were dispersed in methanol (25 mg $PbCO_3$/ml MeOH) and sonicated for 180 minutes at room temperature. Microscope slides were cut to 15x15 or 17x17 mm squares, cleaned with isopropyl alcohol, and plasma cleaned for 10 minutes. Typically, 150–200 µl of the $PbCO_3$/MEOH was drop casted onto each substrate. To obtain the canvas, the solvent was left to evaporate at 45 °C in an oven. Thinner films were achieved by diluting the dispersion (Figure M4.1). The lead carbonate canvas used for the airbrushed portrait and the "perovskite" lettering was obtained by covering a 20x20 cm ceramic tile with double-sided tape and brushing lead carbonate onto it (see also M4.2g).

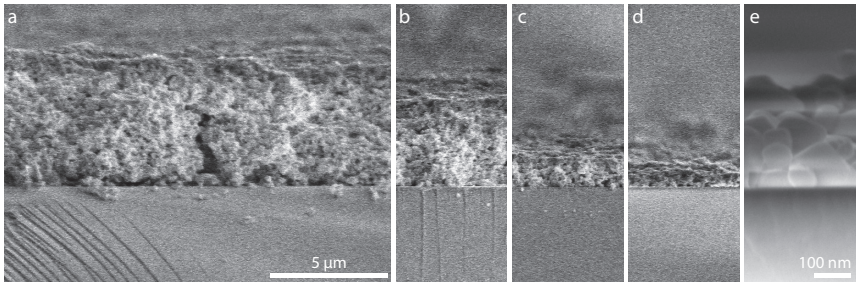

FIGURE M4.1: Lead carbonate nanoparticle films of decreasing thickness. a) 5 µm film created with stock solution. b–e) Dilution of the dispersion allows for thinner films. Note the higher magnification in e).

4.4.2 Contact Printing Perovskites

Stamps were prepared from commercially available silicone (Zhermack elite double, 32 shore). The silicone is available in a variety of degrees of hardness. We find that softer stamps damage the film, whereas harder stamps fail to make uniform contact. The stamps were fabricated by casting the liquid silicone into 3D printed molds. We designed patterns with 1x1 mm studs and 1 mm spacing, as well as a pattern of 1.5x3 mm studs. The later pattern was split into three parts on three stamps for sequential application (Figure M4.2). The conversion ink was prepared by dissolving 0.16 mmol methylammonium or formamidinium halide per ml

isopropyl alcohol under inert environment. The crucial parameters for successful stamping are the amount of ink that is transferred and the applied pressure. To control the amount of liquid, 25 µl conversion ink is placed in a petri dish. A 20x20 mm piece of foam board is pressed onto that drop. The stamp is inked by gently pressing it against the foam board. To contact print the $PbCO_3$, the stamp is gently pressed on the canvas, assuring sufficient contact pressure to transfer the ink without damaging the canvas.

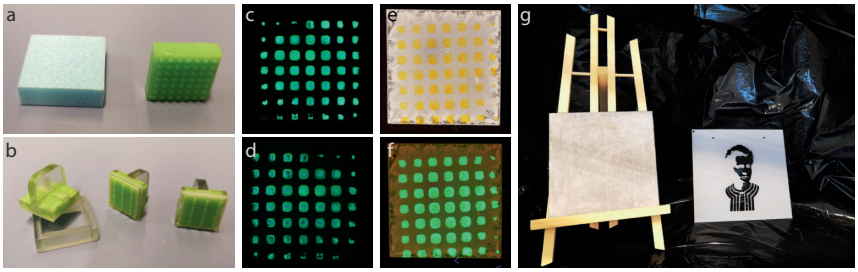

FIGURE M4.2: Printing and painting of perovskites. a) Foam board for ink transfer and silicone stamp. b) Silicone stamps with guiding frame to integrate different compositions, c) and d) perovskite pattern on glass, imaged from the front and backside, respectively, showing conversion throughout the film. f, g) Perovskite pattern in daylight and with additional UV light, respectively. c) Setup for airbrush painting with a stencil.

4.4.3 Characterization of Perovskite Samples

The fluorescent nature of the perovskites is a convenient first indicator of successful conversions. Illuminated with a UV LED (365 nm), the converted parts light up. The photographs in Figures 4.2 and 4.3 were taken with a Canon 800D camera equipped with a Sigma 17-70 mm macro lens and a UV filter. Scanning electron microscopy micrographs were captured with an FEI Verios 460. The EDS (energy dispersive X-Ray spectroscopy) map of bromide distribution was recorded with an additional Oxford X-Max^n energy dispersive X-ray spectrometer (Figure 4.2 and M4.3). Photoluminescence was studied using a Witec alpha 300 in combination with a Thorlabs S1FC405 405 nm laser.

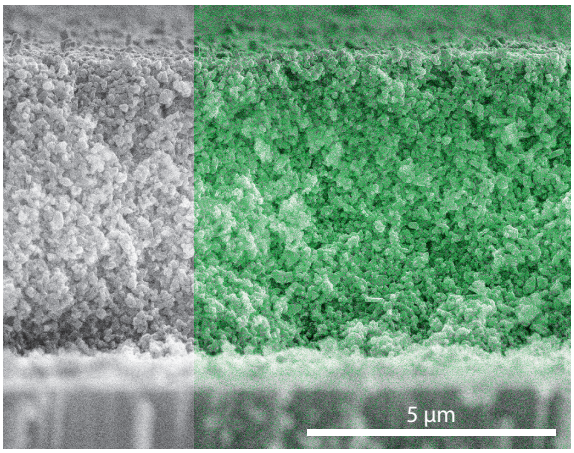

FIGURE M4.3: EDS map of a cross-sectioned, converted canvas. Left: SEM image showing the nanoparticles in the film. Right: elemental map overlay showing the presence of bromide (green) throughout the film, indicating conversion from top to bottom.

4.4.4 LED Fabrication

The stack used to fabricate the LED is ITO/PVK/perovskite/TPBi/LiF/Al. First, glass-ITO substrates were cleaned with sonication subsequently for 15 minutes in detergent in deionized water, acetone, and isopropanol, followed by oxygen plasma for 15 minutes at 100 W. The hole injection layer is prepared by dissolving 9 mg of Poly(9-vinylcarbazole) powder in 1 ml of chlorobenzene, stirred overnight and then spun at 2000 rpm for 60 seconds with a ramp of 1000 rpm/s on the cleaned ITO substrates. The films were then annealed at 120 °C for 20 minutes. Second, the $PbCO_3$ canvas was created and converted to perovskite: after 1 second of plasma cleaning of the PVK surface, 150 µl of $PbCO_3$ dispersion (prepared as above, settled for 24 h) were drop cast onto the PVK film at 50 °C. The lead carbonate films were converted to perovskite by immersing them into a conversion ink for 30 seconds (0.16 mmol/ml FABr in anhydrous IPA) and drying them under N_2 flow. Finally, the films were taken into an evaporation chamber where 40 nm TPBi (0.1 Å/s), 1.2 nm LiF (0.1 Å/s), and 100 nm aluminum (1 Å/s) were sequentially deposited at a pressure of 10-7 mbar to serve as electron injection layer and cathode. Prior IV and EL characterizations, the devices were encapsulated using epoxy glue and glass coverslips.

4.4.5 LED Characterization

The top contact, as well as the ITO film, was segmented into six sections, which could be individually addressed. A custom software took care of recording the current density versus voltage behavior via a Keithley 2440. For the EL measurement, a continuous voltage of 10 V was applied while simultaneously capturing the emitted light with a fiber-coupled spectrometer (Ocean Optics). To enhance the light collection, a 30 mm lens was mounted above the device to collect the emission and focus it into the fiber towards the spectrometer.

4.5 Appendix

4.5.1 Photoluminescence of Formamidinium Lead Halide Perovskites

Formamidinium lead halide perovskites can be created via ion exchange of $PbCO_3$ with formamidinium halide inks. Figure A4.1 shows typical PL spectra of blue-, green-, and red-emitting perovskites.

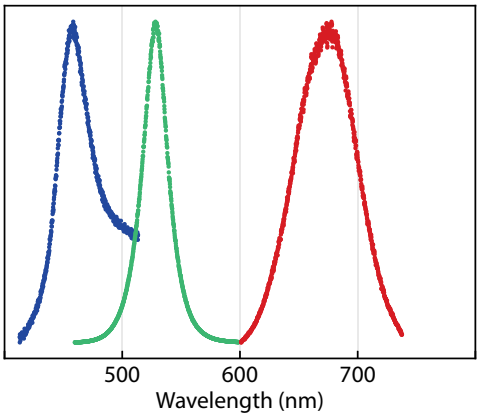

FIGURE A4.1: Normalized photoluminescence spectra of formamidinium lead halide perovskites created by ion exchange reaction of $PbCO_3$ with: blue: FACl-FABr (6:4); green: FABr, red: FABr-FAI (2:8).

Bibliography

1. Curie, E. *Madame Curie: A Biography* (William Heinemann, London, 1937).
2. Whitesides, G. M. & Grzybowski, B. Self-assembly at all scales. *Science* **295,** 2418–2421 (2002).
3. Faustini, M., Nicole, L., Ruiz-Hitzky, E. & Sanchez, C. History of Organic-Inorganic Hybrid Materials: Prehistory, Art, Science, and Advanced Applications. *Advanced Functional Materials* **28,** 1704158 (2018).
4. Jackson, A. P., Vincent, J. F. V. & Turner, R. M. The mechanical design of nacre. *Proceedings of the Royal Society of London. Series B. Biological Sciences* **234,** 415–440 (1988).
5. Van Olphen, H. Maya Blue: A Clay-Organic Pigment? *Science* **154,** 645–646 (1966).
6. Harari, Y. N. *Sapiens: A Brief History of Humankind* (Random House, 2014).
7. Cölfen, H. & Mann, S. Higher-order organization by mesoscale self-assembly and transformation of hybrid nanostructures. *Angewandte Chemie - International Edition* **42,** 2350–2365 (2003).
8. Phillips, K. R. *et al.* A colloidoscope of colloid-based porous materials and their uses. *Chemical Society Reviews* **45,** 281–322 (2016).
9. Sacanna, S. *et al.* Shaping colloids for self-assembly. *Nature Communications* **4,** 1688 (2013).
10. Vantomme, G. & Meijer, E. W. The construction of supramolecular systems. *Science* **363,** 1396–1397 (2019).
11. Vogel, N., Retsch, M., Fustin, C.-A., del Campo, A. & Jonas, U. Advances in Colloidal Assembly: The Design of Structure and Hierarchy in Two and Three Dimensions. *Chemical Reviews* **115,** 6265–6311 (2015).
12. Marshall, S. M., Murray, A. R. & Cronin, L. A probabilistic framework for identifying biosignatures using Pathway Complexity. *Philosophical Transactions of the Royal Society A: Mathematical, Physical and Engineering Sciences* **375** (2017).
13. Lowenstam, H. A. & Weiner, S. *On Biomineralization* (Oxford Univ. Press, Oxford, 1989).
14. De Yoreo, J. J. *et al.* Crystallization by particle attachment in synthetic, biogenic, and geologic environments. *Science* **349,** aaa6760 (2015).
15. Menges, A. & Schwinn, T. Manufacturing reciprocities. *Architectural Design* **82,** 118–125 (2012).

16. Aizenberg, J., Tkachenko, A., Weiner, S., Addadi, L. & Hendler, G. Calcitic microlenses as part of the photoreceptor system in brittlestars. *Nature* **412,** 819–822 (2001).

17. Wegst, U. G. K., Bai, H., Saiz, E., Tomsia, A. P. & Ritchie, R. O. Bioinspired structural materials. *Nature Materials* **14,** 23–36 (2015).

18. Ball, P. *The Self-made Tapestry: Pattern Formation in Nature* (Oxford University Press, 1999).

19. Knippers, J. & Nickel, K. G. *Biologically-Inspired Systems Biomimetic Research for Architecture and Building Construction* (Springer International, 2016).

20. Grun, T. B. *et al.* in *Biologically-Inspired Systems Biomimetic Research for Architecture and Building Construction* (eds Knippers, J. & Nickel, K. G.) 217–242 (Springer International, 2016).

21. D'Errico, F. *et al.* Additional evidence on the use of personal ornaments in the Middle Paleolithic of North Africa. *Proceedings of the National Academy of Sciences* **106,** 16051–16056 (2009).

22. Haeckel, E. *Kunstformen der Natur* (Verlag des Bibliographischen Instituts, Leipzig, Wien, 1904).

23. Thompson, D. W. *On Growth and Form* (Cambridge University Press, London, 1917).

24. Garcia-Ruiz, J. M., Melero-Garcia, E. & Hyde, S. T. Morphogenesis of Self-Assembled Nanocrystalline Materials of Barium Carbonate and Silica. *Science* **323,** 362–365 (2009).

25. Lee, K. *et al.* Self-assembly of amorphous calcium carbonate microlens arrays. *Nature Communications* **3,** 725 (2012).

26. Mann, S. & Ozin, G. A. Synthesis of inorganic materials with complex form. *Nature* **382,** 313–318 (1996).

27. Meldrum, F. C. & Cölfen, H. Controlling Mineral Morphologies and Structures in Biological and Synthetic Systems. *Chemical Reviews* **108,** 4332–4432 (2008).

28. Miskin, M. Z. *et al.* Graphene-based bimorphs for micron-sized, tautonomous origami machines. *Proceedings of the National Academy of Sciences of the United States of America* **115,** 466–470 (2018).

29. Noorduin, W. L., Grinthal, A., Mahadevan, L. & Aizenberg, J. Rationally designed complex, hierarchical microarchitectures. *Science* **340,** 832–837 (2013).

30. Nudelman, F. & Sommerdijk, N. A. Biomineralization as an inspiration for materials chemistry. *Angewandte Chemie - International Edition* **51,** 6582–6596 (2012).

31. Studart, A. R. Towards high-performance bioinspired composites. *Advanced Materials* **24,** 5024–5044 (2012).

32. Sanchez, C., Arribart, H. & Guille, M. M. G. Biomimetism and bioinspiration as tools for the design of innovative materials and systems. *Nature Materials* **4,** 277–288 (2005).

33. Bianchi, E., Blaak, R. & Likos, C. N. Patchy colloids: State of the art and perspectives. *Physical Chemistry Chemical Physics* **13,** 6397–6410 (2011).

34. Boneschanscher, M. P. *et al.* Long-range orientation and atomic attachment of nanocrystals in 2D honeycomb superlattices. *Science* **344,** 1377–1380 (2014).

35. Shevchenko, E. V., Talapin, D. V., Kotov, N. A., O'Brien, S. & Murray, C. B. Structural diversity in binary nanoparticle superlattices. *Nature* **439,** 55–59 (2006).

36. Stebe, K. J., Lewandowski, E. & Ghosh, M. Oriented assembly of metamaterials. *Science* **325,** 159–160 (2009).

37. Yi, G.-R., Pine, D. J. & Sacanna, S. Recent progress on patchy colloids and their self-assembly. *Journal of Physics: Condensed Matter* **25,** 193101 (2013).

38. Zhang, J., Li, Y., Zhang, X. & Yang, B. Colloidal self-assembly meets nanofabrication: From two-dimensional colloidal crystals to nanostructure arrays. *Advanced Materials* **22,** 4249–4269 (2010).

39. Kovalenko, M. V. *et al.* Prospects of nanoscience with nanocrystals. *ACS Nano* **9,** 1012–1057 (2015).

40. Joannopoulos, J. & Meade, R. *Photonic crystals: molding the flow of light* (Princeton University Press, 2007).

41. Jiang, P., Prasad, T., McFarland, M. J. & Colvin, V. L. Two-dimensional nonclose-packed colloidal crystals formed by spincoating. *Applied Physics Letters* **89** (2006).

42. Hatton, B., Mishchenko, L., Davis, S., Sandhage, K. H. & Aizenberg, J. Assembly of large-area, highly ordered, crack-free inverse opal films. *Proceedings of the National Academy of Sciences of the United States of America* **107,** 10354–10359 (2010).

43. Leunissen, M. E. *et al.* Ionic colloidal crystals of oppositely charged particles. *Nature* **437,** 235–240 (2005).

44. Chen, Q., Bae, S. C. & Granick, S. Directed self-assembly of a colloidal kagome lattice. *Nature* **469,** 381–384 (2011).

45. Vogel, N. *et al.* Color from hierarchy: Diverse optical properties of micron-sized spherical colloidal assemblies. *Proceedings of the National Academy of Sciences* **112,** 10845–10850 (2015).

46. Bittarello, E. & Aquilano, D. Self-assembled nanocrystals of barium carbonate in biomineral-like structures. *European Journal of Mineralogy* **19,** 345–351 (2007).

47. Garcia-Ruiz, J. M. On the formation of induced morphology crystal aggregates. *Journal of Crystal Growth* **73,** 251–262 (1985).

48. Holtus, T. *et al.* Shape-preserving transformation of carbonate minerals into lead halide perovskite semiconductors based on ion exchange/insertion reactions. *Nature Chemistry* **10,** 740–745 (2018).

49. Kaplan, C. N. *et al.* Controlled growth and form of precipitating microsculptures. *Science* **355,** 1395–1399 (2017).

50. Kellermeier, M., Cölfen, H. & García-Ruiz, J. M. Silica Biomorphs: Complex Biomimetic Hybrid Materials from "Sand and Chalk". *European Journal of Inorganic Chemistry* **2012,** 5123–5144 (2012).

51. Knoll, P. & Steinbock, O. Inorganic Reactions Self-organize Life-like Microstructures Far from Equilibrium. *Israel Journal of Chemistry* **58,** 682–692 (2018).

52. Opel, J. *et al.* Hybrid biomimetic materials from silica/carbonate biomorphs. *Crystals* **9,** 1–8 (2019).

53. Opel, J., Wimmer, F. P., Kellermeier, M. & Cölfen, H. Functionalisation of silica-carbonate biomorphs. *Nanoscale Horizons* **1,** 144–149 (2016).

54. García-Ruiz, J. M. *et al.* Self-Assembled Silica-Carbonate Structures and Detection of Ancient Microfossils. *Science* **302,** 1194–1197 (2003).

55. Montalti, M. *et al.* Local pH oscillations witness autocatalytic self-organization of biomorphic nanostructures. *Nature Communications* **8,** 1–6 (2017).

56. Opel, J. *et al.* Symbiosis of Silica Biomorphs and Magnetite Mesocrystals. *Advanced Functional Materials* **29,** 1902047 (2019).

57. Bernáth, B. *et al.* How could the Viking Sun compass be used with sunstones before and after sunset? Twilight board as a new interpretation of the Uunartoq artefact fragment. *Proceedings of the Royal Society A: Mathematical, Physical and Engineering Sciences* **470,** 20130787 (2014).

58. Le Floch, A. *et al.* The sixteenth century Alderney crystal: a calcite as an efficient reference optical compass? *Proceedings of the Royal Society A: Mathematical, Physical and Engineering Sciences* **469,** 20120651 (2013).

59. Arago, F. Mémoire sur une modification remarquable qu'éprouvent les rayons lumineux dans leur passage a' travers certains corps diaphanes, et sue quelques autres nouveaux phénoménes d'optique. *Mémoires de la Classe des Sciences Mathématiques et Physiques de l'Institut de France* **1,** 93–134 (1811).

60. Biot, J.-B. Phenomene de polarisation successive, observés dans des fluides homogenes. *Bulletin des Sciences, par la Société Philomatique de Paris,* 190–192 (1815).

61. Lindman, K. F. Über eine durch ein isotropes System von spiralförmigen Resonatoren erzeugte Rotationspolarisation der elektromagnetischen Wellen. *Annalen der Physik* **368,** 621–644 (1920).

62. Mauguin, C. V. Sur les cristaux liquides de Lehmann. *Bulletin de la Société française de minéralogie* **34,** 71–117 (1911).

63. Pasteur, L. Mémoire sur la relation qui peuvent exister entre la forme cristalline et la composition chimique, et le sens de la polarisation rotatoire. *Comptes rendus de l'Académie des sciences* **26,** 535–538 (1848).

64. Joly, G. & Billard, J. Quelques champs électromagnétiques dans les piles de Reusch (Some electromagnetic fields in Reusch's piles). *Journal of Optics* **12,** 323 (1981).

65. Reusch, E. Untersuchung über Glimmercombinationen. *Annalen der Physik* **214,** 628–638 (1869).

66. Kertész, K. *et al.* Gleaming and dull surface textures from photonic-crystal-type nanostructures in the butterfly Cyanophrys remus. *Physical Review E* **74,** 021922 (2006).

67. Li, L. *et al.* A highly conspicuous mineralized composite photonic architecture in the translucent shell of the blue-rayed limpet. *Nature Communications* **6,** 6322 (2015).

68. Teyssier, J., Saenko, S. V., Van Der Marel, D. & Milinkovitch, M. C. Photonic crystals cause active colour change in chameleons. *Nature Communications* **6,** 1–7 (2015).

69. Vukusic, P. & Sambles, J. R. Photonic structures in biology. *Nature* **424,** 852–855 (2003).

70. Aizenberg, J., Sundar, V. C., Yablon, A. D., Weaver, J. C. & Chen, G. Biological glass fibers: Correlation between optical and structural properties. *Proceedings of the National Academy of Sciences* **101,** 3358–3363 (2004).

71. Naqshbandi, M., Canning, J., Gibson, B. C., Nash, M. M. & Crossley, M. J. nanoparticles into photonic structures. *Nature Communications* **3,** 1187–1188 (2012).

72. Arsenault, A. C., Puzzo, D. P., Manners, I. & Ozin, G. a. Photonic-crystal full-colour displays. *Nature Photonics* **1,** 468–472 (2007).

73. Colvin, V. L. From Opals to Optics: Colloidal Photonic Crystals. *MRS Bulletin* **26,** 637–641 (2001).

74. Forster, J. D. *et al.* Biomimetic isotropic nanostructures for structural coloration. *Advanced Materials* **22,** 2939 (2010).

75. Vlasov, Y. a., Bo, X. Z., Sturm, J. C. & Norris, D. J. On-chip natural assembly of silicon photonic bandgap crystals. *Nature* **414,** 289–93 (2001).

76. Ropars, G., Lakshminarayanan, V. & Le Flocha, A. The sunstone and polarised skylight: ancient Viking navigational tools? *Contemporary Physics* **55,** 302–317 (2014).

77. Choi, J. H. *et al.* Exploiting the colloidal nanocrystal library to construct electronic devices. *Science* **352,** 205–208 (2016).

78. Kundu, P. K. *et al.* Light-controlled self-assembly of non-photoresponsive nanoparticles. *Nature Chemistry* **7,** 646–652 (2015).

79. Ma, M. G. & Cölfen, H. Mesocrystals - Applications and potential. *Current Opinion in Colloid and Interface Science* **19,** 56–65 (2014).

80. Ni, S., Isa, L. & Wolf, H. Capillary assembly as a tool for the heterogeneous integration of micro- and nanoscale objects. *Soft Matter* **14,** 2978–2995 (2018).

81. Sciacca, B. *et al.* Monocrystalline Nanopatterns Made by Nanocube Assembly and Epitaxy. *Advanced Materials* **29,** 1–6 (2017).

82. Smith, M. J., Lin, C. H., Yu, S. & Tsukruk, V. V. Composite Structures with Emissive Quantum Dots for Light Enhancement. *Advanced Optical Materials* **7,** 1801072 (2019).

83. Beberwyck, B. J., Surendranath, Y. & Alivisatos, A. P. Cation exchange: A versatile tool for nanomaterials synthesis. *Journal of Physical Chemistry C* **117,** 19759–19770 (2013).

84. Steimle, B. C., Fenton, J. L. & Schaak, R. E. Rational construction of a scalable heterostructured nanorod megalibrary. *Science* **367,** 418–424 (2020).

85. De Trizio, L. & Manna, L. Forging colloidal nanostructures via cation exchange reactions. *Chemical Reviews* **116,** 10852–10887 (2016).

86. Hodges, J. M., Kletetschka, K., Fenton, J. L., Read, C. G. & Schaak, R. E. Sequential Anion and Cation Exchange Reactions for Complete Material Transformations of Nanoparticles with Morphological Retention. *Angewandte Chemie - International Edition* **54,** 8669–8672 (2015).

87. Powell, A. E., Hodges, J. M. & Schaak, R. E. Preserving Both Anion and Cation Sublattice Features during a Nanocrystal Cation-Exchange Reaction: Synthesis of Metastable Wurtzite-Type CoS and MnS. *Journal of the American Chemical Society* **138,** 471–474 (2016).

88. Son, D. H., Hughes, S. M., Yin, Y. & Alivisatos, A. P. Cation exchange reactions in ionic nanocrystals. *Science* **306,** 1009–1012 (2004).

89. Groeneveld, E. *et al.* Tailoring ZnSe-CdSe colloidal quantum dots via Cation Exchange: From core/shell to alloy nanocrystals. *ACS Nano* **7,** 7913–7930 (2013).

90. Fedorov, V. A., Ganshin, V. A. & Korkishko, Y. N. Ion exchange in II–VI crystals: Thermodynamics, kinetics, and technology. *Physica Status Solidi (a)* **139,** 9–65 (1993).

91. Putnis, A. Mineral replacement reactions: from macroscopic observations to microscopic mechanisms. *Mineralogical Magazine* **66,** 689–708 (2002).

92. Ramaswamy, R. V. & Srivastava, R. Ion-Exchanged Glass Waveguides: A Review. *Journal of Lightwave Technology* **6,** 984–1000 (1988).

93. Le Chatelier, H. Sur un énoncé général des lois des équilibres chimiques. *Comptes-rendus de l'Académie des sciences* **99,** 786–789 (1884).

94. Wu, H. L. *et al.* Formation of pseudomorphic nanocages from Cu2O nanocrystals through anion exchange reactions. *Science* **351,** 1306–1310 (2016).

95. Miszta, K. *et al.* Nanocrystal film patterning by inhibiting cation exchange via electron-beam or X-ray lithography. *Nano Letters* **14,** 2116–2122 (2014).

96. Palazon, F., Akkerman, Q. A., Prato, M. & Manna, L. X-ray Lithography on Perovskite Nanocrystals Films: From Patterning with Anion-Exchange Reactions to Enhanced Stability in Air and Water. *ACS Nano* **10,** 1224–1230 (2016).

97. Castells, M. *The Rise of the Network Society* 2nd ed. (Wiley Blackwell, Malden, 2010).

98. Chelikowsky. in *Silicon:Evolution and Future of a Technology* (eds Siffert, P. & Krimmel, E. F.) 1–20 (Springer Berlin Heidelberg, 2004).

99. Williams, J. B. *The electronics revolution : inventing the future* (Springer Praxis Books, 2017).

100. Green, M. A. *et al.* Solar cell efficiency tables (Version 55). *Progress in Photovoltaics: Research and Applications* **28,** 3–15 (2020).

101. Moore, G. E. *Understanding Moore's law: four decades of innovation* (Chemical Heritage Press, Philadelphia, 2006).

102. Akkerman, Q. A., Rainò, G., Kovalenko, M. V. & Manna, L. Genesis, challenges and opportunities for colloidal lead halide perovskite nanocrystals. *Nature Materials* **17,** 394–405 (2018).

103. Green, M. A. & Ho-Baillie, A. Perovskite Solar Cells: The Birth of a New Era in Photovoltaics. *ACS Energy Letters* **2,** 822–830 (2017).

104. Stranks, S. D. & Snaith, H. J. Metal-halide perovskites for photovoltaic and light-emitting devices. *Nature Nanotechnology* **10,** 391–402 (2015).

105. Kojima, A., Teshima, K., Shirai, Y. & Miyasaka, T. Organometal halide perovskites as visible-light sensitizers for photovoltaic cells. *Journal of the American Chemical Society* **131,** 6050–6051 (2009).

106. Rose, G. Ueber einige neue Mineralien des Urals. *Journal fuer Praktische Chemie* **19,** 459–468 (1840).

107. Chen, Q. *et al.* All-inorganic perovskite nanocrystal scintillators. *Nature* **561,** 88–93 (2018).

108. Lee, W. *et al.* High-Resolution Spin-on-Patterning of Perovskite Thin Films for a Multiplexed Image Sensor Array. *Advanced Materials* **29,** 1–7 (2017).

109. Wei, H. *et al.* Sensitive X-ray detectors made of methylammonium lead tribromide perovskite single crystals. *Nature Photonics* **10,** 333–339 (2016).

110. Wei, Y., Cheng, Z. & Lin, J. An overview on enhancing the stability of lead halide perovskite quantum dots and their applications in phosphor-converted LEDs. *Chemical Society Reviews* **48,** 310–350 (2019).

111. Xue, J. *et al.* Narrowband Perovskite Photodetector-Based Image Array for Potential Application in Artificial Vision. *Nano Letters* **18,** 7628–7634 (2018).

112. Zhang, F. *et al.* Brightly luminescent and color-tunable colloidal CH3NH3PbX3 (X = Br, I, Cl) quantum dots: Potential alternatives for display technology. *ACS Nano* **9,** 4533–4542 (2015).

113. Wong, Y. C. *et al.* Color Patterning of Luminescent Perovskites via Light-Mediated Halide Exchange with Haloalkanes. *Advanced Materials* **31,** 1–7 (2019).

114. Chen, J. *et al.* Simple and Fast Patterning Process by Laser Direct Writing for Perovskite Quantum Dots. *Advanced Materials Technologies* **2,** 1–7 (2017).

115. Kamminga, M. E. *et al.* Micropatterned 2D Hybrid Perovskite Thin Films with Enhanced Photoluminescence Lifetimes. *ACS Applied Materials and Interfaces* **10,** 12878–12885 (2018).

116. Kim, B. H. *et al.* High-resolution patterns of quantum dots formed by electrohydrodynamic jet printing for light-emitting diodes. *Nano Letters* **15,** 969–973 (2015).

117. Lin, C. H. *et al.* Large-Area Lasing and Multicolor Perovskite Quantum Dot Patterns. *Advanced Optical Materials* **6,** 1–9 (2018).

118. Lin, C.-K. *et al.* Two-Step Patterning of Scalable All-Inorganic Halide Perovskite Arrays. *ACS Nano* **14,** 3500–3508 (2020).

119. Wang, G. *et al.* Wafer-scale growth of large arrays of perovskite microplate crystals for functional electronics and optoelectronics. *Science Advances* **1,** 1–9 (2015).

120. Lei, Y. *et al.* A fabrication process for flexible single-crystal perovskite devices. *Nature* **583,** 790–795 (2020).

121. Zhang, C. *et al.* Conversion of invisible metal-organic frameworks to luminescent perovskite nanocrystals for confidential information encryption and decryption. *Nature Communications* **8,** 1138 (2017).

122. Tan, Z.-K. *et al.* Bright light-emitting diodes based on organometal halide perovskite. *Nature Nanotechnology* **9,** 687–692 (2014).

123. Anthony, J. W., Bideaux, R. A., Bladh, K. W. & Nichols, M. C. *Handbook of Mineralogy Crystal Data* (Mineralogical Society of America, 2010).

124. Palik, E. D. *Handbook of optical constants of solids* (Academic Press, San Diego, 1985).

125. Nichols, S., Arteaga, O., Martin, A. & Kahr, B. Measurement of transmission and reflection from a thick anisotropic crystal modeled by a sum of incoherent partial waves. *Journal of the Optical Society of America A* **32,** 2049–2057 (2015).

126. Arteaga, O., Freudenthal, J., Wang, B. & Kahr, B. Mueller matrix polarimetry with four photoelastic modulators: Theory and calibration. *Applied Optics* **51,** 6805–6817 (2012).

127. Mohtashami, A., Osorio, C. I. & Koenderink, A. F. Angle-Resolved Polarimetry of Antenna-Mediated Fluorescence. *Physical Review Applied* **4,** 1–7 (2015).

128. Vdovin, G. & van Goor, F. LightPipes: beam propagation toolbox. *OKO Technologies, The Netherlands* (1999).

129. Azzam, R. M. Propagation of partially polarized light through anisotropic media with or without depolarization: A differential 4×4 matrix calculus. *Journal of the Optical Society of America* **68,** 1756–1767 (1978).

130. Goldstein, D. H. Mueller matrix dual-rotating retarder polarimeter. *Applied Optics* **31,** 6676–6683 (1992).

131. Chen, C. *et al.* Multichannel Mueller matrix ellipsometer based on the dual rotating compensator principle. *Thin Solid Films* **455-456,** 14–23 (2004).

132. Nichols, S. M. *Coherence in polarimetry* PhD thesis (New York University, 2018).

133. Arteaga, O. & Kahr, B. Mueller matrix polarimetry of bianisotropic materials [Invited]. *Journal of the Optical Society of America B* **36,** F72–F83 (2019).

134. Freudenthal, J. H., Hollis, E. & Kahr, B. Imaging chiroptical artifacts. *Chirality* **21,** E20–E27 (2009).

135. Ossikovski, R. & De Martino, A. Differential Mueller matrix of a depolarizing homogeneous medium and its relation to the Mueller matrix logarithm. *Journal of the Optical Society of America A* **32,** 343–348 (2015).

136. Ulrich, R. & Simon, A. Polarization optics of twisted single-mode fibers. *Applied Optics* **18,** 2241–2251 (1979).

137. Smith, A. M. Birefringence induced by bends and twists in single-mode optical fiber. *Applied Optics* **19,** 2606–2611 (1980).

138. Aizenberg, J., Muller, D. A., Grazul, J. L. & Hamann, D. R. Direct fabrication of large micropatterned single crystals. *Science* **299,** 1205–1208 (2003).

139. Jiang, W. *et al.* Chiral acidic amino acids induce chiral hierarchical structure in calcium carbonate. *Nature Communications* **8,** 1–13 (2017).

140. Fratzl, P. Biomimetic materials research: What can we really learn from nature's structural materials? *Journal of the Royal Society Interface* **4,** 637–642 (2007).

141. Giosia, M. D. *et al.* Bioinspired Nanocomposites: Ordered 2D Materials Within a 3D Lattice. *Advanced Functional Materials* **26,** 5569–5575 (2016).

142. Xu, S. *et al.* Assembly of micro/nanomaterials into complex, three-dimensional architectures by compressive buckling. *Science* **347,** 154–159 (2015).

143. Nie, Z., Petukhova, A. & Kumacheva, E. Properties and emerging applications of self-assembled structures made from inorganic nanoparticles. *Nature Nanotechnology* **5,** 15–25 (2010).

144. Bao, Z. *et al.* Chemical reduction of three-dimensional silica micro-assemblies into microporous silicon replicas. *Nature* **446,** 172–175 (2007).

145. Mann, S. *Biomineralization* (Oxford Univ. Press, Oxford, 2002).

146. Sandhage, K. H. *et al.* Novel, bioclastic route to self-assembled, 3D, chemically tailored meso/nanostructures: Shape-preserving reactive conversion of biosilica (diatom) microshells. *Advanced Materials* **14,** 429–433 (2002).

147. Wu, H. *et al.* Electrospun metal nanofiber webs as high-performance transparent electrode. *Nano Letters* **10,** 4242–4248 (2010).

148. Geuchies, J. J. *et al.* In situ study of the formation mechanism of two-dimensional superlattices from PbSe nanocrystals. *Nature Materials* **15,** 1248–1254 (2016).

149. Miszta, K. *et al.* Hierarchical self-assembly of suspended branched colloidal nanocrystals into superlattice structures. *Nature Materials* **10,** 872–876 (2011).

150. Zhang, W., Eperon, G. E. & Snaith, H. J. Metal halide perovskites for energy applications. *Nature Energy* **1,** 16048 (2016).

151. Polman, A. & Atwater, H. A. Photonic design principles for ultrahigh-efficiency photovoltaics. *Nature Materials* **11,** 174–177 (2012).

152. Johlin, E., Mann, S. A., Kasture, S., Koenderink, A. F. & Garnett, E. C. Broadband highly directive 3D nanophotonic lenses. *Nature Communications* **9,** 4742 (2018).

153. Chen, K. & Tüysüz, H. Morphology-Controlled Synthesis of Organometal Halide Perovskite Inverse Opals. *Angewandte Chemie - International Edition* **54,** 13806–13810 (2015).

154. Ashley, M. J. *et al.* Templated Synthesis of Uniform Perovskite Nanowire Arrays. *Journal of the American Chemical Society* **138,** 10096–10099 (2016).

155. Burschka, J. *et al.* Sequential deposition as a route to high-performance perovskite-sensitized solar cells. *Nature* **499,** 316–319 (2013).

156. Sheng, R. *et al.* Methylammonium lead bromide perovskite-based solar cells by vapor-assisted deposition. *Journal of Physical Chemistry C* **119,** 3545–3549 (2015).

157. Yuan, K., Lee, S. S., De Andrade, V., Sturchio, N. C. & Fenter, P. Replacement of calcite (CaCO3) by Cerussite (PbCO3). *Environmental Science and Technology* **50,** 12984–12991 (2016).

158. Lide, D. R. *CRC Handbook of Chemistry and Physics, Internet Version 2005* (CRC Press, Boca Raton, FL, 2005).

159. Niu, G. *et al.* Study on the stability of CH NH3 PbI3 films and the effect of post-modification by aluminum oxide in all-solid-state hybrid solar cells. *J. Mater. Chem. A* **2,** 705–710 (2014).

160. Tenuta, E., Zheng, C. & Rubel, O. Thermodynamic origin of instability in hybrid halide perovskites. *Scientific Reports* **6,** 1–8 (2016).

161. Eperon, G. E. *et al.* The Importance of Moisture in Hybrid Lead Halide Perovskite Thin Film Fabrication. *ACS Nano* **9,** 9380–9393 (2015).

162. Weatherspoon, M. R., Allan, S. M., Hunt, E., Cai, Y. & Sandhage, K. H. Sol-gel synthesis on self-replicating single-cell scaffolds: applying complex chemistries to nature's 3-D nanostructured templates. *Chemical Communications* **5,** 651 (2005).

163. Dorsey, K. J. *et al.* Atomic Layer Deposition for Membranes, Metamaterials, and Mechanisms. *Advanced Materials* **31,** 1–6 (2019).

164. Dieleman, C. D. *et al.* Universal direct patterning of colloidal quantum dots by (extreme) ultraviolet and electron beam lithography. *Nanoscale* **12,** 11306–11316 (2020).

165. Jackman, R. J., Wilbur, J. L. & Whitesides, G. M. Fabrication of submicrometer features on curved substrates by microcontact printing. *Science* **269,** 664–666 (1995).

166. Klajn, R. *et al.* Multicolour micropatterning of thin films of dry gels. *Nature Materials* **3,** 729–735 (2004).

167. Kraus, T. *et al.* Nanoparticle printing with single-particle resolution. *Nature Nanotechnology* **2,** 570–576 (2007).

168. Perl, A., Reinhoudt, D. N. & Huskens, J. Microcontact printing: Limitations and achievements. *Advanced Materials* **21,** 2257–2268 (2009).

169. Hong, L. *et al.* Guanine-Stabilized Formamidinium Lead Iodide Perovskites. *Angewandte Chemie International Edition* **59,** 4691–4697 (2020).

170. Zhumekenov, A. A. *et al.* Formamidinium Lead Halide Perovskite Crystals with Unprecedented Long Carrier Dynamics and Diffusion Length. *ACS Energy Letters* **1,** 32–37 (2016).

171. Kim, Y. T. H. *et al.* High efficiency perovskite light-emitting diodes of ligand-engineered colloidal formamidinium lead bromide nanoparticles. *Nano Energy* **38,** 51–58 (2017).

172. Fang, H. *et al.* Few-layer formamidinium lead bromide nanoplatelets for ultrapure-green and high-efficiency light-emitting diodes. *Nano Research* **12,** 171–176 (2019).

173. Anaf, W., Schalm, O., Janssens, K. & De Wael, K. Understanding the (in)stability of semiconductor pigments by a thermodynamic approach. *Dyes and Pigments* **113,** 409–415 (2015).

174. Cennini, C. & Tambroni, G. *Di Cennino Cennini trattato della pittura* (Paolo Salviucci, Rome, 1821).

175. Fiedler, I. & Bayard, M. a. in *Artists'Pigments - A Handbook of their History and Characteristics* (ed Feller, R. L.) 104–105 (National Gallery of Art, Washington, 1986).

176. Rahemi, V. *et al.* Unique Optoelectronic Structure and Photoreduction Properties of Sulfur-Doped Lead Chromates Explaining Their Instability in Paintings. *Analytical Chemistry* **89,** 3326–3334 (2017).

177. Bargardi, F. L., Le Ferrand, H., Libanori, R. & Studart, A. R. Bio-inspired self-shaping ceramics. *Nature Communications* **7,** 1–8 (2016).

178. Begley, M. R., Gianola, D. S. & Ray, T. R. Bridging functional nanocomposites to robust macroscale devices. *Science* **364,** eaav4299 (2019).

179. Eder, M., Amini, S. & Fratzl, P. Biological composites—complex structures for functional diversity. *Science* **362,** 543–547 (2018).

Summary

Patterns in nature can be observed at all length scales, planets arrange in solar systems, sand grains into dunes, and atoms into crystals. All these patterns are self-assembled without human contribution. Some of the most intricate patterns occur in biologically controlled systems where organisms use deliberate patterning and organization of matter to create a vast variety of materials, each specific for their application. Evolution shaped their properties in many ways, for instance, towards outstanding hardness, for lightweight finesse, or even both. Also, such self-assembled systems can be tailored, even down to a scale where photonic effects arise. Often, these functionalities emerge from nanoscopic building blocks that form a microscopic ensemble. Human-made architectures aim at mimicking or even outperforming their natural counterparts, reaching incredible precision on the nanometer scale. However, this commonly requires expensive and laborious manufacturing techniques, while in nature, patterns emerge seemingly effortless through an interplay of biologically controlled physical and chemical processes. Thus, strategies that allow for creating synthetic patterns, in a programmable manner, but with the effortlessness of biological systems, have the potential to lead to a paradigm shift in fabrication techniques.

FIGURE S1: Self-assembled microarchitecture composed of $BaCO_3$ nanocrystals and amorphous SiO_2 (structure width: 26 µm).

This thesis, titled "Ion Exchange, Self-Assembly, and Light Emission — A Dance of Ions and Light", explores two bioinspired strategies for creating architectures with optical functions. First, we explore a self-assembly approach to create microscopic architectures with user-defined shapes and demonstrate their ability to manipulate light. Second, we develop ion exchange reactions to turn these architectures into light-emitting semiconductors. Based on these results, we create spatial patterns of these semiconductors by developing a method to locally apply ion exchange reactions onto surfaces.

The cover of this thesis shows the result of a self-assembly process for constructing a variety of architectures, such as microscopic vase-, stem-, helix-, and coral-like shapes (Figure S1). Although the synthesis is very simple, requiring only water, barium ions, and silicate, the resulting architectures are remarkably complex. The architectures emerge from the interplay between two processes. Barium forms barium carbonate ($BaCO_3$) in the presence of atmospheric CO_2, which triggers silicate to polymerize to silica (SiO_2). As these two processes take place simultaneously, this so-called coprecipitation yields a brick-and-mortar structure of nanocrystals and silica. Manipulating the reaction conditions allows to shape the resulting architectures into user-defined shapes.

In **chapter 2**, we manipulate light using self-assembled barium carbonate/silica ($BaCO_3/SiO_2$) helices. To study how light behaves when traveling through the microarchitecture, we embed fluorescent molecules as an internal light source inside the structure. Light is emitted internally and subsequently reflected on the inside of the helix until it leaves the tip in a narrow emission-angle. By analyzing light emission from helices with different orientations, we find that helices behave as directional emitters (Figure S2a).

Furthermore, we study the interaction between light and the internal nanocrystalline layout of the helices by characterizing the polarization of the transmitted light. The fundamental building blocks of these helices are barium carbonate nanorods with a different refractive index along the long versus the short axis. Their arrangement follows the twist of the helix and is thus chiral. We find that light passing through this helical stack of crystals experiences a rotation of polarization, specific to the handedness of the helix (Figure S2b, c). The stack of nanocrystals thus has a different refractive index for left- versus right-handed circular polarized light, whereas the individual nanocrystals do not show this behavior. These results demonstrate the potential of self-assembly processes to organize simple building blocks across multiple length scales into hierarchical order. From this, optical functionality emerges, which is absent in the individual building blocks alone.

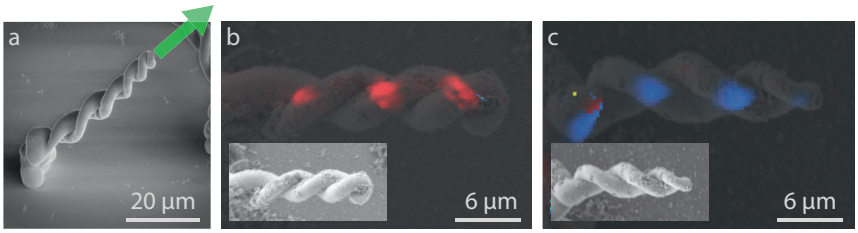

FIGURE S2: Directed emission and circular retardance from microhelices. a) Self-assembled micro helices act as directional emitters. b, c) Orthogonal to their long axis, they exhibit handedness-specific circular retardance.

In **chapter 3**, we develop an ion exchange route to convert $BaCO_3/SiO_2$ architectures into light-emitting semiconductors. Although a wide variety of shapes can be produced from the coprecipitation of $BaCO_3$ and SiO_2, this synthesis cannot facilely be expanded to other material compositions. To overcome this entanglement between the synthesis route and the material composition, we sought inspiration in a field with similar challenges—nanoparticle fabrication. There, routes have been developed to change the composition of nanoparticles after synthesis by exchanging the ions. Typically, ion exchange reactions have been developed for individual nanocrystals in solution—here, we explore applying these principles to ensembles of nanocrystals such as the barium carbonate microarchitectures and biominerals.

To demonstrate the proof-of-principle, we develop an ion exchange route to convert $BaCO_3/SiO_2$ architectures into light-emitting methylammonium lead halide perovskite semiconductors ($MAPbX_3$, with X=Cl, Br, or I). The outstanding optoelectronic properties of perovskites make them one of the most researched materials for solar cells at this moment. Based on a crystallographic analysis, we develop a route from $BaCO_3$ over $PbCO_3$ to PbX_2, and finally $MAPbX_3$. $BaCO_3$, $PbCO_3$, and PbX_2 crystallize in the same crystal lattice, which facilitates the ion exchange. PbX_2 is a common precursor for the synthesis of $MAPbX_3$. We performed the cation exchange in two steps: first, we convert $BaCO_3$ to $PbCO_3$ by immersing the architectures in a solution with lead ions. Subsequently, the $PbCO_3$ converts in a cascade anion exchange reaction to PbX_2 and further to $MAPbX_3$ by exposing the architectures to MAX (Figure S3a–e).

We find that these shape-preserving chemical conversions are possible due to a combination of factors. The similarities in crystal structure enable a replacement of ions and rearrangement into the perovskite crystal structure. The nanocomposite architecture facilitates the ion exchange owning to the fact that nanocrystals are faster to exchange than bulk materials, while the silica matrix may act as a stabilizing scaffold that allows transport of ions. These insights suggest that the same principles enable the ion exchange of other hierarchically structured nanocomposites.

Biominerals such as the skeleton of a sand dollar are also composed of carbonate nanocrystals ($CaCO_3$), which allowed us also converting these into semiconductors (Figure S3f). Overall, this is an essential step towards independent control over both the shape and composition of 3D functional materials, showing that we may leverage a self-assembly approach, which gives the desired microarchitecture, with an ion exchange route, which yields the targeted composition to create tailored functional materials.

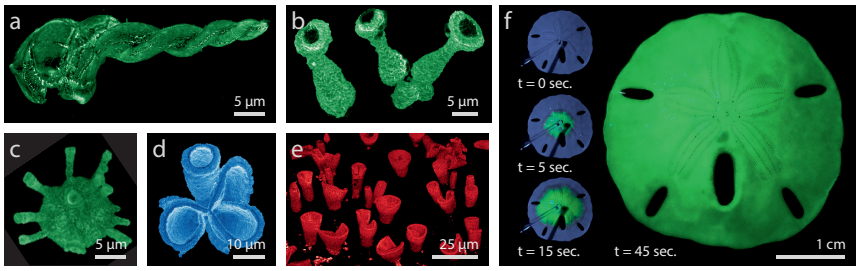

FIGURE S3: Conversion to methylammonium lead halide perovskite. a-e) Microarchitectures converted into different perovskite semiconductors. The colors seen in the micrographs are the light emission as measured with cathodoluminescence microscopy. Blue, green, and red emission originate from methylammonium lead chloride, bromide, and iodide, respectively. f) Timeseries showing the conversion of a sand dollar skeleton into perovskite, emitting green light under UV irradiation.

In **chapter 4**, we develop a process to integrate patterns of semiconductors into an insulating film by locally performing the ion exchange reactions developed in chapter 3 on a film. The ability to create such patterns is essential for many integrated (opto-)electronic devices such as displays and photodetectors. In analogy to conventional lithography for print, we develop a new technique that we coin ion exchange lithography (IEL). In IEL, a reactive nanoparticle film that acts as a "canvas" is locally converted into a desirable composition by adding ion-exchange "inks". The "inks" are methylammonium or formamidium halides that can transform the "canvas", a $PbCO_3$ nanoparticle film, into light-emitting, semiconducting perovskites. We apply the ink via customized stamps, traditional paint brushes, and airbrushing onto the canvas to locally create luminescent perovskite (Figure S4). The color of emission of the perovskite can be tuned from blue to green and further to red by adjusting the ratio between chloride, bromide, and iodide in the ink. Moreover, we show that the IEL approach can be integrated into the fabrication of (opto)electronic devices such as light-emitting diodes (LED). While conventional cleanroom techniques tend to be expensive and laborious, the simplicity, scalability, versatility, and customizability of IEL make it a promising route for integrated devices. Building on the many ion exchange reactions that

have already been developed in liquids, we ultimately envision fully printed devices with ion exchange lithography.

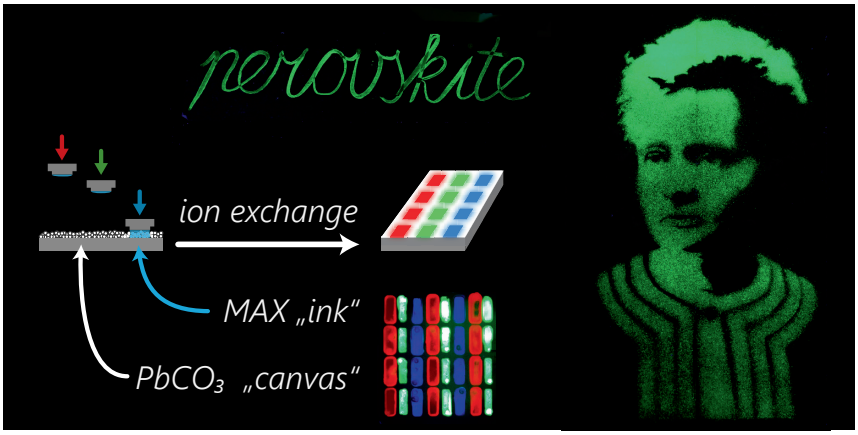

FIGURE S4: Ion Exchange Lithography. Top: fluorescence photograph of a pattern drawn by applying the conversion ink with a paintbrush. Left: schematic illustration showing the fabrication of a spatially patterned perovskite film. Center bottom: fluorescence photograph of multicolor contact printed pixels. Right: airbrush painting of Marie Skłodowska-Curie.

Overall, this thesis explores ion exchange, self-assembly, and light emission for functional optical materials. Nature-inspired self-assembly has the power to assemble composite materials such that functionality emerges from the hierarchical order within. Here, we witnessed the remarkable transition from an aqueous solution of metal salt without chiral order to microscopic helices that rotate light. Inherently, the synthesis of a material determines its final composition. In our case, metal salts, carbonate, and silicate form hierarchical metal carbonate/silica architectures. These architectures enable light manipulation, but other functionalities such as emitting light would require a different material composition that cannot be accessed via the same synthesis route. Conventionally, materials have been regarded as permanently defined by their constituting elements. Here, ion exchange reactions bring an opportunity to change material compositions post-synthesis. We harness the potential of the assembly process to form metal carbonate microarchitectures and, through ion exchange reactions, change the material composition to create a light-emitting perovskite. The possibility to change material composition is taken one step further through performing ion exchange reactions selectively on some areas of the material. Instead of positioning multiple materials next to each other, we can program the conversion of one material into different materials locally.

In optoelectronics, self-assembly could upgrade devices with optical elements that are otherwise too expensive to manufacture. Combined with ion exchange,

self-assembly could introduce three-dimensional elements into conventionally two-dimensional routes such as optical and e-beam lithography. Collectively, these approaches may lead to integrated devices fully designed through self-assembly and ion exchange. Essentially, optoelectronics is a case study; the same concept holds potential for many fields, for example, catalysis and batteries. Ultimately, the increasing control over artificial self-assembly processes, combined with the versatility of ion exchange routes, will allow us to fabricate architectures and materials that are inaccessible with our current fabrication techniques.

Samenvatting

In de natuur zijn er patronen op alle lengteschalen: planeten ordenen zich in zonnestelsels, zandkorrels in duinen, en atomen in kristallen. Al deze patronen vormen zich spontaan zonder menselijke inbreng. Levende organismen sturen de vorming van complexe patronen om zo een grote diversiteit aan functionele materialen te creëren. Evolutie heeft deze patronen geoptimaliseerd voor specifieke toepassingen, zodat eigenschappen zoals uitstekende hardheid, lichtgewicht finesse, of zelfs beiden ontstaan. Dergelijke zelfgeassembleerde systemen vormen patronen tot op een dermate kleine schaal dat er optische functies ontstaan. Vaak ligt de oorsprong van deze functionaliteiten in de formatie van een microscopisch ensemble bestaande uit nanoscopische bouwstenen. Kunstmatige architecturen hebben de ambitie om hun natuurlijke pendant te imiteren of zelfs te overtreffen, waarbij een geweldige precisie wordt bereikt op nanometerschaal. Dit vereist meestal dure en moeizame fabricagetechnieken, terwijl in de natuur vergelijkbare patronen schijnbaar moeiteloos tot stand komen door een biologisch gecontroleerd samenspel van fysische en chemische processen. Strategieën die het mogelijk maken om synthetische patronen te creëren op een programmeerbare manier met de moeiteloosheid van biologische systemen, hebben daarom het potentieel om te leiden tot een paradigmaverschuiving in productietechnieken.

FIGUUR S1: Zelfgeassembleerde microarchitectuur bestaande uit $BaCO_3$ nanokristallen en amorfe SiO_2 (structuurbreedte: 26 µm).

Dit proefschrift, getiteld *"Ion Exchange, Self-Assembly, and Light Emission — A Dance of Ions and Light"* (Ion-uitwisseling, zelf-assemblage en licht emissie — een dans van ionen en licht), onderzoekt twee biologisch geïnspireerde strategieën voor het creëren van architecturen met optische functies. Ten eerste onderzoeken we een zelfassemblage methode om microscopische architecturen met gedefinieerde vormen te creëren en demonstreren we hun vermogen om licht te manipuleren. Ten tweede ontwikkelen we ionen uitwisselingsreacties om deze architecturen om te zetten in lichtgevende halfgeleiders. Op basis van deze resultaten ontwikkelen we een methode om patronen van deze halfgeleiders te kunnen maken met lokale ionen uitwisselingsreacties.

De kaft van dit proefschrift toont het resultaat van een zelfassemblage proces voor het maken van diverse microscopische architecturen, zoals vaas-, stengel-, helix-, en koraalachtige vormen (Figuur S1). De synthese is zeer eenvoudig en vereist slechts barium-ionen en silicaat in water, maar de resulterende architecturen zijn opmerkelijk complex. Deze complexiteit ontstaat uit het samenspel tussen twee processen. Doordat barium in de aanwezigheid van atmosferische CO_2 bariumcarbonaat ($BaCO_3$) vormt, wordt silicaat gepolymeriseerd tot siliciumdioxide (SiO_2). Omdat deze twee processen gelijktijdig plaatsvinden, levert deze zogenaamde co-precipitatie een baksteen- en mortelstructuur van nanokristallen en siliciumdioxide op. Door het manipuleren van de reactiecondities is het mogelijk om de vorm van de resulterende architecturen te programmeren.

In **hoofdstuk 2** manipuleren we licht met behulp van zelfgeassembleerde bariumcarbonaat/silica ($BaCO_3/SiO_2$) helices. Om te onderzoeken hoe het licht zich gedraagt tijdens het passeren van de microarchitectuur bouwen we fluorescerende moleculen in de helix als een interne lichtbron. Het licht wordt geëmitteerd en vervolgens gereflecteerd op de binnenkant van de helix tot het de tip verlaat onder een nauwe emissie-hoek. Door het analyseren van de lichtemissie van helices met verschillende oriëntaties, vinden we dat helices zich gedragen als richtinggevende stralers (Figuur S2a).

We onderzoeken ook de interactie tussen licht en de interne nanokristallijne opbouw van de helices door het analyseren van de polarisatie van het doorgelaten licht. De fundamentele bouwstenen van deze helices zijn staafvormige bariumcarbonaat nanokristallen die een verschillende brekingsindex hebben in de lengte en breedte. De ordening van de staafjes volgt de draaiing van de helix en is daardoor chiraal. We vinden dat het licht dat door deze spiraalvormige stapel kristallen gaat een rotatie van polarisatie ervaart die specifiek is voor de handigheid van de helix (Figuur S2b, c). De stapel nanokristallen heeft dus een verschillende brekingsindex voor links- versus rechtshandig circulair gepolariseerd licht, terwijl de individuele nanokristallen dit fenomeen niet tonen. Deze resultaten demonstreren het potentieel van zelfassemblage processen om eenvoudige bouwstenen te organiseren over meerdere lengteschalen in hiërarchische orde. Hieruit ontstaat optische functionaliteit die afwezig is in de individuele bouwstenen.

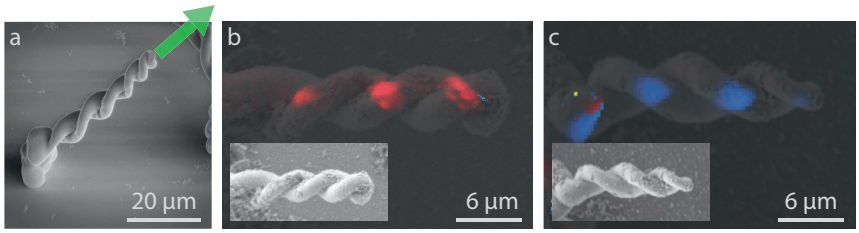

FIGUUR S2: Gerichte emissie en circulaire polarisatie van microhelices. a) Zelfgeassembleerde microhelices fungeren als richtinggevende stralers. b, c) Orthogonaal ten opzichte van hun lange as vertonen ze handigheidsspecifieke circulaire polarisatie.

In **hoofdstuk 3** ontwikkelen we een ionen uitwisselingsroute om $BaCO_3/SiO_2$ architecturen om te zetten in lichtgevende halfgeleiders. Alhoewel een grote diversiteit aan vormen kan worden gerealiseerd door de co-precipitatie van $BaCO_3$ en SiO_2, kan deze synthese niet gemakkelijk worden toegepast op andere materiaalsamenstellingen. Om deze afhankelijkheid tussen de syntheseroute en de materiaalsamenstelling te overkomen hebben we inspiratie gezocht in een veld met vergelijkbare uitdagingen—het fabriceren van nanodeeltjes. Daar zijn routes ontwikkeld om de samenstelling van nanodeeltjes te veranderen na de synthese door uitwisseling van ionen. Tot nu toe zijn de meeste uitwisselingsreacties van ionen ontwikkeld voor individuele nanokristallen in oplossingen. Hier onderzoeken we de toepassing van deze principes in ensembles van nanokristallen zoals de bariumcarbonaat microarchitecturen en biomineralen.

Om het principe te verifiëren, ontwikkelen we een ionen uitwisselingsroute om $BaCO_3/SiO_2$ architecturen om te zetten in lichtgevende methylammonium loodhalogenide perovskiet halfgeleiders ($MAPbX_3$, met X=Cl, Br, of I). De uitstekende opto-elektronische eigenschappen van perovskieten maken ze een van de meest onderzochte materialen voor zonnecellen op dit moment. Op basis van een kristallografische analyse ontwikkelen we een route van $BaCO_3$ naar lood carbonaat ($PbCO_3$). Vervolgens zetten we deze $PbCO_3$ vormen in één stap om naar de pervoskiet ($MAPbX_3$) via een intermediare loodhalide (PbX_2). We voerden de kationenuitwisseling uit in twee stappen: eerst zetten we $BaCO_3$ om in $PbCO_3$ door de architecturen in een oplossing met loodionen te dompelen. Aansluitend zetten wij de $PbCO_3$ in een cascade van anionen uitwisselingsreacties eerst om naar PbX_2 en vervolgens naar $MAPbX_3$ door de architecturen met methylammoniumhalide (MAX) in contact te brengen (Figuur S3a–e).

We constateren dat deze vormbehoudende chemische omzettingen mogelijk zijn door een combinatie van factoren. De overeenkomsten in de kristalstructuur maken een vervanging van ionen en een reorganisatie in de perovskietkristalstructuur mogelijk. De nanocomposiet architectuur faciliteert de ionenuitwisseling, aangezien nanokristallen sneller kunnen worden uitgewisseld dan bulkmaterialen, terwijl de silicamatrix als een stabiliserende structuur fungeert die het transport

van ionen mogelijk maakt. Deze inzichten suggereren dat dezelfde principes ook de ionenuitwisseling van andere hiërarchisch gestructureerde nanocomposieten mogelijk maken.

We onderzoeken deze potentie voor biologische gevormde mineralen, zoals het skelet van een zanddollar. Dit is ook samengesteld uit metaalcarbonaat nanokristallen ($CaCO_3$), waardoor we deze konden omzetten in halfgeleiders (Figuur S3f). Al met al is dit een essentiële stap in de richting van onafhankelijke controle over zowel de vorm alsook de samenstelling van 3D-functionele materialen. Dit laat zien dat we een zelfassemblage aanpak kunnen combineren met een ionen uitwiselingsroute, om zo functionele materialen met de gewenste microarchitectuur en samenstelling op maat te maken.

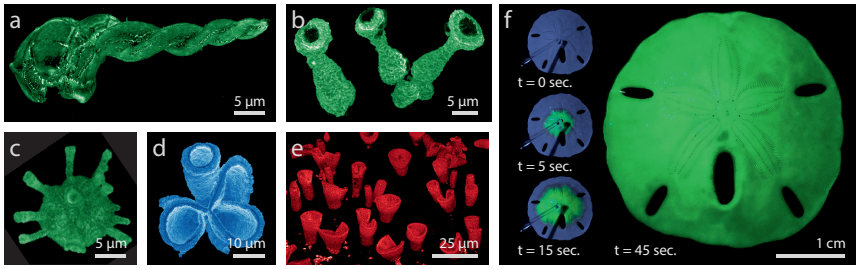

FIGUUR S3: Omzetting naar methylammonium loodhalogenide perovskieten. a-e) Microarchitecturen omgezet in verschillende perovskiet-halfgeleiders. De kleuren zijn de lichtemissie zoals gemeten met kathodoluminescentiemicroscopie. De blauwe, groene en rode emissie is afkomstig van methylammoniumloodchloride, -bromide en -jodide. f) Tijdseries die de omzetting van een zanddollarskelet in perovskiet laten zien. De perovskiet straalt groen licht uit onder UV-belichting.

In **hoofdstuk 4** ontwikkelen we een proces om patronen van halfgeleiders te integreren in een isolerende film door lokaal de in hoofdstuk 3 ontwikkelde ionenwisselingsreacties op een film uit te voeren. Het vermogen om dergelijke patronen te creëren is essentieel voor vele geïntegreerde (opto-)elektronische apparaten, zoals displays en fotodetectoren. Naar analogie van de traditionele lithografie voor drukwerk, ontwikkelen we een nieuwe techniek die wij *"ion exchange lightography"* (IEL, ionenuitwisselings lithografie) noemen. In IEL wordt een reactieve nanodeeltjesfilm, die fungeert als "canvas", lokaal omgezet in een gewenste samenstelling door het toevoegen van ionenwisselende ïnkten". De ïnkten"zijn methylammonium- of formamidiumhalogeniden die het "canvas", een $PbCO_3$ nanodeeltjesfilm, kunnen omzetten in lichtgevende, halfgeleidende perovskieten. We brengen de inkt aan op het canvas via zelfgemaakte stempels, traditionele schilderskwast en *airbrushing* om zo lokaal lichtgevende perovskieten te creëren (Figuur S4). De kleur van de emissie van de perovskiet kan worden afgestemd van blauw naar groen en verder naar rood door de ratio tussen chloride, bromide

en jodide in de inkt aan te passen. Daarnaast laten we zien dat de IEL-methode kan worden geïntegreerd in de fabricage van (opto)elektronische apparaten zoals lichtgevende diodes (LEDs). Terwijl conventionele *cleanroom* technieken vaak duur en arbeidsintensief zijn, maken de eenvoud, schaalbaarheid, en veelzijdigheid van IEL het een veelbelovende productie route voor geïntegreerde apparaten. Gezien het grote aantal ionen uitwisselingsreacties dat al in vloeistoffen is ontwikkeld, verwachten we dat apparaten in de toekomst uiteindelijk volledig met ionenuitwisselings lithografie geprint kunnen worden.

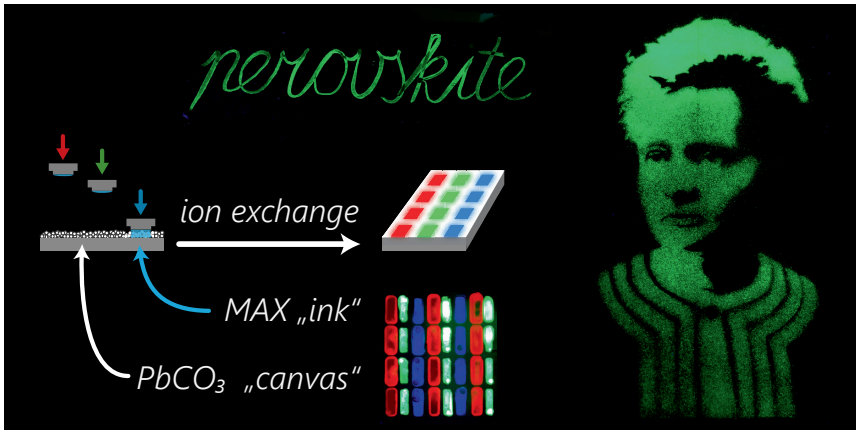

FIGUUR S4: Ion Exchange Lithography. Bovenkant: fluorescentie foto van een patroon getekend door het aanbrengen van de conversie inkt met een schilderskwast. Linkerzijde: schematische afbeelding van de fabricatie van een patroon van perovskite-film. Middenonder: fluorescentiefoto van meerkleurige contact gedrukte pixels. Rechterkant: airbrush-schilderij van Marie Skłodowska-Curie.

In dit proefschrift worden ionenuitwisseling, zelfassemblage en lichtemissie voor functionele optische materialen onderzocht. De door de natuur geïnspireerde zelfassemblage heeft de potentie om composietmaterialen zodanig te assembleren dat de functionaliteit uit de hiërarchische rangschikking ontstaat. Zo vonden we de opmerkelijke overgang van een waterige oplossing van metaalzout zonder chirale orde naar microscopische helices die een draaiing aan het licht geven. Het is inherent dat de synthese van een materiaal de uiteindelijke samenstelling ervan bepaalt. In ons geval vormen metaalzouten, carbonaat en silicaat een hiërarchische metaalcarbonaat/silica-architectuur. Deze architecturen maken lichtmanipulatie mogelijk, maar andere functionaliteiten zoals het uitzenden van licht vereisen een andere materiaalsamenstelling die niet toegankelijk is via eenzelfde syntheseroute. Conventioneel worden materialen gezien als permanent gedefinieerd door hun constituerende elementen. In dit promotieonderzoek vinden we dat ionen uitwisselingsreacties de mogelijkheid geven om de materiaalsamenstelling na de

synthese te veranderen. We maken gebruik van het potentieel van het assemblageproces om metaalcarbonaat microarchitecturen te vormen en door middel van ionen uitwisselingsreacties de materiaalsamenstelling te veranderen om een licht uitstralende perovskiet te creëren. De mogelijkheid om de materiaalsamenstelling te veranderen wordt nog een stap verder gebracht door ionen uitwisselingsreacties selectief uit te voeren op het materiaal. In plaats van meerdere materialen naast elkaar te plaatsen kunnen we op deze manier de omzetting van één materiaal in verschillende materialen lokaal programmeren.

In opto-elektronica zou zelfassemblage in combinatie met ionenuitwisseling driedimensionale elementen op een kostenefficiënte manier kunnen introduceren in conventioneel tweedimensionale routes zoals optische en e-beam lithografie. Gezamenlijk kunnen deze technieken leiden tot geïntegreerde apparaten die volledig zijn ontwikkeld op basis van zelfassemblage en ionenuitwisseling. In essentie is opto-elektronica een voorbeeld; hetzelfde concept bevat potentie voor vele gebieden zoals bijvoorbeeld katalyse en batterijen. Uiteindelijk zal de toenemende controle over kunstmatige zelfassemblageprocessen in combinatie met de veelzijdigheid van ionen uitwisselingsroutes ons in staat stellen om architecturen en materialen te fabriceren die met onze huidige fabricagetechnieken ontoegankelijk zijn.

List of Publications

Published:

Helmbrecht, L., Tan, M., Röhrich, R., Bistervels, M.H., Kessels, B.O., Koenderink, A.F., Kahr, B. and Noorduin, W.L., *Directed Emission from Self-Assembled Microhelices.* Advanced Functional Materials, 2020, 30, 1908218.
(Chapter 2)

Holtus, T., **Helmbrecht, L.**, Hendrikse, H.C., Baglai, I., Meuret, S., Adhyaksa, G.W., Garnett, E.C. and Noorduin, W.L. *Shape-preserving transformation of carbonate minerals into lead halide perovskite semiconductors based on ion exchange/insertion reactions.* Nature chemistry, 2018, 10(7), pp.740-745.
(Chapter 3)
Tim Holtus, Lukas Helmbrecht, and Hans C. Hendrikse contributed equally.

Submitted:

Helmbrecht, L., Futscher, M.H., Muscarella, L.A., Ehrler, B. and Noorduin, W.L., *Ion Exchange Lithography: Localized Ion Exchange Reactions for Spatial Patterning of Perovskite Semiconductors and Insulators*, 2020.
(Chapter 4)

Acknowledgment

This endeavor began with the sight of beautiful colored SEM images of crystal flowers on the website of AMOLF. I was caught by the aesthetics and intrigued by the science behind it. At first sight, it did not seem to match my studies. Now, many adventures into this journey later, I know that this was a perfect fit. This thesis, the essence of those years in the lab, bears only my name on the cover. Yet we know that this book is the product of the many different relations between people. In this thesis, you saw the names of those I worked with at the beginning of each chapter. Beyond these scientific bonds, there were many helping hands and guiding minds involved. This is for my mentors who guided me, the scientists from whom I learned, the colleagues that created a warm atmosphere, the old friends who are still around, the new ones that made Amsterdam a home, and the family that always supported me.

First of all, my gratitude goes to Wim for giving me the opportunity to do my PhD with him. Wim, I still remember vividly how enthusiastic we both were during the interview. From that moment, I knew I wanted to do a PhD with you. You had to learn how to start a group, while I had to learn how to become an independent scientist. It has been an incredible journey in which you taught me how to spot exciting topics, make new discoveries, and finally, how to write about them in a way that creates impact. I am happy to have had the opportunity to visit many conferences and meet renowned researchers in our field. There are many highlights of our time together—the afternoon coffees, the trip to the GRC and your former lab, the discussions in our meetings, the moments in various labs together—just to name a few. Sharing the belief that science should feel exciting, we created beautiful figures and surprising experiments to convey this feeling. This is what made the years in the lab a lot of fun and turned this thesis almost into a picture book. Even when your group grew, you always found time to meet every single one of us, supporting us with your cheerful enthusiasm. You know how to choose the right balance between guiding and granting freedom. I cannot imagine having a better mentor for my PhD.

With Wim just having started his group, we had to figure out a lot of things on our own. Well, not entirely on our own. Martin was always there to help. Thank you, Martin, for your support throughout these years, your pragmatic advice helped to readjust the efforts and gave me confidence that with careful planning, everything will work out. Once, you suggested creating a "Lukas_Thesis.tex" and adding the first paper—as you promised—this made things feel concrete, and here we have the final print of it.

Another implication of being the first PhD student is that writing a thesis is faster than getting a professor's title. Luckily, Huib became my official promotor. Thank you, Huib, for finding the time for me, even if that meant looking at my thesis during your vacations. I am impressed that although you manage a group and run the institute, you never lose your cheerful attitude.

I want to thank those that have opened this thesis not only for the pretty pictures and the acknowledgment. The Doctorate Committee took the time and effort to read this thesis down to the most minute detail. I want to thank prof. dr. E.C. Garnett, prof. dr. A.M. Brouwer, prof. dr. N.F. Shahidzadeh, dr. E.M. Hutter, prof. dr. M.L. van Hecke, and prof. dr. P. Levkin for accepting the invitation to be part of the committee and providing me with valuable feedback to eliminate the little typos before printing the thesis. I am looking forward to our scientific discussions.

Of course, I was not going to be Wim's only student. Foremost I want to thank you, Hans. Like scientific twins, we joined almost at the same time, became friends and are finishing practically together. Starting from what Tim and Daniel had set up in the first weeks of their internships, we began to build a lab together, we figured out how to be PhD students, traveled to conferences and conducted social experiments on how to create bonds between scientists. Through these years we were almost in sync with the challenges we faced, and chatting about them made everything easier. Not many PhD students get to work together with someone on the same topic towards the same goal, together with you making perovskites was a lot of fun!

Observing Wim as a mentor, I was keen on guiding students myself and got the chance to work with three excellent students. Thank you, Alicia (with your magical approach to experiments), Bruno (with your resolute effort in getting the perfect helix), and Ariane. Ariane, I am impressed by the sophistication you demonstrated already in your bachelor's research, and I am looking forward to seeing your beautiful crystal stars in a paper. Thanks for the liveliness while you were here and the friendship that followed.

From the outside—I have been told—our group sometimes looked like quite a wild mix of characters. But actually, this is what created a very enjoyable balance of personalities where each has its own place in the group. With you, Tim and Daniel, the early months when we had the freedom to decide which signature this lab will have in the future, were a lot of fun. Iarik, your pragmatic sarcasm made our lunch breaks fun and saved our meetings when we drifted off into pointless discussions. Arno, you are an infinite source of technical information—whatever the question was, you would help with something you read in a paper or you would have written some code to answer it. Marloes, your dedication to making the impossible work is fascinating, and with your caring attitude, you always created a warm atmosphere in the group. Christiaan, your weightless positivity always cheers me up, and your enthusiasm while explaining your experiments

when we met in the lab almost made me want to change topics. Sjoerd, your input to the challenges I face in the lab made me realize how important it is to routinely question everything you do in the lab. And of course, I want to thank Nesrine, Imane, Stivell, Pietro, and Miriam, who brought fresh perspectives into the group. During the many conferences and symposia, Liesbeth seemed almost part of the group. I want to thank you for the many words of advice you had on being a confident scientist. Esmee, it is exciting to see that as a secret member of the group, you bring out our science's artistic side. I find it remarkable that in our group, we always support each other and everyone will pause their own project for a moment if someone needs help. Without you all, this PhD would have been much harder and certainly less fun. I will always remember our coffees, ice-cream breaks, lunches, outings (in rain and wind), and conferences together. Our group wouldn't be complete with the indispensable help of Teresa, Karelia, and Sabine, who kept Wim's agenda together, as well as Marko, Marc, and Hinco, who kept the lab running and translated our thoughts into actual functional equipment. Marko, thank you for bringing in all the expertise on optics that I didn't have, and beyond that for the many lunch breaks together. Marc, you help with the many chemistry questions along the way was indispensable. Hinco, ik ben blij dat je altijd Nederlands tegen mij hebt gepraat en daarbij ook tegen iedereen hebt gezegd dat ze met mij Nederlands moesten praten. Dit heeft erg geholpen mijn Nederlands te verbeteren. Met veel plezier heb ik met je over het oplossen van de vele kleine technische uitdagingen van mijn PhD nagedacht. In een ander leven had de jouwe mijn droombaan kunnen zijn.

My path to becoming a scientist started long ago with many influential teachers along the way, who encouraged me in my curiosity for the world and the functioning of things. I want to thank my high school teachers, Herr Paas and Herr Landers, that got me interested in chemistry by teaching how to create color and explosions. Now, after a few years of PhD research, I am amazed by how many of the things I learned in my studies came in handy. I want to compliment dr. Mertin, prof. Bacher, and prof. Winterer for devising a university course that prepared me well enough to pursue a PhD in chemistry although studying nano-optoelectronics. Especially, I want to thank prof. Winterer and Notti for supervising both my bachelor and master theses. Listing everyone with whom I studied and from whom I learned during that time would fill a book by itself, but those who remember studying together hiding in the far corners of the library, in the Faschaftsraum with takeaway fries, or at home till deep in the night, you know who you are, and I want to thank you.

Like an apprenticeship as a craftsman is not complete without the Wanderjahre, an academic shall aim to learn from different mentors in different labs and cultures. I want to thank prof. Donghan Lee at Chungnam National University and his PhD student Jongmin, prof. Craig B Arnold at Princeton University and his PhD student Frederik, as well as prof. John Canning at the University of Sydney for

welcoming me to their labs and showing me their way to approach science. I learned how the friendship between people, the ambition, and the right questions are what develops a great scientist and enables one to make discoveries.

Having seen companies and universities, I was used to every group being a little kingdom of its own. AMOLF, however, felt more like a community with less hierarchy. It is this collaborative atmosphere that I am especially grateful for. So far, Wim's microarchitectures had been beautiful, the new mission was to make them functional. Wim and I set out to explore how they would interact with light. In our lab, we can create the self-assembled microarchitectures, but to explore their functionality, I needed help. It was clear that I needed Femius. Thank you, Femius, not only for the many funny conversations but specifically for bringing me back to the darkness of laser labs. Ruslan, thank you for introducing me to the puzzling world of Fourier optics and explaining what the light does whenever I got too puzzled. Bart, I want to thank you for introducing me to the world of crystals that twist light. It was a lot of fun to be in your lab at NYU together with Melissa, discovering how light can twist while it travels through our self-assembled helices. Melissa, your professionalism in the experiments impressed me. You were so good at finding helices and measuring them within minutes, I didn't even need to come back to New York (which was almost a little disappointing). Many thanks to the four of you; without you, there would be no chapter two.

The 3D perovskite architectures of chapter three were only possible because Erik had introduced Hans and me to his lab and the art of making perovskites. I want to thank you, Erik for the many discussions about this surprising material. Of course, we didn't do this alone and I owe a big thanks to Sarah, Gede, and Sophie. This work led to chapter four, in which I wanted to build an LED. I am thankful that Bruno welcomed me in his lab and that Moritz and Loreta did everything possible to help with knowledge and hands-on lab work to eventually make this happen. I also want to thank Louis for our many discussions with Wim and Alicia on manipulating the growth of the helices. I am looking forward to the day where you grow a field enantiomerically pure helices. The best thing that can happen to research is when it sparks someone's curiosity, and they decide to continue it. Therefore, I am honored that you, Igor, chose to introduce ion exchange reactions to your group and thank you Lucas for starting your postdoc by coming here to learn how to convert chalk into perovskite.

I also want to thank everyone who makes AMOLF a place where I only need to worry about getting my experiments working. My thanks go to Ad, Marjo, and Juliette whose warm welcome in the morning brightens my day already at its start, to Tineke and her team who keep things neat and tidy (especially to Kaya, who saves the plants and Jusuf), and to Floortje's team of the canteen. A PhD is full of technical challenges and this is a big thanks to those that helped to solve them all: Thank you, Hans, Bob, Andries, Dimitry, and Igor from the nanocenter. Without you, none of the beautiful SEM images would be here. Hinco, thank you for

always inventing something on the spot for the many technical challenges I faced. Dion, thanks for getting enthusiastic about my experiments, especially when you made the stamps. Niels, the many Christmas Lunch projects with you were a lot of fun. Ilya, Marnix, and Henk-Jan form the design department; your ability to transform a vague pencil sketch into a technical drawing is impressive. Thank you, Jan, Tom, Wessel, and the other fantastic craftsmen/craftswomen of the workshop, for bringing my ideas to reality and for the many interesting conversations we had. Jan, I enjoyed our many chats about the scientific and hobby projects you are mastering and am thankful for the advice you had for mine. Tom, the cheerfulness with which you tell about the things you are currently building makes me want to do an internship in the workshop. Wessel, it is always nice to pass by the workshop and hear about the things you are making and chat about photography equipment. Erny and Petra, thank you for promoting me to the official unofficial AMOLF photographer. I am honored that you gave me the possibility to grow into this role. I always enjoy passing by to hear about the events you are planning and to brainstorm about the next photo session for AMOLF news. Oana, thank you for your indispensable help in dealing with publishers, open access, and copyrights. Valeska, Reshma, Sharlene, Linda, and Wouter, thank you for having arranged such a smooth start into my Amsterdam life by sorting out my housing and since then taking care that PhD students don't need to do much paperwork. Thank you, Tatiana and Angela, for helping countless times with the many orders I wanted to place at obscure suppliers and even more for being the Christmas angels. Also, thanks to Tarik, Andre, and Clyde, I am happy that you always keep the building running so smoothly. Clyde, you are certainly one of the most iconic figures of AMOLF. Your authenticity brightens my day every time we meet. We met at all the fun PhD defense parties, and I am looking forward to seeing you at mine. Thank you, Floortje, Karelia, Teresa, Henriëtte, and Sabine; if it weren't for your effort to structure the group leaders' agendas and tell us where we can find them, no one would graduate on time.

AMOLF is not complete without the PV. Floortje, Niels, Hans, Konrad, Annemarie, Niels, Giorgio, Giulia, Sukanth, Christian, Lennard, Tom, Loreta, Jeffrey, and Isabelle. I want to thank you all for being such a great team and all the fun we had together with organizing the best borrels and most fantastical Christmas Lunches AMOLF has seen. We couldn't have organized events this big without all the helping hands that have helped setting up and tidying up. Thanks to you and thanks to those that showed up to the events. Of course, I also want to thank those that established the PV before us and those that continued once I left. Beyond the PV, I want to thank everyone who was part of the many other activities. Nasim, thank you for initiating a language café that reflects the international spirit of AMOLF. Thanks to those who met in the Climate Lunches to discuss what we scientists can do about the climate (thank you, Giada for kicking off the first

meeting) and those who would just start a spontaneous vrijdagmiddagborrel with a message in our life of pi whatsapp group.

The office I was in felt sometimes more like a botanical garden than an office. This little green oasis has hosted many friendly faces throughout these years. Katharina and Erçağ, the plant we chose together, has been my steady companion, who reminds me of the beginning at AMOLF and our time in the office. Erçağ, I like to recall the many productive hours in silence, interwoven with deep conversations, and occasionally compensated with a concert at Paradiso. Ariane, with your arrival in the office, the calm was replaced by positive energy with which you motivated everyone to leave their comfort zone. When Ariane left, it took till you, Hanne, arrived and with you, liveliness returned. Anne, you, together with Hanne, have brought the mood in our office to another cheerful peak. When I had to move into the corona-home-office, I realized how vital this atmosphere was for me. I missed the steady calm of you, Zhou, recalled the chats about life with Rob, and the days with Daniel, Nesrine, Alicia, and Imane, who once were part of the office. Said, Falco, Marnix, and Bob, you joined us so often, you feel like temporary office mates that I now miss. I am thankful to have had such lovely company throughout the years with whom we could work in silence and chat about life.

You will have noticed that the SEM images on the cover are the most colorful ones you have ever seen. These images were taken by Stefan Diller, purely motivated by the beauty of the microarchitectures. I want to thank you, Stefan for reaching out to us, taking such fantastic images, and even making 3D movies. This was the most surprising and most aesthetic collaboration of my PhD. And to the scientists with beautiful SEM specimen: make sure to tell Stefan about it. I am grateful to those that helped to make the inside of this thesis artistic. Henk-Jan, I like recalling the photoshoot for the sand dollars, spending a day in a dark room throwing sand dollars into an aquarium. Det, I want to thank you for teaching me how to make a coral from clay during the "Molding Nano" workshop with Giada. Rogier, thank you for passing by AMOLF to take these impressive photos of scientists, including me.

To my paranymphs Annemarie and Leonie—I chose you because you are smart enough to defend this thesis with words and fearless enough to defend it with a sword if that was still allowed. I am honored that you accepted my invitation, also because you both match my spirit of the PhD—always dedicated to perfection in the lab, and rarely frustrated about the frustrations of science and devoted to actively enjoying every moment outside of the lab. Annemarie, thank you for all the traveling we have done together. Independent of where we are, you always have the right advice and your sober realism has brought my mind back to solid ground many times. Leonie, thank you for the many conversations we had on the many aspects of life. From theater plays and unknown indie bands to shady

take out restaurants and beer at Joost, you are the loveliest companion to venture through the nights of Amsterdam while never losing our calm.

Most of the friendships I made at AMOLF started with an encounter at the coffee machine. If we had given the coffee machine a name, I would thank her for being such a good companion throughout the years. She started on the same day as me and made about 20.000 coffees a year. In front of the coffee machine, everyone is equal—master students can show senior professors how to make a good espresso, and group leaders can casually check in on their students. I recall many chats and want to thank Albert for his caring career advice, Bas for showing me how to froth milk properly, Pieter Rein for enthusiastic stories about his research, Femius for commenting on conversations with humorous facial expressions, Paula for stories on her travels, Kristina for discussions on gender equality, and Bruno and Erik for spontaneous advice on misbehaving perovskites.

Walking from the coffee machine to our lab always involves a brief but pleasant journey through the lab of Martin. On my way through, I often got stuck—distracted by this physics playground. Scott playing with bouncy balls, Anne crumpling plastic sheets, Corentin programming smiley faces in rubber, and Hadrien putting architectures in the hydraulic press, you always brightened my day with brainstorming about what else one could do with all those squishy or wrinkly rubber things. Thank you for showing me how fun mechanics can be!

I made many friends at AMOLF during my PhD. Some of you I saw only inside of AMOLF, others mostly outside. Without being able to mention all the names, I want to thank everyone who socializes at the coffee machine. Somehow there is always someone having a coffee to have a chat with, no matter if day or night. Moritz, when we met during my interview, little did I know back then what lasting friendship would develop. I like to look back at the places we explored together, from morning coffee with a panoramic view in Berlin to Zürich with Laura and Leo. Giada, thank you for bringing art and politics into AMOLF. With you, I enjoyed exploring the hidden sides of Amsterdam and learning how to make the best pizza in Italy with your parents. Now that our friendship has brought us safely through the last few months of intense thesis writing, I am looking forward to meeting again somewhere and starting another artistic project. Giorgio, thank you for the many coffee breaks we spent trying to get a decent coffee out of mediocre beans and the many evenings in which we thought we would write code but ended up cooking dinner. Your culinary dedication is amazing, and I am looking forward to many more dinners with Andrea and you. Nasim, I am always amazed by the endless source of cheerful energy inside of you. I couldn't imagine anyone else starting a language café and getting so many people excited about it. When the green oasis of my office faced the lockdown, you adopted the plants and gave them as much care and attention as you give your friends. Thank you for balancing my soul with delicious Persian dinners when there seemed to be only work, and the writing bound all my time. Dario, the dinner evenings

with you were great. I especially like to remember all the food adventures we had together—walking half an hour through town just to try another bar that someone told us would have the best jamón ibérico. Agustin, conversations with you always bring back my optimism. When you listen, you are always interested, yet nothing can surprise you. Jenny, where ever you are, things are cheerful. I always enjoyed how, wherever you go, your laugh signals your arrival. Carolyn, whenever you cook and bake, I feel reminded of home, and whenever I was gone, and you took care of my plants, they seemed happy as if they had been on vacation themselves. Giulia, many of my friends admire food, but your passion for original ingredients impresses me. Thank you for showing me these flavors and hosting dinners with Nicola. Cristina, thank you for the concerts together and the Zen you radiate. Felicio, thank you for sharing many beautiful techno experiences, no matter how far we had to travel.

In such a rainy country, sunny days need to be worshipped. On a sunny day, no one would risk wasting time late at AMOLF or even at home. The many summer barbecues were a great place to make and develop our friendships. Marco, Ale, Masha, Nicola, Mario & Olga, Lorenzo, Giorgio & Andrea, Agustin & Bram, Cristina, Jenny, Agata, Parisa, Carolyn, Laura, Dario, Eliane, Moritz & Laura, Giulia & Judith, Ruslan, Kevin, you were indispensable for a party mood, no matter whether in the park or at a party, you would make sure some dancing would happen. Federica, thank you for bringing the physics and the biophysics parts of AMOLF closer together when you first suggested merging two different BBQs.

I want to thank everybody that made my life at AMOLF richer—Kevin (for your sarcasm that lifted the mood of any coffee or lunch break), Christiaan M (for your support and the nice postcards), Loreta (for making me feel at home in Rome and never getting tired of my perovskite questions), Chris (for the grounding atmosphere that surrounds you), Marloes (for our shared fascination for the mind), Henk-Jan (for your advice on photography and the sand dollar photo shoot), Rob (for radiating kindness wherever you go), Sander and Sebastian (yours were the first defenses I addended and was looking forward to having that same confident seniority by the time I would finish my PhD), Roberto (for our many lunch time conversations about food and for briefing me for my Mexico travels), Mario (for the energy you brought into every party), Isabelle (for your dance moves and trying to teach them as well as sharing the fascination for photography), Ilya (for the concerts and parties we went to together and for adding liveliness to Eindhoven), Ruslan (for your endless enthusiasm, and for hosting fun house parties), Lucie (for your caring personality and the posters on influential female scientists in your office window), Susan (for bringing a sense of fashion into AMOLF), Steffen (for welcoming me at AMOLF in odd hours), Eline (for your support in perovskite questions and encouraging women to stay in science), Benjamin and Christian D. (for bringing up politics from a German and a Dutch perspective and sharing

the obsession with coffee), Beniamino and Charly (for your inspiring lively spirit that made me question the productivity obsession at AMOLF), Mareike (for the kind atmosphere you bring wherever you go), Bob (for inspiring me to bring more lab equipment to the kitchen) and Bob together with Dimitry (for encouraging everyone at the borrels to go wild), Tom (for the conversations on coffee and rebuilding a house), Alexander (for more conversations on coffee), Hugo (for the many conversations over lunch and the enthusiasm with which you explain your research here and in Zürich), Anne (for your positivity each day and our snack-sharing friendship), Verena (for your determination to make this world a better place), Eitan (for challenging me and everyone with questions and sarcasm), Said (for the lunches together, the interest in the people around you and the different perspective you bring to conversations), Luuk (for sharing your experiences about your life as an artist and advice how to bring that out in myself). Also, the many other little encounters in the daily AMOLF life really make a difference. I was always happy to run into you—Cesare, Laura, Marco, Yuval, Melle, Bart, Rene, Hongyu, Matthijs, Jian-Yao, Magda, Fotios, Aaron, Alexandra, Luca, Harmen, Matthias, Sven, and Nick. Some of you I especially remember for the shared passion for food—Nicola (for having the best food a defense has seen), Andrea (for constantly talking about coffee or food), Agatha (for importing polish sweets and sausages), Parisa (for bringing Safran from Iran to assure that I cook with quality ingredients), Anders (for making Haggis and the most elaborate cakes), Eliane (for shining at every cake baking contest), Harshal (for teaching me some Indian cooking skills), Jumin (for making a proper Korean bbq), and finally the bread-baking friends: Kelly, Moritz, Cristina, Giorgio and Verena.

The first days in Amsterdam, before even starting my PhD, I dedicated to learning Dutch. Not only would this be the basis for integrating into Amsterdam, I also made good friends. Nina and Johanna, I am happy we are still in touch this long after the course. Zita and Vainius, you were my first friends in Amsterdam and you are such a cosmopolitan couple with amazing friends. I am looking forward to seeing you again, somewhere on this globe. Alex J., for you, it took a while till you eventually moved here, but since then, we had many coffees and beers talking about the Dutch things we like and the German things we miss.

Amsterdam is a place of art and liveliness. Marlies, you showed me how colorful and fun that world is, and with you, I discovered many of those colorful aspects in myself. The energy with which you move around the globe to follow your passion for fashion inspires me to live as intensely as you and never get stuck in a place. Rosa, I always enjoyed creating and discovering with you. Steffi and Davide, whenever I met you two somewhere, I knew I had picked the right event for the evening. Ashley, thank you for showing me how different and yet similar a PhD student's life can be that has to do fieldwork instead of lab work. Ruth, we both still are surprised how randomly our friendship started and how it grew into a close bond over the course of a summer. You inspire me with the

ease with which you go through life and the many references to literature you use to comment on what happens around you. I enjoy recalling the trips we went on and am grateful for the support we give each other—you are the best. Ranes, it is beautiful how we met through music and how, ever since, we've been cooking well and made people dance. Paloma, you see the world with critical eyes; the Columbian anthropologist in you has made me aware of the often Eurocentric routine with which I look at the world. Imran, you are one of the most loving and kind persons I know. Thank you for our conversations without judgment. You truly know how to make everyone feel appreciated. Kat, our shared fascination for sound, light, and the mind has started a wonderful friendship. Egle, it is always fun to explore museums with you. Alex K., the BBQ's with you in Duisburg were always a culinary highlight. I am glad that now, you and Hanneke are just a few minutes away. There are many more that have made my time in Amsterdam unforgettable, Istvan, Joy, Jonathan, Doet, Miko, Willem, Szymon, Mohammad, and all the others that I may have forgotten to mention; thanks for your friendship!

Part of my time in Amsterdam was not actually in Amsterdam. Tobi, you challenged me to move into a home office before it was cool. And then take this home office with me around the world to meet you in Peru and Mexico. Thank you for showing me a different way of living and helping me to learn so much about myself.

This thesis would not have been possible without my amazing friends that supported me through school and university. I am grateful that our friendships continued, and so many of you came to visit me here in Amsterdam. I want to thank all of you for the many contributions to my life. Kati, I enjoy looking at the many years we spent together and how we grew with one another. Christian and Hendrik, by now, you are kind of family, making me feel at home whenever we meet. Together with Kati, Anna, Lina, Marcel, Eva, Katha, and Anka, you two always make me feel welcome in Witten. Jacke, I enjoy your reflective view on the world. Dominique, I keep being impressed by our friendship that lasted although we changed so much during these years. Chrisi, it has always been great fun to come back to Witten to your parties. Even more importantly, you also visited so regularly that I never felt like I really lived abroad, especially when Lena and Lauritz joined. Lünd, your critical perspective on current affairs is always a great start for conversations. Cornelius, I like creating art with you. I wish there was a way to add NanoTropics as a video at the end of this text. Marcel, thank you for never losing contact through these many years. Maria, I enjoy your directness and liveliness; thanks for still being there after these many years. Johannes, I am impressed that no bus ride can be long enough to discourage you from passing by. Jean, thank you for bearing even longer bus rides and sharing your fantastic taste in music. Eddie, I am inspired by the many lives you have lived and still remember when you wrote your first book full of illustrations. I am sure you will approve of this scientific equivalent. Henning, your drive and entrepreneurial

spirit keep me inspired to be open to the possibilities that make life exciting. Julien, thank you for balancing out the hectic ones with your peaceful atmosphere. Alex, I am amazed at the energy you go through life with. Especially with you, Zoey, you two become unstoppable. Around you two, life is not allowed to become a boring routine, thanks for the times together.

Studying NanoEngineering was quite an experiment, but going through this together with friends made it a memorable time. Seeing you again in Amsterdam, on my birthdays, at fusion, and in your new homes means a lot to me. Caner, your dedication and entrepreneurship keep impressing me—Kaiserberg for life! Mohamed, you are the best flatmate in the world. Andreas, imagining wild scientific ideas with you, always revives my fascination for science. Stevan, thank you for our many conversations about photography and food. Alex, your attitude makes conversations relevant, and when they pause, your taste in music pleasantly fills the room. Stephan, I enjoy listening to the stories of your adventures. Erik, thank you for first introducing me to Arduino projects and sharing a fascination with electronics. Eric, the many cooking evenings at yours are some of my favorite memories of the last Duisburg years. Domme, thank you for reuniting us every time around your birthdays and for the many music recommendations you (and your dad) gave. Samer, your fascination for fire and photography makes the conversations always exciting. Rene, thank you for our nighttime walks with beer and discussions in whichever city we met. Lana, you are always a great addition to those walks. Ina, thank you for always having a loving word of support for me and for all your friends. Freddy, your cheerful chaos always brightens my mood. Kevin, planning our fusion mascots together is the best part of fusion preparations. Tim, thank you for making sure that at some point in the night, everyone dances to psytrance. Lisa, thank you for the many weekends spent with music and good food. Patti, the friendship with you is the most valuable element our studies created. With you, I feel comfortable telling anything that is on my mind, and many times your challenging questions have brought clarity to my thoughts. From calm to wild, from fine teas on the couch to Kellertechno in concrete bunkers, time with you is extraordinary. Danke, dass du meine beste Freundin bist.

I am really fortunate to have a very supportive family, this includes everyone from siblings, parents, grandparents to aunts and uncles, cousins, and those that feel like family. Especially the infinite loving support of my parents made it possible to make it this far. Thank you, Mia and Detlef, for supporting me in every possible way—teaching me to be independent and think in a critical analytical, and creative way. By its very nature, there is more I am grateful for than these few lines can express, yet here are some thoughts that came to my mind. Detlef, you taught me how to overcome any problem that involves technology, code, or mathematics and inspired me with your fascination for sound and music. Mia, you are the origin of my passion for food and art. From you, I learned to dream and create. Oma, wenn ich sehe wie munter und aktiv du noch mit über neunzig

bist, habe ich keine Angst alt zu werden. Mit deinem Hühnersuppen Rezept rettest du mich jedes Mal durch die verregneten Amsterdamer Winter. Opa, von dir habe ich gelernt gründlich zu arbeiten und Nickerchen zu machen. Granny and Jeddo, you inspired me to aim high, and I am proud to carry on your passion for food and festivities. Nelly, thank you for your moral support during the years of my PhD. We understand each other and the challenges the life as a scientist brings. Kilian, thank you for the many conversations in which we sorted our thoughts on the situations we are in. Through your analyses that that span from the details to the big picture you have opened my perspectives on the world. With both of you, I share the curiosity for the world and am amazed to see your ways of uncovering the unknown. Time with you two always grounds me, and your reflective view on the world sparks my enthusiasm for life. Mit euch allen teile ich nicht nur die Neugierde für die Welt, sondern auch die Leidenschaft für gutes Essen, eine Gemeinsamkeit die zusammen mit euch am meisten Freude bereitet.

Together, all of you played a role in making this thesis possible. And even beyond that, you shaped who I am now. Thank you!


Nikon
Photo: Rogie Chang - chang.nl

About the Author

Lukas Helmbrecht was born in 1988 in Germany. Inspired by inventors such as *Gyro Gearloose* and *Gaston Lagaffe*, his enthusiasm for understanding and observing his surroundings manifested at a young age. He enjoyed taking apart tape recorders, soldering electronics but also creating flavourful dishes, making movies, and documenting the world with his parents' analog camera.

When considering how to translate his observant and creative nature into a career, Lukas decided to explore the natural sciences and promised himself that art would always follow him on this journey. Being curious about many different disciplines, he chose NanoEngineering, which fuses electrical and mechanical engineering, process technology, mathematics, physics, and chemistry. In 2011, he obtained his Bachelor's degree from the University of Duisburg Essen (UDE). He thoroughly enjoyed this interdisciplinary blend and graduated with a Master's degree in NanoEngineering from the UDE in 2015. During his studies, he was an elected member of the student's parliament, co-founded a tutoring company, and created award-winning movies.

During Lukas' time as a student, his spirit of discovery brought him to many different labs around the world. He spent a semester in South Korea at Chungnam National University in the lab of prof. Donghan Lee and had the pleasure of working in the lab of prof. Craig Arnold at Princeton University. He concluded his studies with a thesis on laser-sintering of nanoparticles for printed electronics, supervised by prof. Markus Winterer at the UDE.

After his masters, Lukas traveled through Australia and came across the work of prof. John Canning at the University of Sydney. He was delighted to join John's lab for a short research stay, in which he created optical fibers through self-assembly of nanoparticles. The joy Lukas felt while discovering the unknown confirmed he should pursue a PhD in a field that connects optics with nanotechnology.

In 2015, Lukas met dr. Wim Noorduin, who shared the belief that science can be a fascinating adventure. Therefore, he moved to Amsterdam to begin his PhD at AMOLF, and on the left, we see him during his early days in the lab. Little did he know at this time, that he would become the official unofficial AMOLF photographer and an enthusiastic member of the events committee. As Wim's first student, Lukas was excited to help transform an empty room into a lively research lab. Together, Wim and Lukas launched a new line of research on beautiful crystal flowers—to say it in more technical terms: self-assembled carbonate microarchitectures. Lukas discovered ways to manipulate light with those microarchitectures and developed a new route to create perovskite semiconductors. The scientific endeavors of those years at AMOLF are presented in this thesis.